

AD-A097 471

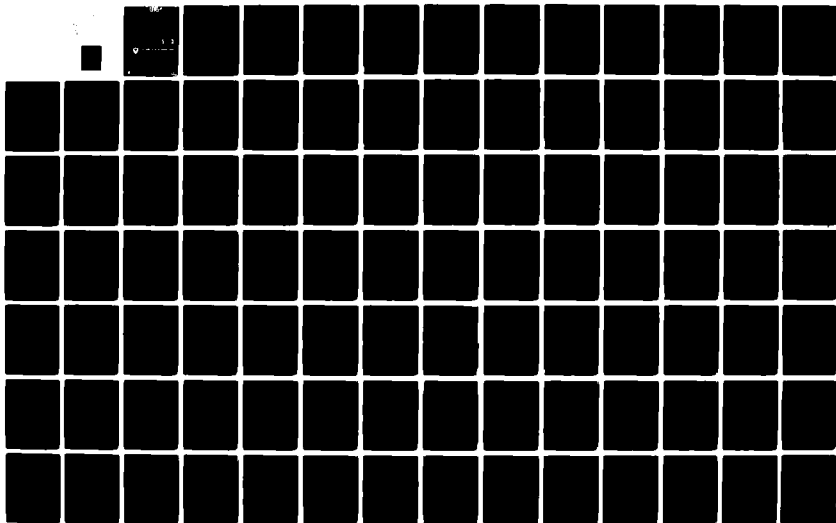
ARMY ARMAMENT RESEARCH AND DEVELOPMENT COMMAND ABERD--ETC F/G 20/1
ANALYTIC MODEL AND NUMERICAL SIMULATION OF SHOCK WAVE PROPAGATI--ETC
JAN 81 J A SCHMITT, R E LOTTERO, H J GOODMAN

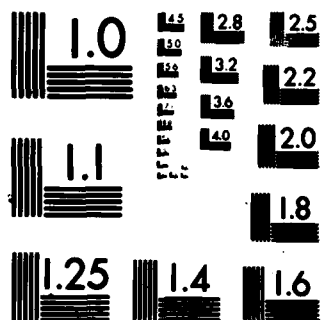
UNCLASSIFIED

ARBRL-TR-02286

SBIE-AD-E430 582

NL





MICROCOPY RESOLUTION TEST CHART
NATIONAL BUREAU OF STANDARDS-1963-A

(12) LEVEL III
F

AD

AD A 097471

TECHNICAL REPORT ARBRL-TR-02286

ANALYTIC MODEL AND NUMERICAL SIMULATION OF
SHOCK WAVE PROPAGATION INTO
A REENTRANT CORNER

J. A. Schmitt
R. E. Lottero
H. J. Goodman

DTIC
ELECTE
S APR 8 1981 D
B

January 1981



US ARMY ARMAMENT RESEARCH AND DEVELOPMENT COMMAND
BALLISTIC RESEARCH LABORATORY
ABERDEEN PROVING GROUND, MARYLAND

Approved for public release; distribution unlimited.

FILE COPY

81 3 27 009

Destroy this report when it is no longer needed.
Do not return it to the originator.

Secondary distribution of this report by originating
or sponsoring activity is prohibited.

Additional copies of this report may be obtained
from the National Technical Information Service,
U.S. Department of Commerce, Springfield, Virginia
22161.

The findings in this report are not to be construed as
an official Department of the Army position, unless
so designated by other authorized documents.

The use of trade names or manufacturers' names in this report
does not constitute endorsement of any commercial product.

UNCLASSIFIED

SECURITY CLASSIFICATION OF THIS PAGE (When Data Entered)

REPORT DOCUMENTATION PAGE		READ INSTRUCTIONS BEFORE COMPLETING FORM
1. REPORT NUMBER TECHNICAL REPORT ARBRL-TR-02286	2. GOVT ACCESSION NO. AD-A097471	3. RECIPIENT'S CATALOG NUMBER
4. TITLE (and Subtitle) Analytic Model and Numerical Simulation of Shock Wave Propagation into a Reentrant Corner	5. TYPE OF REPORT & PERIOD COVERED	
7. AUTHOR(s) J.A. Schmitt R.E. Lottero H.J. Goodman	6. PERFORMING ORG. REPORT NUMBER	
9. PERFORMING ORGANIZATION NAME AND ADDRESS Ballistic Research Laboratory ATTN: DRDAR-BLB Aberdeen Proving Ground, MD 21005	8. CONTRACT OR GRANT NUMBER(s)	
11. CONTROLLING OFFICE NAME AND ADDRESS US Army Armament Research & Development Command Ballistic Research Laboratory ATTN: DRDAR-BL, APG, MD 21005	10. PROGRAM ELEMENT, PROJECT, TASK AREA & WORK UNIT NUMBERS RDT&E 1L161102AH43	
14. MONITORING AGENCY NAME & ADDRESS (if different from Controlling Office)	12. REPORT DATE January 1981	
	13. NUMBER OF PAGES 113	
	15. SECURITY CLASS. (of this report) UNCLASSIFIED	
	16a. DECLASSIFICATION/DOWNGRADING SCHEDULE	
16. DISTRIBUTION STATEMENT (of this Report) Approved for public release; distribution unlimited.		
17. DISTRIBUTION STATEMENT (of the abstract entered in Block 20, if different from Report)		
18. SUPPLEMENTARY NOTES		
19. KEY WORDS (Continue on reverse side if necessary and identify by block number) Shock Tube Experiments Shocks Analytic Model Hydrocode DORF Stair-Step Reentrant Corner Mach Reflection		
20. ABSTRACT (Continue on reverse side if necessary and identify by block number) 10001 An analytical model is developed and numerical simulations are performed for shock wave propagation into a reentrant corner. The analytical and numerical results are compared with shock tube experiments performed in a 100° reentrant corner with a moderate strength ($P_1/P_0 = 2.37$, shock overpressure 137.9 kPa) incident shock and a weak ($P_1/P_0 = 1.12$, shock overpressure 12.41 kPa) incident shock. The analytical model provides an exact solution of the flow field if		

DD FORM 1 JAN 79 1073

EDITION OF 1 NOV 65 IS OBSOLETE

UNCLASSIFIED

SECURITY CLASSIFICATION OF THIS PAGE (When Data Entered)

UNCLASSIFIED

SECURITY CLASSIFICATION OF THIS PAGE(When Data Entered)

shock diffraction does not occur within the reentrant corner; it also provides an approximation to the peak vertex pressure which is comparable with experimental results if diffraction does occur. Both regular and Mach reflections are modeled. When the corner has finite length, an estimate of the duration of the peak vertex pressure is given. The numerical simulations are performed with the Eulerian hydrodynamic computer code DORF. In the DORF calculations, the reentrant corner is formed by a rigid smooth wall and a rigid stair-step wall. A detailed discussion of the stair-step construction and comparisons of the pressure distributions along these walls are included. Furthermore, the analytical and numerical pressure results for an infinitely long reentrant corner are compared.

UNCLASSIFIED

SECURITY CLASSIFICATION OF THIS PAGE(When Data Entered)

TABLE OF CONTENTS

	Page
LIST OF TABLES.	5
LIST OF FIGURES	6
1. INTRODUCTION.	11
2. EXPERIMENTS	15
3. ANALYTIC MODEL.	17
3.1 Theory for an Infinite Corner.	17
3.2 Examples	27
3.3 Peak Pressure Duration for a Finite Corner	34
4. DORF CODE SIMULATION OF AN INFINITE CORNER	40
4.1 DORF Code Description.	40
4.2 Examples	43
4.3 Stair-Step Approximation	44
4.4 Comparison of the Pressure Along the Smooth and Stair-Step Walls	53
5. COMPARISON OF PRESSURE VALUES FROM EXPERIMENTS, ANALYSES AND NUMERICAL SIMULATIONS	76
5.1 Experimental, Analytical and Numerical Peak Pressure Values at the Vertex.	76
5.2 Experimental and Analytical Peak Pressure Duration Values.	79
5.3 Analytical and Numerical Pressure Results Within an Infinite Corner.	80
6. CONCLUSIONS	85
ACKNOWLEDGMENTS	91
REFERENCES.	92

TABLE OF CONTENTS (Continued)

	Page
APPENDIX A. DERIVATION OF THE OBLIQUE SHOCK RELATIONS.	95
APPENDIX B. EXPLICIT FORMULAS FOR OBLIQUE SHOCK CALCULATIONS	99
LIST OF SYMBOLS	101
DISTRIBUTION LIST	103

LIST OF TABLES

Table		Page
1	Summary of Experimental Shots.	18
2	Regional Flow Properties for Shot 2 in Laboratory Coordinates.	31
3	Regional Flow Properties for Shot 1 in Laboratory Coordinates.	37
4	DORF's Initial Values for Shot 2.	45
5	DORF's Initial Values for Shot 1	46
6	Peak Pressure Duration Data From Experiments and Analytic Model	79

Accession For	
NTIS GRA&I	<input checked="" type="checkbox"/>
DTIC TAB	<input type="checkbox"/>
Unannounced	<input type="checkbox"/>
Justification	
By	
Distribution/	
Availability Codes	
Dist	Avail and/or Special
A	

LIST OF FIGURES

Figure	Page
1 Schematic of Incident Shock in a Concave Corner of Infinite Width.	12
2 Schematic of the Experimental Shock Tube Model.	16
3 Regular Reflection in a Neighborhood of the Reflection Point Q	21
4 Mach Reflection in a Neighborhood of the Triple Point Z	24
5 Criterion for Determining the Presence of Regular and Mach Reflection (Adapted from Reference 14).	28
6 Flow Field Before the Incident Shock Reaches the Vertex for Shot 2.	29
7 Flow Field Shortly After the Incident Shock Reaches the Vertex for Shot 2.	32
8 Flow Field Before the Incident Shock Reaches the Vertex for Shot 1.	35
9 Flow Field Shortly After the Incident Shock Reaches the Vertex for Shot 1.	36
10 Rarefaction Wave Propagation Along a Finite Wall (a) Before and (b) After the Incident Shock Reaches the Vertex	39
11 Initial Flow Field for DORF Simulations	47
12 Reentrant Corner Construction	48
13 Stair-Step Wall Constructions Used in AWFL-HULL Code Study ⁹	51
14 Detailed Portion of Computational Domain Near the Vertex	54
15 Comparison of Wall Pressure Values for Shot 2 at $t = 0$	56
16 Comparison of Wall Pressure Values for Shot 2 at $t = 69.74\mu s$	57

LIST OF FIGURES (Continued)

Figure	Page
17 Comparison of Wall Pressure Values for Shot 2 at $t = 114.3 \mu s$	58
18 Comparison of Wall Pressure Values for Shot 2 at $183.6 \mu s$	60
19 Comparison of Wall Pressure Values for Shot 2 at $t = 321.4 \mu s$	61
20 Comparison of Wall Pressure Values for Shot 1 at $t = 0$	62
21 Comparison of Wall Pressure Values for Shot 1 at $t = 91.09 \mu s$	63
22 Comparison of Wall Pressure Values for Shot 1 at $t = 142.4 \mu s$	64
23 Comparison of Wall Pressure Values for Shot 1 at $t = 240.7 \mu s$	65
24 Comparison of Wall Pressure Values for Shot 1 at $t = 465.6 \mu s$	66
25 Comparison of Wall Pressure Histories at a One and a Half Cell Distance From the Vertex for Shot 2.	68
26 Comparison of Wall Pressure Histories at a Two and a Half Cell Distance From the Vertex for Shot 2.	69
27 Comparison of Wall Pressure Histories at a Three and a Half Cell Distance From the Vertex for Shot 2.	70
28 Comparison of Wall Pressure Histories at a Four and a Half Cell Distance From the Vertex for Shot 2.	71
29 Comparison of Wall Pressure Histories at a One and a Half Cell Distance From the Vertex for Shot 1.	72

LIST OF FIGURES (Continued)

Figure	Page
30 Comparison of Wall Pressure Histories at Two and a Half Cell Distance From the Vertex for Shot 1. . .	73
31 Comparison of Wall Pressure Histories at Three and a Half Cell Distance From the Vertex for Shot 1. . .	74
32 Comparison of Wall Pressure Histories at Four and a Half Cell Distance From the Vertex for Shot 1. . .	75
33 Comparison of Experimental, Analytical and Numerical Values of the Peak Vertex Pressure for Shot 2.	77
34 Comparison of Experimental, Analytical and Numerical Values of the Peak Vertex Pressure for Shot 1	78
35 Comparison of the Analytic and DORF Pressure Histories at Cell 1 (5 mm along the smooth boundary) for Shot 2	81
36 Comparison of the Analytic and DORF Pressure Histories at Cell 4 (35 mm along the smooth boundary) for Shot 2	82
37 Comparison of the Analytic and DORF Pressure Histories at Cell 30 (55.1 mm along the axis of symmetry) for Shot 2.	83
38 Comparison of the Analytic and DORF Pressure Histories at Cell 31 (off the axis of symmetry, 55.9 mm from vertex) for Shot 2.	84
39 Comparison of the Analytic and DORF Pressure Histories at Cell 1 (5 mm along the smooth boundary) For Shot 1	86
40 Comparison of the Analytic and DORF Pressure Histories at Cell 4 (35 mm along the smooth boundary) for Shot 1	87
41 Comparison of the Analytic and DORF Pressure Histories at Cell 30 (55.1 mm along the axis of symmetry) for Shot 1.	88

LIST OF FIGURES (Continued)

Figure	Page
42 Comparison of the Analytic and DORF Pressure Histories at Cell 31 (off the axis of symmetry 55.9 mm from vertex) for Shot 1.	89

1. INTRODUCTION

When a shock wave propagates into a concave corner, it is reflected one or more times from the walls forming the corner. Upon reaching the corner, the direction of the shock propagation is reversed, one or more additional reflections may occur, and, in general, the last reflected shock is diffracted. These multiple reflections cause significant increases in the pressure along the walls as compared with a single normal reflection. Therefore, such corners may be susceptible to damage from blast waves that might otherwise cause little or no damage elsewhere on a structure. Examples of such corners are the wing/body junctions of aircraft and helicopters.

If the propagation direction of the incident shock lies in the cross-sectional plane of a reentrant corner and if the corner's width is "large enough", then a two-dimensional model can be applied near the mid-plane of the corner. See Figure 1. The purposes of this report are: (1) to develop an analytical model for the two-dimensional shock wave propagation into a reentrant corner which can determine the peak pressure and its duration at the vertex of a corner of a general angle and for an arbitrary incident strength shock; (2) to simulate the above phenomenon numerically using the DORF hydrodynamic computer code¹; and (3) to validate the results of (1) and (2) by comparing them with shock tube experiments as well as with each other. By comparing the results from the analytic model, the numerical calculations, and the experiments, it is possible to quantify the capabilities and limitations of each. This is of particular importance relative to the numerical calculations which, in principle, can simulate more complex flows than any analytic model and can provide more complete information than any experiment. However, the reliability of a code in predicting a particular type of flow field must first be established. This report provides a partial evaluation of the DORF code as a tool for simulating shock wave propagation in a reentrant corner. The pressure profile difference along a smooth boundary versus a stair-step boundary is discussed.

Section 2 of this report describes the shock tube experiments which were performed at the ARRADCOM Ballistic Research Laboratory (BRL).

The analytic model is described in detail in Section 3. The mathematical problem corresponding to Figure 1 with the additional assumption of infinitely long walls has been solved analytically in several special cases. Lighthill² considered an arbitrary strength shock propagating into a corner with an vertex angle 2α which deviated only slightly from

1. Johnson, W.E., "Code Correlation Study", AFWL-TR-70-144, US Air Force Weapons Laboratory, Kirtland Air Force Base, NM (April 1971).
2. Lighthill, M.J., "The Diffraction of Blast II", Proc. Roy. Soc., Series A, Vol. 198, pp 554-65, 1950.

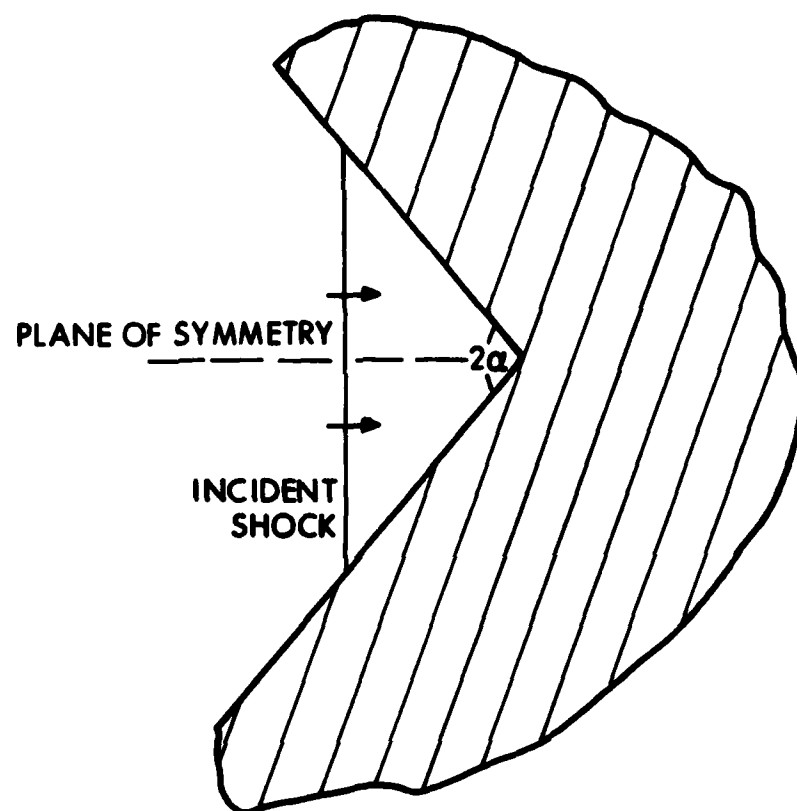


Figure 1. Schematic of Incident Shock in a Concave Corner of Infinite Width.

180°. Keller and Blank³ considered weak shock waves (acoustic waves) propagating into any corner. Later, Keller⁴ considered the special cases where no diffractions of the regular reflected shock waves occur and determined the exact solutions by algebraic means. Schniffman et al.⁵ considered a series of reentrant corner problems, most of which involved 90° corners. Some of these corners had one finite length wall. For corners formed at non-right angles, they considered only regular reflection within an infinitely long corner and used approximations to the oblique shock relations in order to obtain estimates of the resulting pressure field. In Section 3.1, an analytic model is presented and the extension of the model to simple Mach reflection is made. The only restriction on the corner angle and shock strength is that complex and double Mach reflections do not occur within the corner. Under the assumptions of the analytic model, the flow field within the corner can be analyzed as a cascading series of step shock reflections, except for possibly the final reflected shock. The model predicts the propagation of all the shocks within the corner, determines the type of reflection occurring at each reflection point within the corner, and calculates the gas states and shock wave parameters associated with each reflection. The flow field resulting from a shock wave propagating into an infinite two-dimensional corner can be solved algebraically provided that the final reflected shock is not diffracted as shown by Keller. However, if any shock is diffracted by either the leading edge of a finite corner or the final reflection process, no exact analytic treatment is possible. In these cases, an approximate technique (numerical or analytic) must be used. The present analytic model provides an exact solution of the flow field if no diffraction occurs and an approximation of the peak vertex pressure which is comparable with experimental results if diffraction occurs. The flow fields behind both weak and moderate strength incident shock waves propagating into an infinitely long corner are calculated in Section 3.2. When the corner has finite length, the rarefaction wave generated at the leading edge of the corner propagates into the corner and decreases the maximum vertex pressure. In Section 3.3, a formula is derived using the results of Section 3.1 to determine the duration of the peak vertex pressure in a finite corner.

3. Keller, J.B. and Blank, A., "Diffraction and Reflection of Pulses by Wedges and Corners", *Communs. Pure and Appl. Math.*, Vol. IV, No. 1, pp. 75-94, 1951.
4. Keller, J.B., "Multiple Shock Reflection in Corners", *Journal of Applied Physics*, Vol. 25, No. 5, pp. 558-590, 1954.
5. Schniffman, T., Heyman, R.J., Sherman, A., and Weimer, D., "Pressure Multiplication in Re-Entrant Corners", in *Proceedings of the First Shock Tube Symposium*, Air Force Weapons Center Report No. SWR-TM-57-2 (AD467-201), 1957.

The numerical simulation of a shock wave propagation into a infinite reentrant corner by the DORF hydrodynamic computer code is described in Section 4. The DORF code solves a finite difference representation of the two-dimensional Euler equations in an Eulerian computational grid. The continuum being modeled is divided into rectangular zones, or cells, each of which represents a given mass of either pure or mixed material in a state of thermodynamic equilibrium. The DORF code can model non-responding cells in the computational flow field. These are used to construct interior reflecting boundaries and rigid structures. A description of the DORF algorithm is given in Section 4.1.

The geometry of a general reentrant corner is not easily modeled with the DORF code. It is necessary to use the two-dimensional Cartesian configuration which has a 90° angle between the x and y axes. One or both of the axes must be modified to model a non-right angle at the apex of a reentrant corner. Because the code is limited to the orthogonal Cartesian mesh, this modification can not be done by rotating the axes. The only means in the current version of DORF by which this can be accomplished is by stacking non-responding cells along a boundary to approximate a corner with an angle other than 90 degrees. DORF does not have the ability to model fractional cells. Consequently, the modified boundary along which the non-responding cells are stacked is not smooth, but rather consists of discrete steps. Because the pressure distributions on the walls forming a reentrant corner are of specific interest, it is important to determine what effect this stair-stepping has on the wall loading.

The DORF code has previously been used with stair-stepping to model the sides of a munition magazine⁶, a cross-section of which is a trapezoid. The trapezoidal structure was modeled as a stair-stepped ramp facing a spherical incident shock wave, followed by a rectangle and another stair-stepped ramp. The geometry used in the simulation was cylindrically symmetric. The actual ramp angles are 26.2° , measured from the horizontal. The stair-step ramps use one cell per step, each cell having an aspect ratio $\Delta r/\Delta z = 2$. Two calculations, simulating different incident shock strengths, were performed. On the forward facing ramp the calculations differ by +13% to +29% from the experimental values, on the top by -20% to +12%, and on the rearward facing ramp by +37 to +71%.

The technique of stair-stepping to model inclined surfaces has also been used in computations with the HULL⁷ hydrodynamic computer code at

6. Goodman, H.J., "Calculations of Pressure Over the Surface of a 1/30th Scale Model Munition Magazine", ARBRL-TR-02153, US Army Ballistic Research Laboratory, Aberdeen Proving Ground, MD (April 1979). (AD #B037702L)
7. Fry, M.A., Durrett, R.E., Ganong, G.P., Matuska, D.A., Stucker, M.D., Chambers, B.S., Needham, C.E., and Westmoreland, C.D., "The HULL Hydrodynamics Computer Code", AFWL-TR-76-183, US Air Force Weapons Laboratory, Kirtland Air Force Base, NM (September 1976).

the US Air Force Weapons Laboratory (AFWL). One series of HULL computations was used to determine the air blast over a dam slope⁸ caused by a nuclear burst on a surface of a reservoir. Here, the stair-stepped dam slope faces rearward relative to the on-coming shock. The results appear to be qualitatively reasonable. However, there are no experimental data with which to compare the results. Another study at AFWL attempts to determine an optimum stair-step design⁹. A discussion of the stair-step design for the reentrant corner problem as well as a critique of the AFWL method is given in Section 4.3.

The two examples of shock wave propagation which are calculated in Section 3.2 using the analytic model are recomputed using the DORF code. The DORF input values are given in Section 4.2. A comparison of the pressure profiles along the different walls is made in Section 4.4.

The experimental measurements, the analytic calculations, and the numerical computations are compared in Section 5. The peak pressure at the vertex was determined by all three methods and the results are compared in Section 5.1. In the experiments, a rarefaction wave is generated at the leading edge of the corner which ultimately decreases the vertex pressure. The values for the duration of the peak pressure measured by the experiment and determined by the analytic theory are compared in Section 5.2. The flow field within an infinite corner is modeled by both the analytic theory and the DORF calculation. The pressure histories at various stations within the corner are compared in Section 5.3.

The summary of the results and conclusions are presented in Section 6.

2. EXPERIMENTS

A series of shock tube experiments were performed at the BRL in which a step shock propagated in air perpendicularly along a shock tube wall into a corner having an vertex angle of 50° . (See Figure 2.) In reference to Figure 1, the experiments simulated a symmetrically placed shock wave into a reentrant corner with a vertex angle of $2\alpha = 100^\circ$. The shock tube wall replaces the plane of symmetry. The wall forming the corner is 0.166m long and is of sufficiently heavy construction that its response to the loading is negligible. Two pressure gages were inserted in the shock tube wall. The gage at the vertex recorded

8. Fry, M.A., Needham, C.E., Stucker, M., Chambers, B.S., III, and Ganong, G.P., "AFWL HULL Calculations of Air Blast Over a Dam Slope", AFWL-TR-76-154, US Air Force Weapons Laboratory, Kirtland Air Force Base, NM (October 1976).
9. Happ, H.J., III, Needham, C.E., and Lunn, P.W., "AFWL HULL Calculations of Square-Wave Shocks on a Ramp", AFWL-TR-77-82, US Air Force Weapons Laboratory, Kirtland Air Force Base, NM (July 1977).

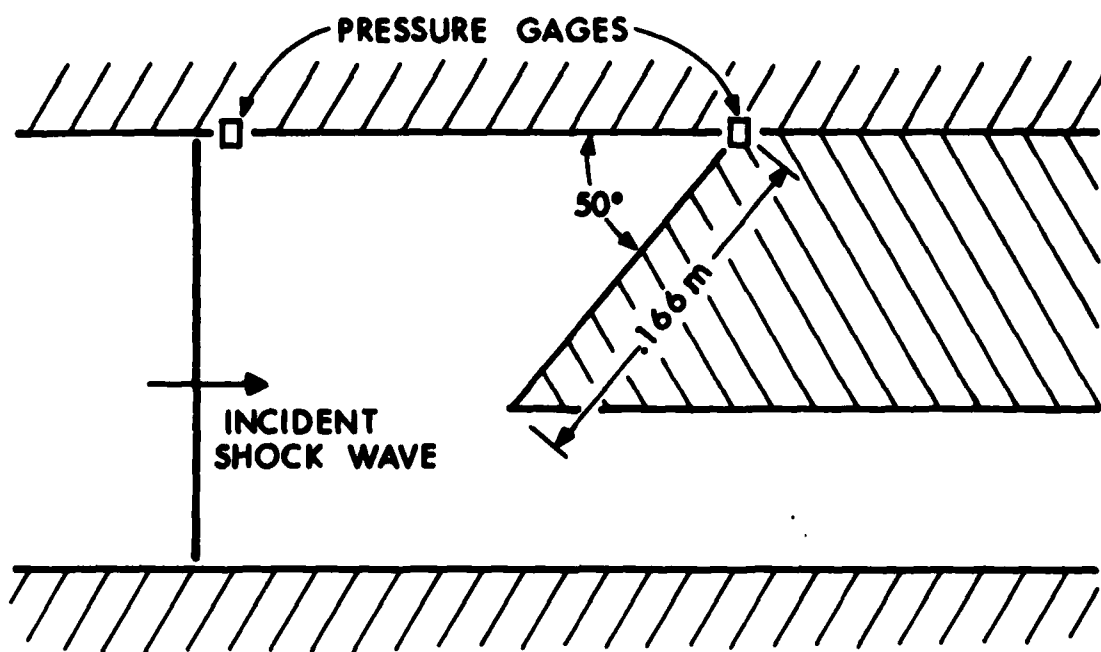


Figure 2. Schematic of the Experimental Shock Tube Model.

the pressure history. Another upstream gage determined the strength of the incident shock wave. The corner's width (254mm) was long enough to minimize three-dimensional effects.

Oscilloscope pressure-time records were obtained¹⁰ for several experiments. From these records the value of the peak overpressure at the vertex, its duration and the overpressure decay at the vertex could be determined. The more relevant experimental data are the pressure peak and its duration, because the rarefaction wave which causes the pressure decay is not explicitly modeled by either the analytical model or the numerical simulation. The estimated accuracy of the overpressure measurements is 5%. The estimated error in the peak pressure duration measurements is less than 7 μ s. A series of four experiments were performed. We shall consider only the weakest incident shock, hereafter referred to as Shot 1, and the strongest incident shock, hereafter referred to as Shot 2. The experimental values are summarized in Table 1.

3. ANALYTIC MODEL

3.1 Theory for an Infinite Corner.

The analytic model is based on four assumptions:

a. The incident shock propagates with constant velocity and is symmetrically placed within the corner at its mid-plane. (See Figure 1.) This hypothesis permits the two-dimensional analysis of a shock propagating with its velocity vector parallel to the plane of symmetry (a rigid wall) into a corner which has an acute angle equal to the bisected angle of the physical corner. This assumption, of course, can be ignored, if the incident shock front is already propagating perpendicularly to a wall. Because the incident shock velocity is constant, its propagation can be considered pseudostationary if a frame of reference is attached to the shock.

b. The medium in which the shock wave propagates is a perfect gas and has negligible viscosity. The latter part of this assumption excludes the formation of boundary layers along the wall, and enables us to treat shock waves as discontinuous surfaces. Following the derivation in Thompson¹¹ or Courant and Friedrichs¹² (see APPENDIX A), the jump conditions

10. Taylor, W.J., ARRADCOM, BRL, Private communication.

11. Thompson, P.A., Compressible Fluid Dynamics, McGraw-Hill Book Co., New York, 1972.

12. Courant, R. and Friedrichs, K.O., Supersonic Flow and Shock Waves, Vol. 1, Interscience Publishers, Inc., New York, 1948.

Table 1. Summary of Experimental Shots.

Designation	P_0	T_0	P_1/P_0	Incident Overpressure	Peak Absolute Pressure at the Vertex	Peak Overpressure at the Vertex	Duration of Peak Pressure at the Vertex
Shot 1	100.8 kPa	295.44 K	1.12	12.4 kPa	154.6 kPa	53.8 kPa	131 μ s
Shot 2	100.7 kPa	295.48 K	2.37	138. kPa	1.82 MPa	1.719 MPa	22 μ s

across a planar discontinuity can be written as:

$$\rho_b (\vec{v}_b - \vec{w}) \cdot \vec{n} - \rho_a (\vec{v}_a - \vec{w}) \cdot \vec{n} = 0, \quad (3.1.1)$$

$$\rho_b [(\vec{v}_b - \vec{w}) \cdot \vec{n}]^2 - \rho_a [(\vec{v}_a - \vec{w}) \cdot \vec{n}]^2 = P_a - P_b, \quad (3.1.2)$$

$$\vec{v}_b \cdot \vec{t} - \vec{v}_a \cdot \vec{t} = 0, \quad (3.1.3)$$

$$h_b + 0.5(\vec{v}_b \cdot \vec{n})^2 - h_a - 0.5(\vec{v}_a \cdot \vec{n})^2 = \vec{w} \cdot (\vec{v}_b - \vec{v}_a), \quad (3.1.4)$$

where ρ , \vec{v} , P , h , \vec{w} , \vec{n} , \vec{t} are the density, velocity, pressure, specific enthalpy, the shock wave velocity, the unit outer normal vector to the shock wave, and the unit tangential vector to the shock wave, respectively. The properties immediately ahead of the shock wave are denoted by the subscript a and those immediately behind by the subscript b. The perfect gas assumption postulates an equation of state of the form $h = \gamma P / [(\gamma - 1)\rho]$ where γ is the ratio of two constants (the specific heat at constant pressure c_p and specific heat at constant volume c_v). The sound speed in a perfect gas is given by $a = (\gamma P / \rho)^{1/2}$. Equations (3.1.1) - (3.1.4) are commonly known as the oblique shock relations and are valid at any point Q on the shock. If the shock is not curved in the immediate vicinity of Q, then the flow is uniform in this neighborhood and the flow properties computed at Q by the oblique shock relations are also valid in this neighborhood.

c. The walls forming the corner are rigid and infinite. The assumption of wall rigidity is reasonable if the time duration of the loading is short relative to the response time of the wall. The infinite extent of the walls eliminates the rarefaction wave which is generated at the leading edge of the corner and causes the curvature of some reflected shocks.

d. Only regular and simple Mach reflections occur within the corner. This restriction is necessary because only these types of reflections are modeled. The theory of the model identifies the type of shock reflection and permits one to carry out a corresponding analysis.

The initial conditions for the shock reflection analysis are the absolute pressure P_0 and temperature T_0 in the undisturbed medium, the incident shock strength and the angle of the apex 2α . From the initial

pressure value and shock strength, the pressure behind the incident shock can be computed. In a perfect gas, the initial density ρ_0 is given by $\rho_0 = P_0 / (T_0 R^*)$, where R^* is the gas constant, and the initial enthalpy is given by $h_0 = \gamma P_0 / [(\gamma - 1) \rho_0]$.

The theory for the regular reflection of a shock wave in a perfect gas from a solid boundary is well known.^{13, 14} Consider a step shock wave I which is propagating with a constant velocity, is incident at point Q upon an infinite plane rigid wedge making an angle θ_w with the horizontal, and causes a regular reflected shock R to arise from the wedge. If we attach a frame of reference to the point Q, the incident shock velocity is zero and the flow in region 0 toward I is parallel to the wedge surface. (See Figure 3.) We define the region upstream of I as region 0, downstream of I and upstream of R as region 1, and downstream of R as region 2. The properties in regions 0, 1, and 2 are related in a neighborhood of the reflection point Q. While passing through the incident shock at an angle of $\phi_0 = 90^\circ - \theta_w$, the flow is deflected from its original direction towards I by an angle θ_1 and its dynamic and thermodynamic properties are changed. These properties are related by the oblique shock relations (3.1.1)-(3.1.4) in the neighborhood of point Q. In these circumstances, the oblique shock relations can be simplified by substituting

$$\vec{u}_a = \vec{v}_a - \vec{w},$$

$$\vec{u}_b = \vec{v}_b - \vec{w},$$

$$\vec{u}_a \cdot \vec{n} = u_0 \sin \phi_0,$$

$$\vec{u}_b \cdot \vec{n} = u_1 \sin (\phi_0 - \theta_1),$$

$$\vec{u}_a \cdot \vec{t} = u_0 \cos \phi_0,$$

$$\vec{u}_b \cdot \vec{t} = u_1 \cos (\phi_0 - \theta_1),$$

and can be rewritten using the equivalent (A10) instead of (3.1.4) as:

$$\rho_1 u_1 \sin (\phi_0 - \theta_1) = \rho_0 u_0 \sin \phi_0, \quad (3.1.5)$$

$$P_1 + \rho_1 [u_1 \sin (\phi_0 - \theta_1)]^2 = P_0 + \rho_0 [u_0 \sin \phi_0]^2, \quad (3.1.6)$$

$$u_1 \cos (\phi_0 - \theta_1) = u_0 \cos \phi_0, \quad (3.1.7)$$

$$h_1 + 0.5 [u_1 \sin (\phi_0 - \theta_1)]^2 = h_0 + 0.5 [u_0 \sin \phi_0]^2, \quad (3.1.8)$$

13. Bleakney, W. and Taub, A.H., "Interaction of Shock Waves", Review of Modern Physics, 21, pp. 584-605, 1949.
14. Polachek, H. and Seeger, R., "Shock Wave Interactions" in Fundamentals of Gas Dynamics, H.W. Emmons, Ed., Princeton University Press, pp. 494-504, 1958.

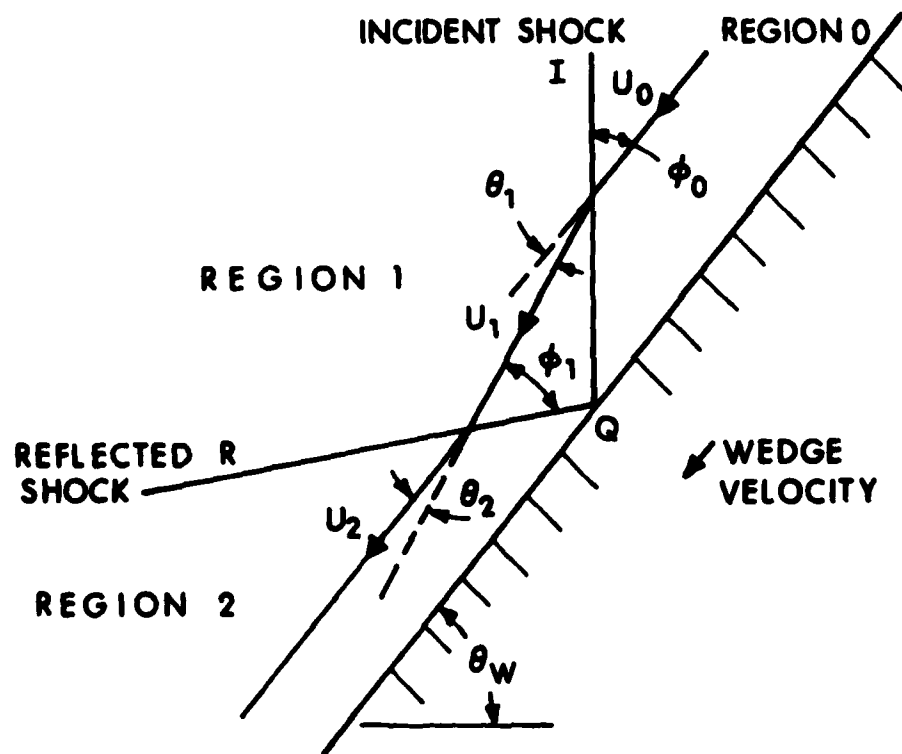


Figure 3. Regular Reflection in a Neighborhood of the Reflection Point Q.

where we define $u_1 = |\vec{u}_1|$. Equations (3.1.5)-(3.1.8) represent a system of four nonlinear algebraic equations with four unknowns, u_0 , ρ_1 , u_1 and θ_1 , because $h_1 = \gamma P_1 / [(\gamma-1)\rho_1]$. The solution of this system is obtained easily, and the explicit formulas for the unknowns are derived in the APPENDIX B. These formulas determine the flow in region 1 and are independent of the type of reflection occurring at the point Q.

The flow deflection across the incident shock causes the flow in region 1 in the neighborhood of Q to approach the reflected shock obliquely at an angle ϕ_1 . While passing through the reflected shock R, the flow is deflected towards it by an angle θ_2 from its region 1 trajectory and its dynamic and thermodynamic properties are altered. These properties are related by the oblique shock relations (3.1.1)-(3.1.4) in the neighborhood of Q. In this case, the velocities are

$$\vec{u}_a \cdot \vec{n} = u_1 \sin \phi_1, \quad \vec{u}_b \cdot \vec{n} = u_2 \sin (\phi_1 - \theta_2),$$

$$\vec{u}_a \cdot \vec{t} = u_1 \cos \phi_1, \quad \vec{u}_b \cdot \vec{t} = u_2 \cos (\phi_1 - \theta_2).$$

In order that the resulting flow in region 2 adjacent to the wall be parallel to the wall in the neighborhood of Q, the deflection angles must be equal, that is, $\theta_2 = \theta_1$. In this framework both θ_1 and θ_2 are positive angles and the difference in deflection direction is incorporated in the formulation. The oblique shock relations for the reflected shock R can be written in the form:

$$\rho_2 u_2 \sin (\phi_1 - \theta_1) = \rho_1 u_1 \sin \phi_1, \quad (3.1.9)$$

$$u_2 \cos (\phi_1 - \theta_1) = u_1 \cos \phi_1, \quad (3.1.10)$$

$$P_2 + \rho_2 [u_2 \sin (\phi_1 - \theta_1)]^2 = P_1 + \rho_1 [u_1 \sin \phi_1]^2, \quad (3.1.11)$$

$$h_2 + 0.5 [u_2 \sin (\phi_1 - \theta_1)]^2 = h_1 + 0.5 [u_1 \sin \phi_1]^2. \quad (3.1.12)$$

In this system of equations, ρ_1 , u_1 , P_1 , h_1 and θ_1 , are known. Thus, equations (3.1.9)-(3.1.12) represent four nonlinear equations in P_2 , ρ_2 , u_2 , and ϕ_1 when the enthalpy h_2 is expressed in terms P_2 and ρ_2 .

The solution to this system cannot be obtained by explicit formulas. Instead the solution can be obtained numerically by using the IMSL subroutine ZSYSTEM¹⁵. (ZSYSTEM solves a system of N simultaneous nonlinear equations in N unknowns by using Brown's technique¹⁶.)

The described method determines the entire flow field in the neighborhood of Q in a shock-fixed coordinate system from the given initial conditions. Performing a simple transformation of the velocities gives the solution in the laboratory coordinate system. Furthermore, this flow configuration can be verified experimentally for a class of incident shock strengths and wall angles. For large incident angles ϕ_0 and/or strong shocks, the equation system may not have a solution. In such cases a so-called "Mach reflection" takes place.

The theory of single Mach reflections from a solid boundary is discussed in References 14, 17, and 18. We extend this theory to include the case of an incident shock propagating into a nonquiescent region. Consider a step shock wave I which is incident upon a plane rigid wall that makes an angle θ_w with the horizontal, and which causes a Mach reflection to arise on the wall. The gas velocity ahead of the shock wave is towards I and is parallel to the wedge. The frame of reference is attached to the triple point Z. (See Figure 4.) The incident shock I, reflected shock R, and the Mach stem M emanate from Z as does the slip line. The trajectory of Z is a straight line with angle χ between it and the wall surface. The region upstream of I and M is denoted by region 0, upstream of R and downstream of I by region 1, downstream of R by region 2, and downstream of M by region 3. The slip line divides regions 2 and 3 which have equal pressures and equal flow directions with different speeds in this reference frame. We correlate the properties in these four regions in the immediate vicinity of the triple point. In this shock-fixed coordinate system, the incident shock velocity is zero and the gas velocity in region 0 relative to the wall velocity is parallel to the wall surface. The portion of the flow in region 0 which passes through I makes an angle

$$\phi_0 = \tan^{-1} \frac{v_{0x} + w}{v_{0y} + w \tan(\theta_w + \chi)} \quad (3.1.13)$$

15. International Mathematical and Statistical Libraries, Inc., IMSL Library 3, Edition 6, IMSL, Houston, Texas, 1977.
16. Brown, K.M., "A Quadratically Convergent Newton-Like Method Based Upon Gaussian Elimination", SIAM Journal of Numerical Analysis, Vol. 6, No. 4, pp. 560-569, 1969.
17. Law, C.K., "Diffraction of Strong Shock Waves by a Sharp Compressive Corner", University of Toronto Institute for Aerospace Studies Technical Note No. 150, 1970.
18. Ben Dor, G., "Regions and Transitions of Nonstationary Oblique Shock Wave Diffractions in Perfect and Imperfect Gases", University of Toronto Institute for Aerospace Studies Technical Report No. 232, 1978.

with 1 where v_{0x} , v_{0y} , and w are the x and y components of the gas velocity in region 0 and the incident shock speed in the laboratory coordinate system, respectively. The resulting flow is then similar to that described in the regular reflection case except that now the flow in region 2 need not be parallel to the wall surface. Instead, the flow velocity \vec{u}_2 relative to the velocity of the wall must be parallel to the wall surface. With the assumption that the incident and reflected shocks are straight line shocks (i.e. not curved) at least in a neighborhood of Z, the oblique shock relations which now relate uniform flow properties in regions 0, 1 and 2 are:

$$\rho_1 u_1 \sin(\phi_0 - \theta_1) = \rho_0 u_0 \sin \phi_0, \quad (3.1.14)$$

$$P_1 + \rho_1 [u_1 \sin(\phi_0 - \theta_1)]^2 = P_0 + \rho_1 [u_0 \sin \phi_0]^2, \quad (3.1.15)$$

$$u_1 \cos(\phi_0 - \theta_1) = u_0 \cos \phi_0, \quad (3.1.16)$$

$$h_1 + 0.5[u_1 \sin(\phi_0 - \theta_1)]^2 = h_0 + 0.5[u_0 \sin \phi_0]^2, \quad (3.1.17)$$

$$\rho_2 u_2 \sin(\phi_1 - \theta_2) = \rho_1 u_1 \sin \phi_1, \quad (3.1.18)$$

$$P_2 + \rho_2 [u_2 \sin(\phi_1 - \theta_2)]^2 = P_1 + \rho_1 [u_1 \sin \phi_1]^2, \quad (3.1.19)$$

$$u_2 \cos(\phi_1 - \theta_2) = u_1 \cos \phi_1, \quad (3.1.20)$$

$$h_2 + 0.5[u_2 \sin(\phi_1 - \theta_2)]^2 = h_1 + 0.5[u_1 \sin \phi_1]^2. \quad (3.1.21)$$

The portion of the flow in region 0 which passes through the Mach stem makes an angle ϕ_M with M. In general, the Mach stem will be a curved shock, so ϕ_M will vary with position along the Mach stem. While passing through the Mach stem, the flow is deflected from its original direction by an angle θ_3 and its dynamic and thermodynamic properties are changed. If the Mach stem is straight in a neighborhood of Z, the flow is uniform in that vicinity. These properties are related by the oblique shock relations (3.1.1)-(3.1.4). For the Mach stem the oblique shock relations can be simplified with

$$\begin{aligned} \vec{u}_a \cdot \vec{n} &= u_0 \sin \phi_M, & \vec{u}_b \cdot \vec{n} &= u_3 \sin(\phi_M - \theta_3), \\ \vec{u}_a \cdot \vec{t} &= u_0 \cos \phi_M, & \vec{u}_b \cdot \vec{t} &= u_3 \cos(\phi_M - \theta_3); \end{aligned}$$

and rewritten as:

$$\rho_3 u_3 \sin (\phi_M - \theta_3) = \rho_0 u_0 \sin \phi_M, \quad (3.1.22)$$

$$u_3 \cos (\phi_M - \theta_3) = u_0 \cos \phi_M, \quad (3.1.23)$$

$$P_3 + \rho_3 [u_3 \sin (\phi_M - \theta_3)]^2 = P_0 + \rho_0 [u_0 \sin \phi_M]^2, \quad (3.1.24)$$

$$h_3 + 0.5[u_3 \sin (\phi_M - \theta_3)]^2 = h_0 + 0.5[u_0 \sin \phi_M]^2. \quad (3.1.25)$$

Furthermore, the flow fields in regions 2 and 3 are related across the slipline because equal pressures exist and the same flow direction occurs near the slipline:

$$P_3 = P_2, \quad (3.1.26)$$

$$\theta_3 = \theta_1 - \theta_2. \quad (3.1.27)$$

For the special case where $\chi = 0$, the triple point Z attaches to the wall and the slipline and region 3 are nonexistent. If one allows $\theta_3 = 0$, equations (3.1.13)-(3.1.21) and equation (3.1.27) reduce to the regular reflection case. For $\chi \neq 0$, equations (3.1.13)-(3.1.27) represent 15 equations in 16 unknowns χ , ϕ_0 , u_0 , ρ_1 , u_1 , θ_1 , ϕ_1 , θ_2 , ρ_2 , P_2 , u_2 , ϕ_M , θ_3 , ρ_3 , P_3 , and u_3 when the initial conditions (P_0 , P_1 , T_0 , θ_w , v_{0x} , and v_{0y}) are given. The perfect gas relations $\rho = P/(TR^*)$ and $h = \gamma P/[(\gamma-1)\rho]$ are assumed. In order to obtain the missing 16th equation, the entire Mach stem is assumed to be a straight line shock. Experiments have shown that except for strong diffractions, the Mach stem is only slightly curved¹⁷. Therefore this assumption does not introduce gross errors. It is equivalent to the assumption of a uniform flow field about the Mach stem. Because the flow adjacent to the wall must remain parallel to the wall's surface after passing through the Mach stem in the laboratory coordinate system, the Mach stem must intersect the wall at 90°. Consequently, we have the following geometric relation

$$\phi_M = \phi_0 + \theta_w \quad (3.1.28)$$

along the entire Mach stem. Equations (3.1.13)-(3.1.28) form a system of 16 nonlinear equations in 16 unknowns which determines the flow field in the neighborhood of Z when the initial conditions in Region 0 and the incident shock I are given.

For nonstationary flow, the criteria for distinguishing between the sundry types of reflections are contained in References 14 and 18. Reflection occurs if the flow behind the incident shock is non-subsonic in the shock-fixed coordinate system. Figure 5 delineates the regions of regular reflection (bottom section) from Mach reflections (top section) in the angle of incidence - inverse shock strength plane. The curve labeled ϕ_e is the limiting curve above which regular reflection is theoretically impossible. The curve labeled ϕ_c is the limiting curve below which the past history can not affect the reflection process. The experimental points indicate the smallest incident angle at which Mach reflection has been observed. The termination of Mach reflection occurs when the Mach number in the shock-fixed coordinate system of region 2 is equal to or greater than one.

The implementation of the regular and Mach reflection theories to form the analytic model for shock wave propagation into a reentrant corner is best illustrated by examples. Such examples are given in Section 3.2. In the next subsection the theory is used to compute the two shock tube experiments described in Section 2.

3.2. Examples.

In the experiments, the walls forming the corners do not have infinite extent. This limits the model's predictions to finite times after the incident shock reaches the vertex. To obtain the complete history of the vertex pressure, a hydrodynamic computer code simulation of the entire experiment must be performed.

Consider the incident step shock from Shot 2 with $P_1/P_0 = 2.3699$ which propagates into an infinite reentrant corner with vertex angle 50° . (See Figure 6.) From the geometry, the incident angle is $\phi_0 = 40^\circ$. The medium is assumed to have constant specific heats $c_v = 714.0 \text{ J/(kg}\cdot\text{K)}$ and $c_p = 1001. \text{ J/(kg}\cdot\text{K)}$, and a gas constant $R = 287.03 \text{ J/(kg}\cdot\text{K)}$. The initial conditions in region 0 are $P_0 = 100.66 \text{ kPa}$, $T_0 = 295.48 \text{ K}$, and zero gas velocity in the laboratory coordinate system with its origin at the vertex. Consider a point Q on the corner wall at which the incident shock impinges. If we make a Galilean transformation at Q, we can apply the formulas in Appendix B. In the shock-fixed coordinate system, we compute $\rho_1 = 2.1561 \text{ kg/m}^3$, $u_1 = 667.35 \text{ m/s}$, $T_1 = 385.45 \text{ K}$, $\theta_1 = 15.208^\circ$ and $a_1 = 393.84 \text{ m/s}$. Because the flow is supersonic in region 1, reflection occurs at Q. The point ($\phi_0 = 40^\circ$ and $P_1/P_0 = 0.4168$) in Figure 5 falls below the ϕ_e curve, and thus regular reflection occurs at Q. Solving the four equations governing regular reflection, equations (3.1.9)-(3.1.12), in the neighborhood of Q with ZSYSTEM

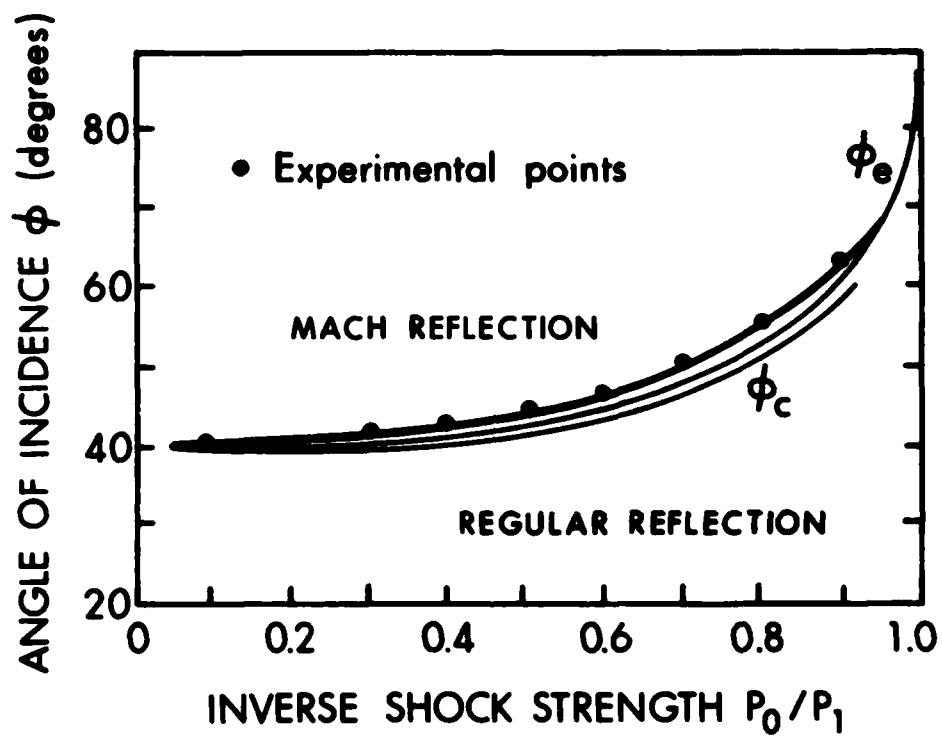


Figure 5. Criterion for Determining the Presence of Regular and Mach Reflection (Adapted from Reference 14).

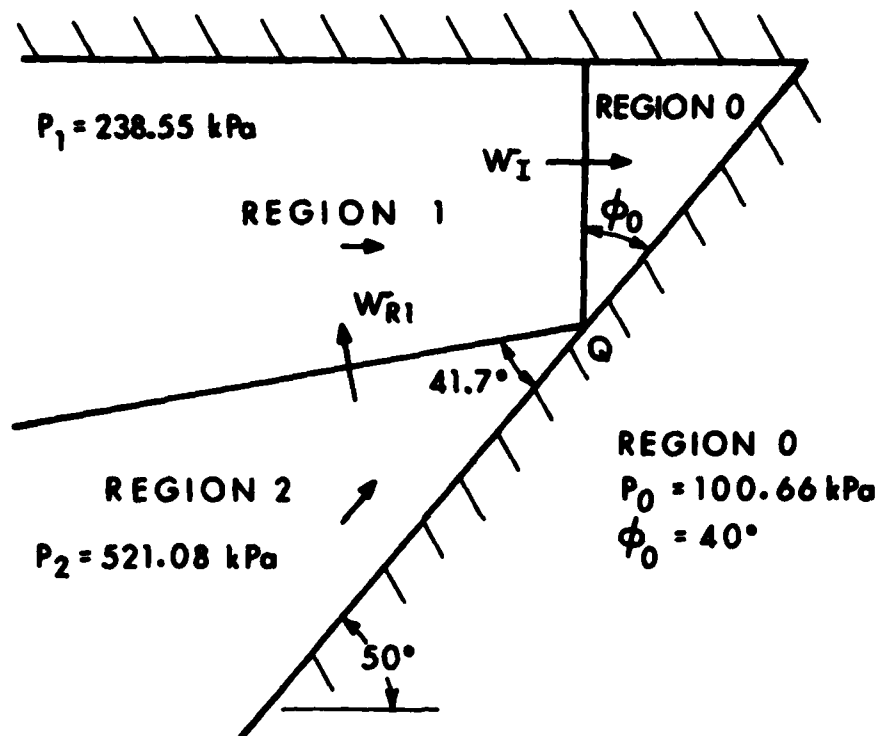


Figure 6. Flow Field Before the Incident Shock Reaches the Vertex for Shot 2.

we obtain $\rho_2 = 3.7132 \text{ kg/m}^3$, $u_2 = 488.09 \text{ m/s}$, $P_2 = 521.08 \text{ kPa}$, and $\phi_1 = 56.893^\circ$. (These results were obtained with ZSYSTEM termination parameters $\text{EPS} = 10^{-10}$, $\text{NSIG} = 13$ and $\text{ITMAX} = 100$.) From geometric considerations, the angle of reflection is 41.685° . With the assumption of an infinite corner, rarefaction waves do not exist within the corner, and the incident and reflected shock remain straight. Thus, the gas properties behind these shocks are uniform and the values of the flow properties calculated in the neighborhood of Q are those behind the entire extent of the shocks. Upon transforming back to the laboratory coordinates, we obtain the configuration depicted in Figure 6. The gas properties in regions 0, 1 and 2 are summarized in Table 2. (The velocities are denoted by u in the shock-fixed coordinate system and by v in the laboratory coordinate system.) The speeds of the incident and first reflected shocks are denoted by w_I and w_{R1} , respectively. The velocities in the laboratory coordinates in regions 1 and 2 are parallel to the plane of symmetry and the corner wall, respectively. The angle of incidence is not equal to the angle of reflection and this one reflection process has already increased the pressure near the wall by a factor of 5.18.

The pseudo-steady flow of Figure 6 remains unchanged until the incident shock reaches the apex. At that instant only the first reflected shock remains (only regions 1 and 2). This shock continues to propagate along the plane of symmetry with an angle of 8.315° and a speed of 3637.0 m/s . With an inverse strength of $P_1/P_2 = .4578$, regular reflection occurs at any reflection point Q' according to Figure 5. (See Figure 7.) Because the flow properties are already calculated in regions 1 and 2, only the flow in region 3 must be calculated. We make a Galilean transformation at Q' . In this shock-fixed coordinate system, the velocity magnitudes are $u_1 = 3865.52 \text{ m/s}$ and $u_2 = 3838.63 \text{ m/s}$ in and the flow deflection angle across the shock is 3.464° . Solving the four equations governing regular reflection, equations (3.1.9)-(3.1.12), in the neighborhood of point Q' with identical ZSYSTEM termination parameters as before, we obtain $\rho_3 = 6.0394 \text{ kg/m}^3$, $u_3 = 3808.8 \text{ m/s}$, $P_3 = 1.045 \text{ MPa}$, and $\phi_2 = 9.069^\circ$. From geometric considerations, the angle of reflection is 5.605° . With the infinite corner assumption, the second reflected shock remains straight and the gas properties behind the shock are uniform. Thus, the values of the flow properties calculated in the neighborhood of Q' are those behind the entire extent of the second reflected shock. Upon transforming back to the laboratory coordinates, we obtain the flow field in Figure 7 with respect to regions 1, 2 and 3. The gas properties of region 3 are given in Table 2. The gas velocity in region 3 is parallel to the plane of symmetry. The speed of the second reflected shock is denoted by w_{R2} .

Table 2. Regional Flow Properties for Shot 2 in Laboratory Coordinates.

<u>Region 0</u>	<u>Region 1</u>	<u>Region 2</u>
$P_0 = 100.66 \text{ kPa}$	$P_1 = 238.55 \text{ kPa}$	$P_2 = 521.08 \text{ kPa}$
$\rho_0 = 1.1869 \text{ kg/m}^3$	$\rho_1 = 2.1561 \text{ kg/m}^3$	$\rho_2 = 3.7132 \text{ kg/m}^3$
$T_0 = 295.48 \text{ K}$	$T_1 = 385.45 \text{ K}$	$T_2 = 488.91 \text{ K}$
$a_0 = 344.82 \text{ m/s}$	$a_1 = 393.84 \text{ m/s}$	$a_2 = 443.56 \text{ m/s}$
$v_{0x} = 0 \text{ m/s}$	$v_{1x} = 228.52 \text{ m/s}$	$v_{2x} = 194.62 \text{ m/s}$
$v_{0y} = 0 \text{ m/s}$	$v_{1y} = 0 \text{ m/s}$	$v_{2y} = 231.94 \text{ m/s}$
$w_I = 508.36 \text{ m/s}$	$w_{R1} = 525.96 \text{ m/s}$	$w_{R2} = 355.24 \text{ m/s}$
<u>Region 3</u>	<u>Region 4*</u>	<u>Region 5*</u>
$P_3 = 1.0447 \text{ MPa}$	$P_4 = 1.8913 \text{ MPa}$	$P_5 = 1.8913 \text{ MPa}$
$\rho_3 = 6.0394 \text{ kg/m}^3$	$\rho_4 = 9.1668 \text{ kg/m}^3$	$\rho_5 = 8.7707 \text{ kg/m}^3$
$T_3 = 602.65 \text{ K}$	$T_4 = 718.80 \text{ K}$	$T_5 = 751.26 \text{ K}$
$a_3 = 492.46 \text{ m/s}$	$a_4 = 537.83 \text{ m/s}$	$a_5 = 549.84 \text{ m/s}$
$v_{3x} = 171.8 \text{ m/s}$	$v_{4x} = -33.492 \text{ m/s}$	$v_{5x} = -101.90 \text{ m/s}$
$v_{3y} = 0 \text{ m/s}$	$v_{4y} = -75.358 \text{ m/s}$	$v_{5y} = -121.42 \text{ m/s}$
$w_{R3} = 479.713 \text{ m/s}$	$w_{R2'} = 497.18 \text{ m/s}$	

*These values are valid only in the neighborhood of the triple point.

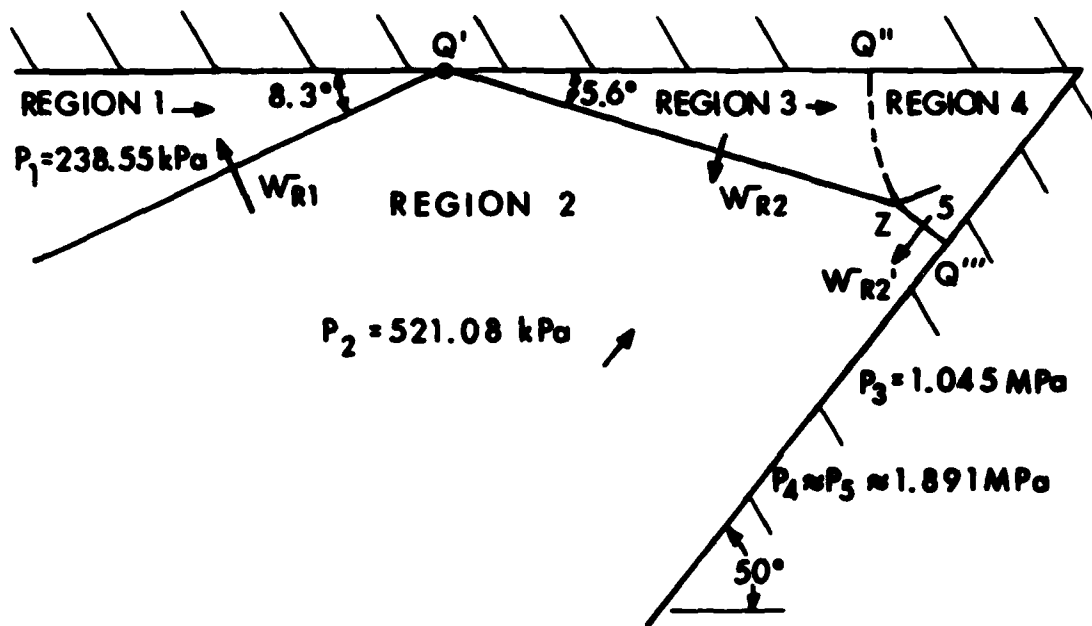


Figure 7. Flow Field Shortly After the Incident Shock Reaches the Vertex for Shot 2.

The second reflected shock will subsequently impinge on the corner wall at an angle of 55.605° . With an inverse shock strength of $P_2/P_3 = 0.4988$, Mach reflection occurs at the wall according to Figure 5. Aligning the second reflected shock with the schematic in Figure 4, the incident shock speed becomes 355.24 m/s and the gas velocity components in regions 0 and 1 are $v_{0x} = -249.84$ m/s, $v_{0y} = -171.03$ m/s, $v_{1x} = -16.781$ m/s, and $v_{1y} = -170.98$ m/s. For Mach reflections, a Galilean transformation is made at the triple point Z. The velocity of the triple point depends on an unknown χ of the configuration. Thus, in the shock-fixed coordinate system for Mach reflections, the values corresponding to $\phi_0, u_0, u_1, \theta_1$ are not known, even though in the laboratory coordinate system they are known. Because the thermodynamic properties are independent of the coordinate system, the values corresponding to P_0, P_1, ρ_0, ρ_1 are known as is the wall angle $\theta_w = 90^\circ - 55.605^\circ$. In reference to Section 3.1, we have now 15 equations and 15 unknowns (ρ_1 is now known). It was found by the first author that the solution of these equations is more simply obtained by the following procedure: (a) guess an initial value of χ, χ_G , and compute the corresponding ϕ_{M_G} from equations (3.1.13) and (3.1.28); (b) solve an appropriate subset of the equations corresponding to equations (3.1.13)-(3.1.27) for $\phi_1, \theta_1, \rho_2, P_2, u_2, \phi_{M_c}, \theta_3, \rho_3, P_3$ and u_3 with the subroutine ZSYSTEM; (c) iterate on χ until $|\phi_{M_G} - \phi_{M_c}|$ is zero within a given tolerance. Following this technique (tolerance = 10^{-4}), the solution of the flow field in the neighborhood of Z in the shock-fixed coordinate system is

$$\begin{array}{llll}
 \chi = 11.083^\circ, & \theta_1 = 13.710^\circ, & u_0 = 805.86 \text{ m/s}, & \rho_2 = 9.1668 \text{ kg/m}^3, \\
 \phi_0 = 48.664^\circ, & \theta_2 = 4.608^\circ, & u_1 = 649.33 \text{ m/s}, & \rho_3 = 8.7707 \text{ kg/m}^3, \\
 \phi_M = 83.059^\circ, & \theta_3 = 9.101^\circ, & u_2 = 434.86 \text{ m/s}, & P_2 = P_3 = 1.8913 \text{ MPa.} \\
 \phi_1 = 80.807^\circ, & & u_3 = 352.39 \text{ m/s}, &
 \end{array}$$

Table 2 lists the values of the flow variables in the laboratory coordinate system. From geometric considerations the angle between the incident shock (actually second reflected shock) and the reflected shock in the Mach configuration is 64.239° . If we extend this Mach reflected shock in a straight line to the plane of symmetry, the incident angle at the point of intersection Q'' is 110.156° (an obtuse angle). Thus, no more reflection can occur. This reflected shock must then impinge at Q'' at a right angle to the plane of symmetry so that the gas flow in the neighborhood of Q'' is parallel to the plane of symmetry. Consequently, the reflected shock must be curved to satisfy the required angles at points Z and Q'' , and the flow

properties in region 4 are not uniform. See Figure 7. The values of the flow properties in region 4 must be obtained by a hydrodynamic computer code simulation. However, an approximation of the vertex pressure value can be obtained by taking as the vertex value the pressure value calculated in the intersection of region 4 and the neighborhood of Z. Although obviously incorrect, the resulting pressure value gives a peak pressure value comparable to those of experiments while retaining the simplicity of the model. If the incident angle at Q'' were acute, Q'' would be another reflection point and the method of analysis would have continued. If the incident angle at Q'' were 90° , no further reflection would occur and the final shock would not be diffracted. In such a case, the reflected shock would remain straight, the gas properties in region 4 would be uniform, and the method would give exact values of the flow field within the entire infinite reentrant corner.

The Mach stem ZQ''' is assumed to be straight and intersects the wall at 90° according to the discussion in Section 3.1. Its speed is denoted by $w_{R2'}$. The velocity in region 5 is parallel to the wall. The pressure near the wall behind the Mach stem has increased by a factor of 18.8. A curved slipline separates regions 4 and 5 which has identical pressure values across it. The velocities in regions 4 and 5 relative to the unsteady motion of the slipline are parallel to the slipline. Because region 4 is nonuniform, the computed values are valid only in a neighborhood of the triple point and care must be used in any extrapolation. The speed of the Mach reflected shock w_{R3} is also correct only in the neighborhood of Z.

Shot 1 is analyzed in a similar fashion. Conceptually, the only difference in the analyses is that at the last reflection point, regular reflection occurs instead of Mach reflection. As before, the last shock wave is diffracted and the pressure at the final reflection point is taken as the vertex pressure value. The flow fields shortly before and after the incident shock reaches the vertex are shown in Figures 8 and 9. The regional flow properties in laboratory coordinates are summarized in Table 3.

3.3. Peak Pressure Duration for a Finite Corner.

To determine an analytic approximation for the duration of the peak pressure at the vertex of a finite corner, we use the concepts developed in Reference 19. The velocities of the incident shock wave and of the rarefaction wave generated at the leading edge of the finite corner are calculated from the values computed in Section 3.1. Using the known length of the corner wall, the time from peak pressure development (arrival of the incident shock at the vertex) to the instant the rarefaction wave reaches the vertex can be computed.

19. Smith, L.G., "Photographic Investigation of the Reflection of Plane Shocks in Air", NDRC Report No. A-350, OSRD Report No. 6271, 1945.

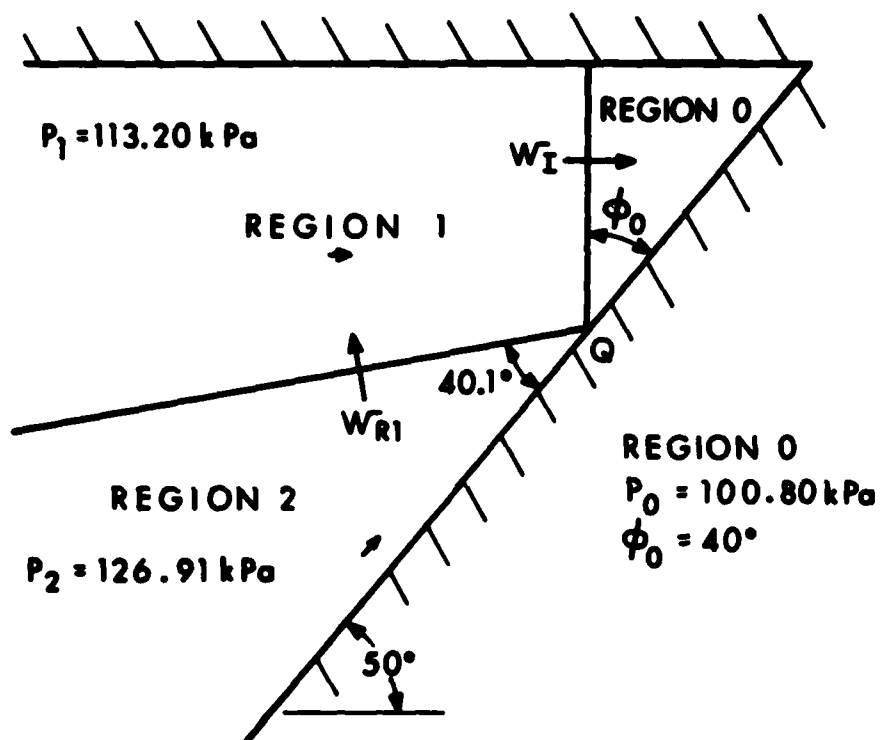


Figure 8. Flow Field Before the Incident Shock Reaches the Vertex for Shot 1.

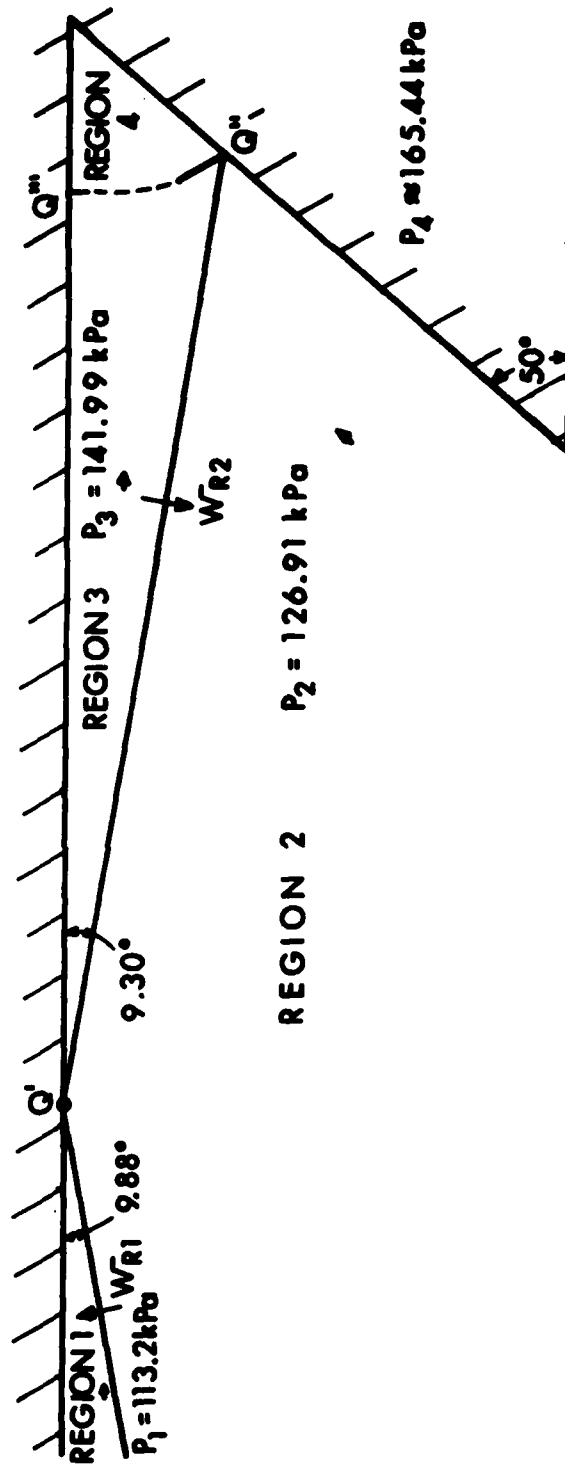


Figure 9. Flow Field Shortly After the Incident Shock Reaches the Vertex for Shot 1.

Table 3. Regional Flow Properties for Shot 1 in Laboratory Coordinates.

<u>Region 0</u>	<u>Region 1</u>	<u>Region 2</u>
$P_0 = 100.80 \text{ kPa}$	$P_1 = 113.20 \text{ kPa}$	$P_2 = 126.91 \text{ kPa}$
$\rho_0 = 1.1887 \text{ kg/m}^3$	$\rho_1 = 1.2912 \text{ kg/m}^3$	$\rho_2 = 1.4008 \text{ kg/m}^3$
$T_0 = 295.44 \text{ K}$	$T_1 = 305.45 \text{ K}$	$T_2 = 315.64 \text{ K}$
$a_0 = 344.80 \text{ m/s}$	$a_1 = 350.60 \text{ m/s}$	$a_2 = 356.40 \text{ m/s}$
$v_{0x} = 0 \text{ m/s}$	$v_{1x} = 28.79 \text{ m/s}$	$v_{2x} = 23.84 \text{ m/s}$
$v_{0y} = 0 \text{ m/s}$	$v_{1y} = 0 \text{ m/s}$	$v_{2y} = 28.40 \text{ m/s}$
$w_I = 362.51 \text{ m/s}$	$w_{R1} = 363.39 \text{ m/s}$	$w_{R2} = 342.23 \text{ m/s}$

<u>Region 3</u>	<u>Region 4*</u>
$P_3 = 141.9 \text{ kPa}$	$P_4 = 165.44 \text{ kPa}$
$\rho_3 = 1.5175 \text{ kg/m}^3$	$\rho_4 = 1.6922 \text{ kg/m}^3$
$T_3 = 325.98 \text{ K}$	$T_4 = 340.62 \text{ K}$
$a_3 = 362.19 \text{ m/s}$	$a_4 = 370.23 \text{ m/s}$
$v_{3x} = 19.2 \text{ m/s}$	$v_{4x} = -15.95 \text{ m/s}$
$v_{3y} = 0 \text{ m/s}$	$v_{4y} = -19.01 \text{ m/s}$
$w_{R3} = 370.10 \text{ m/s}$	

* These values are valid only in the neighborhood of the last reflection point.

The incident shock wave travels at a speed of $w_I/\sin \phi_0$ along the wall and traverses it in $t_w = (d_w \sin \phi_0)/w_I$, where d_w is the length of the wall. (See Figure 10a.) The rarefaction wave travels at a speed equal to the algebraic sum of the sound speed and the gas particle speed. In t_w seconds, the rarefaction wave in region 2 travels a distance $d_r = (a_2 + v_2)t_w$, because the direction of the gas velocity is toward the vertex. The remaining distance that the rarefaction wave must travel to reach the vertex is

$$\begin{aligned} d_p &= d_w - d_r \\ &= d_w \left[1 - \frac{a_2 + v_2}{w_I} \sin \phi_0 \right]. \end{aligned} \quad (3.3.1)$$

The time that the rarefaction wave takes to traverse the distance d_p is the duration of the peak apex pressure. The velocity of the rarefaction wave depends on the gas properties in regions 2, 4 and 5 for the configuration depicted in Figure 7 and the gas properties in regions 2, 3 and 4 for that given in Figure 9. Because the extent of region 3 at Q'' near the wall is small (see Figure 9) we neglect its influence on the speed of the rarefaction wave. The rarefaction wave continues to propagate into region 2 until it meets the final shock traveling at speed w_F along the wall from the vertex. (See Figure 10b.) The time at which this occurs is

$$t^* = \frac{d_p}{a_2 + v_2 + w_F}. \quad (3.3.2)$$

The time to traverse the remaining distance from their meeting point to the vertex is

$$t^+ = \frac{w_F t^*}{a_F - v_F}, \quad (3.3.3)$$

where a_F and v_F are the sound speed and gas velocity in the final region, respectively. For a_F and w_F we choose the well-defined gas properties immediately behind the last shock at the wall. These values are not accurate for the whole region, and therefore, the calculation provides only an approximation to the duration of the peak pressure. Adding equations (3.3.2) and (3.3.3), the approximation to the duration of the peak pressure is

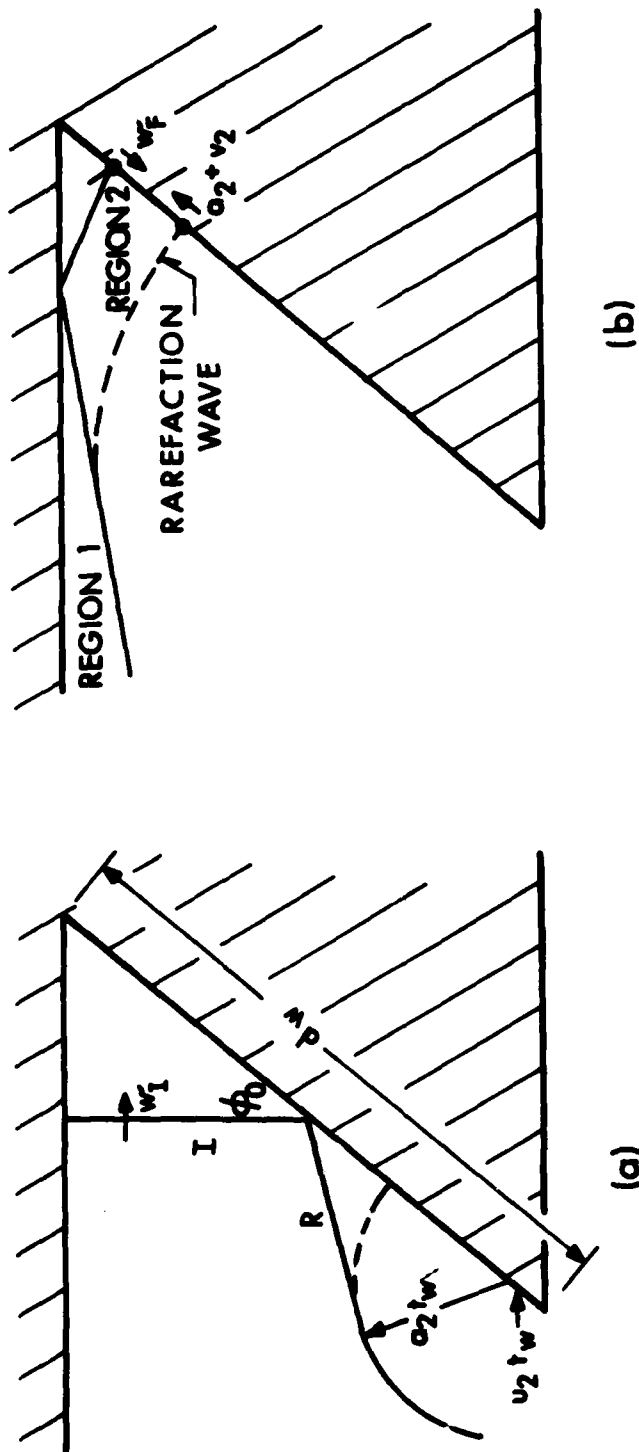


Figure 10. Rarefaction Wave Propagation Along a Finite Wall (a) Before and (b) After the Incident Shock Reaches the Vertex.

$$t^* + t^+ = \left[1 + \frac{w_F}{a_F - v_F} \right] \left[\frac{d_p}{a_2 + v_2 + w_F} \right]. \quad (3.3.4)$$

In both experimental Shots 1 and 2, the distance d_w is 0.166 m and angle ϕ_0 is 40° . For Shot 2, we use the appropriate values from Table 2 with $w_F = w_{R2'}$, $a_F = a_5$, and $v_F = v_5$ in equations (3.3.1) and (3.3.4) and compute the duration of the peak pressure to be 17.06 μ s. For Shot 1 we use the appropriate values from Table 3 with $w_F = w_{R3}$, $a_F = a_4$ and $v_F = v_4$ to obtain from equations (3.3.1) and (3.3.4) the peak pressure duration of 135.78 μ s.

4. DORF CODE SIMULATION OF AN INFINITE CORNER

4.1 DORF Code Description.

The DORF hydrodynamic computer code¹ is a two-dimensional, Eulerian, explicit code which solves the equations for conservation of mass,

$$\frac{\partial \rho}{\partial t} + \vec{\nabla} \cdot (\rho \vec{v}) = 0, \quad (4.1.1)$$

conservation of momentum,

$$\frac{\partial (\rho \vec{v})}{\partial t} + \vec{\nabla} \cdot (\rho \vec{v} \vec{v}) = - \vec{\nabla} P, \quad (4.1.2)$$

and conservation of total energy,

$$\frac{\partial (\rho E)}{\partial t} + \left[\vec{\nabla} \cdot (\rho E \vec{v}) \right] = - \vec{\nabla} \cdot (P \vec{v}), \quad (4.1.3)$$

together with an equation of state of the form

$$P = P(\rho, I), \quad (4.1.4)$$

and a sound speed equation of the form

$$a = a(\rho, P). \quad (4.1.5)$$

For the computations described in this report, the fluid is taken to be inviscid air and is assumed to be polytropic, so equation (4.1.4) becomes

$$P = \rho I (\gamma - 1), \quad (4.1.6)$$

with $\gamma = 1.402$. The particular sound speed relation is

$$a = \left[\frac{\gamma P}{\rho} \right]^{1/2}. \quad (4.1.7)$$

The momentum equation (4.1.2) is derived from the Navier-Stokes equation

$$\frac{\partial(\rho \vec{v})}{\partial t} + \vec{\nabla} \cdot (\rho \vec{v} \vec{v}) = \rho \vec{g} - \vec{\nabla} P + \vec{\nabla}(\lambda \vec{\nabla} \cdot \vec{v}) + 2(\vec{\nabla} \cdot \nu \vec{\nabla}) \vec{v} + \vec{\nabla} \times (\nu \vec{\nabla} \times \vec{v}), \quad (4.1.8)$$

by assuming the fluid to be inviscid ($\nu = \lambda = 0$) and the gravitational acceleration $\vec{g} = 0$. The energy equation (4.1.3) is derived from

$$\begin{aligned} \frac{\partial(\rho E)}{\partial t} + \left[\vec{\nabla} \cdot (\rho E \vec{v}) \right] &= \rho \vec{v} \cdot \vec{g} \\ &+ \vec{\nabla} \cdot \left\{ \tau \vec{\nabla} T - P \vec{v} + \lambda \vec{v} (\vec{\nabla} \cdot \vec{v}) \right. \\ &\left. + \frac{1}{2} \nu \vec{\nabla} (\vec{v} \cdot \vec{v}) + \nu (\vec{v} \cdot \vec{\nabla}) \vec{v} \right\}, \end{aligned} \quad (4.1.9)$$

by letting the heat transfer coefficient $\tau = 0$, and using the previous assumptions of zero viscosity and gravity.

The DORF code uses an explicit numerical method. The time step for a given sweep through the computational mesh is computed by sweeping through the entire mesh and computing, on a cell by cell basis, the minimum cell dimension

$$d_{\min} = \min(\Delta x, \Delta y), \quad (4.1.10)$$

the time step based on the sound speed in the cell

$$\Delta t_s = \frac{d_{\min}}{a}, \quad (4.1.11)$$

the time step based on the x direction particle speed

$$\Delta t_x = \frac{\Delta x}{v_x}, \quad (4.1.12)$$

and the time step based on the y direction particle speed

$$\Delta t_y = \frac{\Delta y}{v_y}. \quad (4.1.13)$$

Once these values are computed, a candidate time step based on the given cell is computed by

$$\Delta t_k = \min(\Delta t_a, \Delta t_x, \Delta t_y). \quad (4.1.14)$$

This process is repeated for each cell in the flow field with the final value for the time step to be used during the next computational cycle being

$$\Delta t = \eta \cdot \min[\Delta t_1, \Delta t_2, \dots, \Delta t_k, \dots, \Delta t_{kmax}], \quad (4.1.15)$$

where η is the Courant-Friedrichs-Lewy stability factor.

Once the time step is established, the DORF code proceeds to compute phase 1, which is the Lagrangian phase. The flux term $[\vec{v} \cdot (\rho \vec{v} \vec{v})]$ in equation (4.1.2) is temporarily dropped, leaving

$$\frac{\partial(\rho \vec{v})}{\partial t} = - \vec{v} \cdot \vec{P}, \quad (4.1.16)$$

which is used to compute the fluid acceleration caused by the pressure gradient between two adjacent flow field cells. The flux term $[\vec{v} \cdot (\rho E \vec{v})]$ in equation (4.1.3) is also dropped, leaving

$$\frac{\partial(\rho E)}{\partial t} = \vec{v} \cdot (P \vec{v}), \quad (4.1.17)$$

which is used to compute the work done at the flow field cell boundaries. In the Lagrangian phase, the continuity equation (4.1.1) becomes

$$\frac{\partial \rho}{\partial t} = 0. \quad (4.1.18)$$

Substituting equation (4.1.18) into equations (4.1.16) and (4.1.17), we obtain

$$\rho \frac{\partial \vec{v}}{\partial t} = \vec{v} \cdot \vec{P}, \quad (4.1.19)$$

and

$$\rho \frac{\partial E}{\partial t} = \vec{v} \cdot (P \vec{v}) \quad (4.1.20)$$

respectively. If we take the specific kinetic energy equation (the dot product of equation (4.1.19) with \vec{v}) and subtract it from equation (4.1.20), the equation for the specific internal energy for the Lagrangian phase is obtained. The updated Lagrangian phase values of the momentum and the specific internal energy are then computed using central spatial differences and forward time differences for the corresponding derivatives in the momentum equation (4.1.19) and the specific internal energy equation.

The initial values in the Eulerian or fluxing phase are the updated Lagrangian phase values. The governing equations in this phase are the continuity equation (4.1.1), the momentum conservation equation (4.1.2) without the stress term $-\vec{\nabla}P$,

$$\frac{\partial(\rho\vec{V})}{\partial t} = -\vec{\nabla} \cdot (\rho\vec{V}\vec{V}), \quad (4.1.21)$$

and the total energy conservation equation (4.1.3) without the work rate term $-\vec{\nabla} \cdot (P\vec{V})$,

$$\frac{\partial(\rho E)}{\partial t} = -\vec{\nabla} \cdot (\rho E\vec{V}). \quad (4.1.22)$$

The DORF code is set up so that the grid origin is at the lower left corner of the grid. The cell indexing increases monotonically when moving either upward from the origin or to the right from the origin, as do the spatial coordinates being simulated. The DORF code uses the donor cell fluxing method to update the mass, momentum, and specific total energy values. The updated value of the specific internal energy is computed by subtracting the specific kinetic energy (obtained from the updated velocities) from the updated specific total energy values. These post-Eulerian phase values are taken to be the values at the end of a given time step. Within the Eulerian phase, a logical constraint exists so that a given cell cannot flux out more material than it contains. The donor cell fluxing method is first order accurate. Thus the entire accuracy of the solution is first order. A more detailed discussion of the DORF code is found in Reference 5.

4.2. Examples.

The DORF code was used to simulate the gas flow within an infinitely long reentrant corner for the case depicted in Figure 1 with $2\alpha=100^\circ$. An infinite reentrant corner was chosen, because the corresponding gas flow is considerably simpler than the flow within a finite corner, and because a comparison of the results of DORF and the analytic model was intended. The simplification which is made possible by the existence of a plane of symmetry within the 100° corner was not exploited in the numerical simulation.

For a non-right angle corner, one of the straight walls forming the reentrant corner within the framework of the DORF code must be approximated by a stair-step. Consequently, the simulation of an 100° corner with its axis of symmetry and its more separated walls is preferable to the simulation of a 50° corner. The quantification of the effects of stair-steps is a primary objective of this numerical computation. A discussion of the different types of stair-step approximations is given in Section 4.3.

Using the DORF code we simulate the two experiments that were also analyzed by the analytic model. The initial conditions used by DORF are those obtained from the analytic model corresponding to the gas flow configuration before the incident shock reaches the vertex. For Shot 2 the initial conditions correspond to those depicted in Figure 6 and for Shot 1 those depicted in Figure 8. Because the corner's orientation for the computer calculation is different from that for the analytic calculation, and because the full 100° reentrant corner is analyzed, the direction of the velocity vectors must be modified. Figure 11 shows the initial flow field for the 100° corner based on the 50° corner analysis. Table 4 lists the initial values of density, specific internal energy ($I=c_v T$) and velocity components for Shot 2 while Table 5 lists the initial values for Shot 1. The walls forming the reentrant corner (the bottom boundary and the 10° wedge emanating from the top left corner in Figure 11) are reflective boundaries. The top and right boundaries are transmissive inflow boundaries for the present problems. However, no special boundary routine was incorporated into DORF to simulate a steady inflow. Instead, in order to avoid erroneous boundary signals from propagating into the portion of the flow field of interest, the top and right boundaries were placed sufficiently far upstream of the vertex of the reentrant corner and the incident shock. It was estimated that any waves from the boundaries theoretically travel less than 10% of the distance along the wall toward the vertex during the simulated time. The actual speed of such boundary signals in the computational domain can be monitored during the calculation, because region 2 near the transmissive boundary and along the smooth horizontal wall should remain uniform until the reflected shock emanating from the vertex reaches this region.

For the sample calculations, we chose the stability factor $\eta = 0.4$ and did not activate the artificial viscosity option. The mesh size and the stair-step approximation are discussed in the next section. The results of the DORF simulation are stated in Sections 4.4, 5.1, 5.2 and 5.3.

4.3. Stair-Step Approximation.

The computational domain is a two-dimensional Cartesian grid forming a 100° reentrant corner. The bottom boundary is a smooth reflecting boundary representing one side of the reentrant corner. (See Figure 12.) The left boundary is also a reflecting boundary, but it is along this boundary that the non-responding flow field cells are stacked to construct the other side of the reentrant corner. As may be seen in Figure 12, the actual reentrant corner side along the left boundary is approximated by a series of discrete steps. If a single computational cell per step were used with its diagonal parallel to the reentrant wall the cell would have a cell aspect ratio of

Table 4. DORF's Initial Values for Shot 2.

<u>Region 0</u>		<u>Region 1</u>	
ρ_0	$= 1.1869 \text{ kg/m}^3$	ρ_1	$= 2.1561 \text{ kg/m}^3$
I_0	$= 210.97 \text{ kJ/kg}$	I_1	$= 275.21 \text{ kJ/kg}$
v_{x0}	$= 0 \text{ m/s}$	v_{x1}	$= -146.89 \text{ m/s}$
v_{y0}	$= 0 \text{ m/s}$	v_{y1}	$= -175.06 \text{ m/s}$
<u>Regions 2 and 2'</u>		$\beta = 41.685^\circ$	
$\rho_2 = \rho_{2'}$	$= 3.7132 \text{ kg/m}^3$		
$I_2 = I_{2'}$	$= 349.08 \text{ kJ/kg}$		
v_{x2}	$= -302.78 \text{ m/s}$		
v_{y2}	$= 0 \text{ m/s}$		
$v_{x2'}$	$= 39.68 \text{ m/s}$		
$v_{y2'}$	$= -225.05 \text{ m/s}$		

Table 5. DORF's Initial Values for Shot 1.

<u>Region 0</u>	<u>Region 1</u>
$\rho_0 = 1.1887 \text{ kg/m}^3$	$\rho_1 = 1.2912$
$I_0 = 210.94 \text{ kJ/kg}$	$I_1 = 218.09 \text{ kJ/kg}$
$v_{x0} = 0 \text{ m/s}$	$v_{x1} = -18.506 \text{ m/s}$
$v_{y0} = 0 \text{ m/s}$	$v_{y1} = -22.054 \text{ m/s}$
 <u>Regions 2 and 2'</u>	 $\beta = 40.116^\circ$
$\rho_2 = \rho_{2'} = 1.4008 \text{ kg/m}^3$	
$I_2 = I_{2'} = 225.37 \text{ kJ/kg}$	
$v_{x2} = -37.079 \text{ m/s}$	
$v_{y2} = 0 \text{ m/s}$	
$v_{x2'} = 6.4387 \text{ m/s}$	
$v_{y2'} = -36.516 \text{ m/s}$	

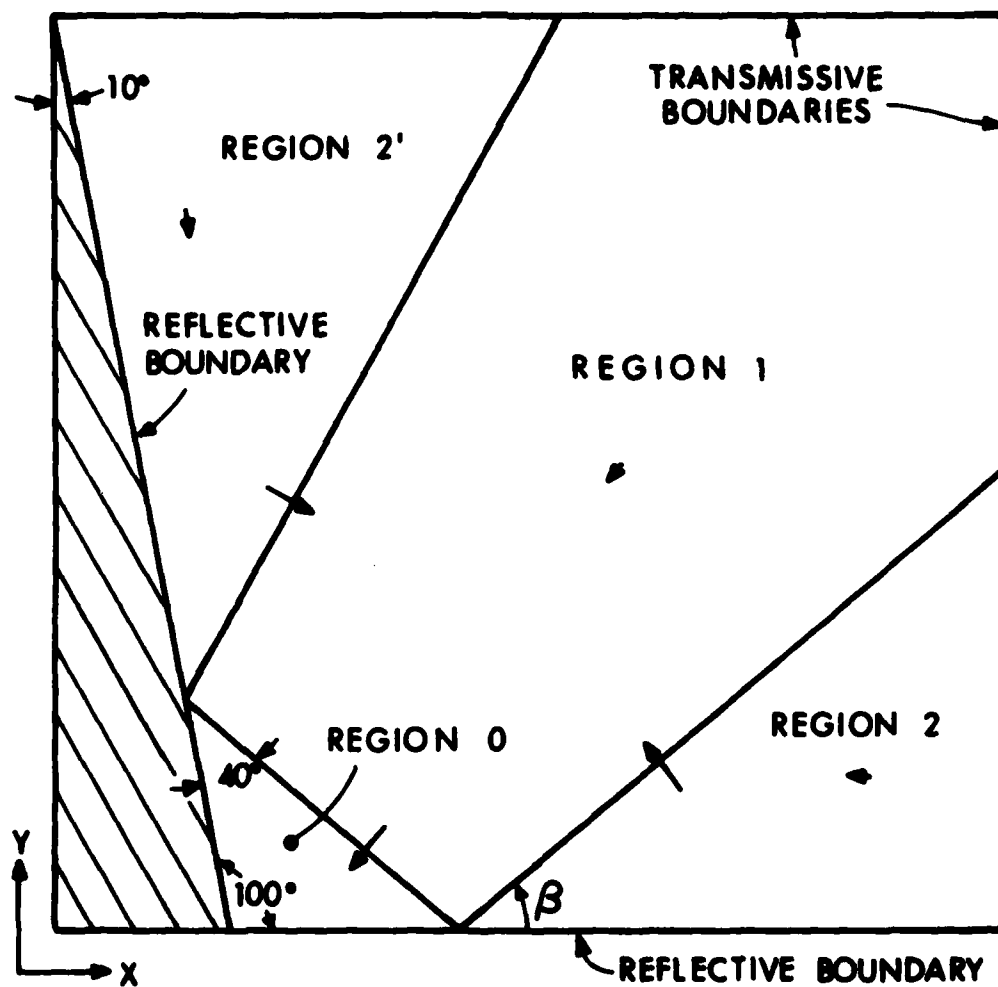


Figure 11. Initial Flow Field for DORF Simulations.

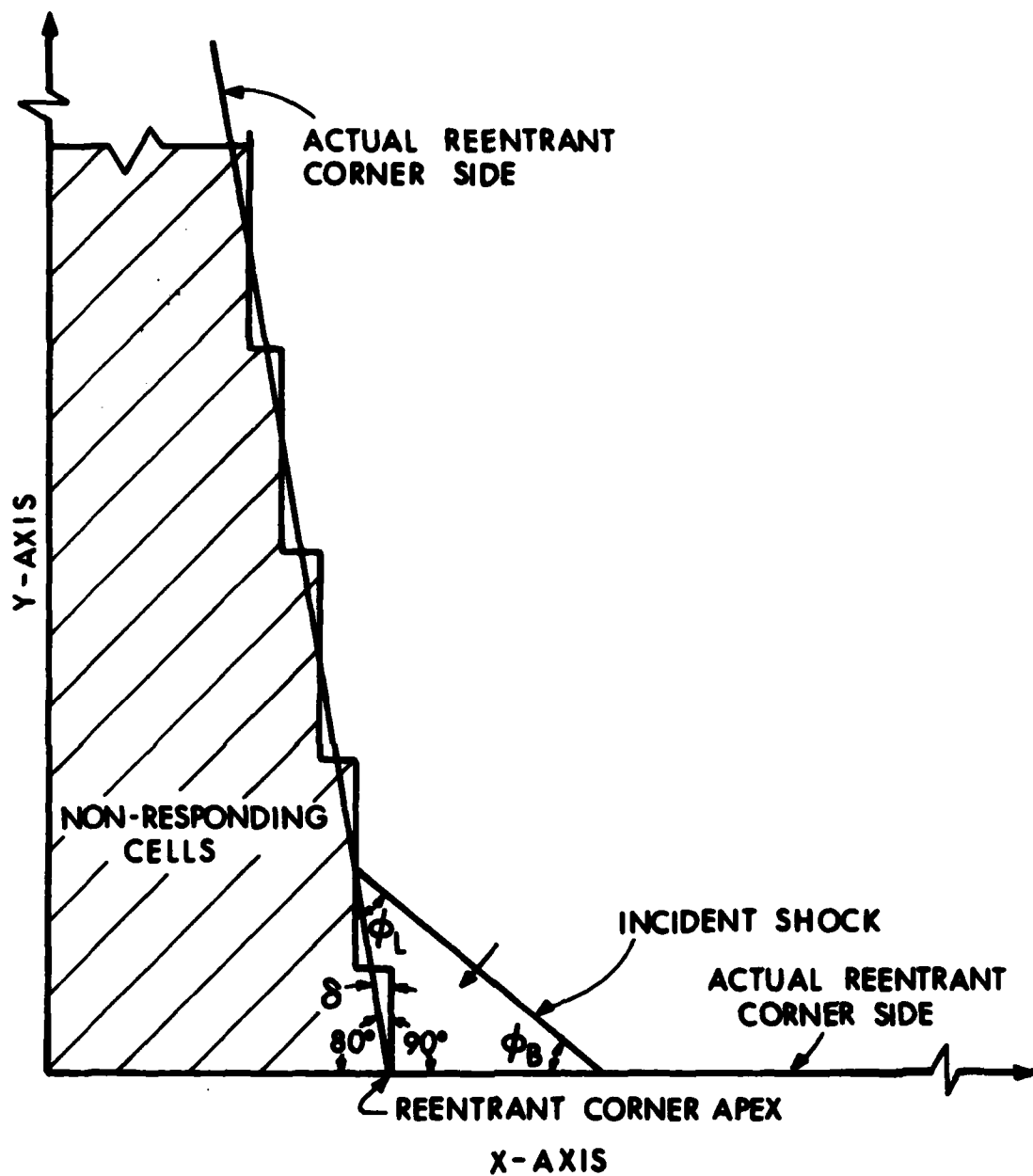


Figure 12. Reentrant Corner Construction.

$$\frac{\Delta Sy}{\Delta Sx} = \frac{\Delta y}{\Delta x} = \frac{1}{\tan 10^\circ} \approx 5.7, \quad (4.3.1)$$

where ΔSy , ΔSx are the dimensions of a step, and Δy and Δx are the dimensions of a cell, in the y and x directions, respectively. A large aspect ratio such as this can cause numerical instabilities in DORF. This stair-step construction can be modified by dividing the single cell into several cells. For the case of $\Delta Sy > \Delta Sx$, the values of ΔSx , ΔSy and Δy are given by:

$$\Delta Sx = \Delta x, \quad (4.3.2)$$

and

$$\Delta Sy = \frac{\Delta Sx}{\tan \delta} \quad (4.3.3)$$

$$\Delta y = \Delta Sy / \left(\left\lceil \frac{1}{\tan \delta} \right\rceil + 1 \right) \quad (4.3.4)$$

where $\lceil \cdot \rceil$ is the greatest integer function. In our case $\delta = 10^\circ$, $\Delta x = 10\text{mm}$, and Δy is calculated via equations (4.3.2)-(4.3.4) as 9.4521 mm. The steps are designed so that each complete step has six cells in the y-direction and one cell in the x-direction. Furthermore, the stair-step wall is constructed so that the line representing the actual, smooth reentrant corner wall bisects both the horizontal and vertical sections of each step. The computational grid contains 60 equal cells in the x-direction and 60 equal cells in the y-direction.

A study comparing the effects of constructing a stair-step wall with more than one square cell per step as opposed to a single high aspect ratio cell per step for shocks propagating parallel to a coordinate axis has been performed at the Air Force Weapons Laboratory⁹. The conclusion reached in that report is that the better way to construct the approximated wall is by using high aspect ratio cells like those that would be generated by equation (4.3.1). This has intuitive appeal, and may be quite valid for codes which can accurately compute with high aspect ratio cells and for cases where the incident angle between the wall and the shock is not near 45° . For a wall angle of 45° , this method reduces to using a single square cell per step. With single cell steps, a normal shock reflection occurs at every cell when the shock reaches the wall, which does not occur on the physically straight wall. For a high aspect ratio cell whose long side is along the direction of travel of the shock, this normal reflection will be weaker than for a square cell. In any case, the numerical simulation may not represent the physical flow because of the many small normal shock/surface interactions.

Figure 13 shows a partial reconstruction of the grids used for two AFWL⁹ problems designated by the numbers 19.8026 (hereafter referred to as Problem A) and 19.8029 (hereafter referred to as Problem B). Problem B uses high aspect ratio cells with $\Delta x = 3$ mm and $\Delta y = 0.529$ mm. A diagonal drawn from the cell lower left corner to the cell upper right corner is at a 10° angle with respect to the lower boundary of the cell. This construction provides a good approximation of the 10° wall angle. Using this construction a 90° expansion occurs at one end of each cell, a normal reflection occurs at the other end, and the computed cell-center values represent some averaging between these two extremes. The absolute atmospheric pressure for this computation is 101.13 kPa and the shock overpressure is 344.6 kPa. The computed peak for Problem B is 423 kPa, which compares very well with the predicted value of 427 kPa taken from Figure 3.786 of Reference 20. Problem A uses steps constructed of square cells, 3 mm on a side, with the steps being one cell high and five cells wide. The arrangement does not approximate a 10° wall but rather approximates an 11.31° wall. If these cells were constructed as prescribed by equations (4.3.2)-(4.3.4), this discrepancy would be rectified. The five flow field cells comprising any given step in Problem A represent a variety of conditions. The forward-most flow field cell along a step, for example cell "A" in Figure 13, is essentially the first cell around a 90° expansion corner after a normal reflection. The last flow field cell on a step, for example cell "B" in Figure 13, is the last flow field cell prior to a non-responding wall against which the shock undergoes a normal reflection. The intervening three flow field cells provide a transition of unknown accuracy between the two extremes. Problem A shows a peak reflected overpressure of 0.758 MPa, 77% above the predicted²⁰ value. However, the flow field cell used in Reference 9 to give the peak pressure value is the same type as cell "B" in Figure 13. This higher pressure is the result of the interaction of the shock with a one-cell-high normal reflecting surface. It would be more informative to see the overpressure histories for all five flow field cells on a step, particularly the third, or middle, cell. The third cell has its center at the geometric center of the step, just as the cell center for the high aspect ratio cell is also the geometric center of the single cell step in Problem B. A comparison between the third cell in Problem A and the high aspect ratio cell in Problem B might be more meaningful.

Another comparison in Reference 9 is between a HULL computation and the corresponding experiment²¹ for a step shock ($P_1/P_0 = 27.3$) impinging on a 40° wall. In that example a Mach reflection develops on the wall.

20. Glasstone, S. and Dolan, P.J., "The Effects of Nuclear Weapons", Department of the Army Pamphlet No. 50-3, Headquarters, Department of the Army (March 1977).
21. Bertrand, B.P., "Measurement of Pressure in Mach Reflection of Strong Shock Waves in a Shock Tube", BRL-MR-2196, US Army Ballistic Research Laboratory, Aberdeen Proving Ground, MD (June 1972). (AD #746613)

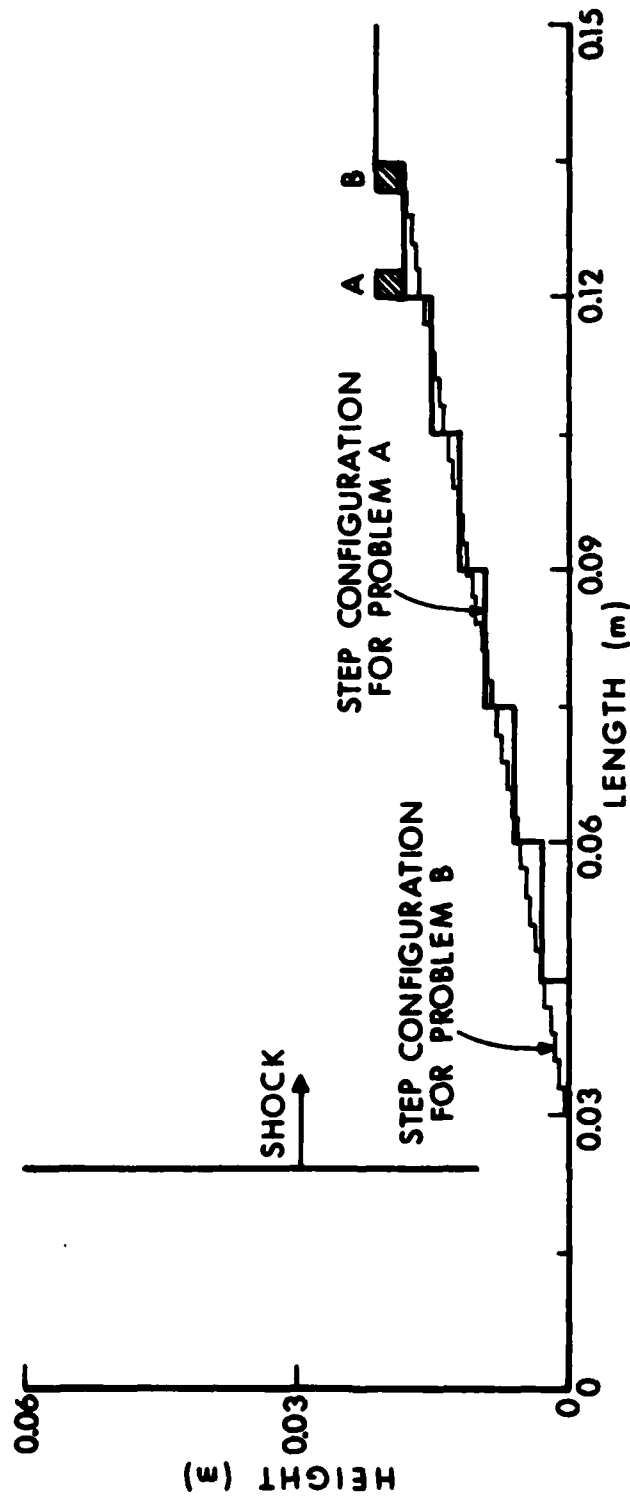


Figure 13. Stair-Step Wall Constructions Used in AWFL-HULL Code Study⁹.

As before, the incident shock is propagating parallel to the horizontal coordinate axis. The grid used for the HULL calculation is constructed of nearly square cells ($\Delta x = 3\text{mm}$, $\Delta y = 2.5173\text{mm}$) in the region of the wall. Each cell on the wall surface constitutes a stair-step. The diagonal of each cell is parallel to the physical wall. As the wall angle approaches 45° both methods studied in the AFWL report became the same. Thus, for this case the procedure recommended by AFWL would be the same as the one used in the DORF simulations. The maximum difference between HULL's results and the experimental peak and late time pressures is 11.5%. However, the structures of the pressure histories do not compare well. The pressure plateaus seen experimentally are not evident in the calculations and the computed times between the initial shock arrival and peak pressure for points well up the wall also do not agree. Thus, the HULL calculation for this problem shows inconsistent simulations of the physical phenomena.

The stair-step formulation used in this report is quite similar to the multiple-square-cell step construction described in the AFWL⁹ report. However, the physical phenomena considered in this report differ from those flows simulated by AFWL because the incident shocks do not impinge normally on the stair-step (see Figure 13) but rather obliquely (see Figure 12), and the incident shock strengths considered in this report are smaller (by 75%-50%) than those in the AFWL study. This report considers both regular and Mach reflections, while the AFWL report is only concerned with MACH reflections. Furthermore, this report deals with the DORF code while the AFWL report documents the HULL code results. Thus the AFWL study is informative, not definitive.

Any type of stair-stepping represents a potentially serious problem. For example, along the bottom boundary of the grid, the incident angle is $\phi_B = 40^\circ$ everywhere, as desired. However, along the left boundary, the incident angle is $\phi_L = 50^\circ$ because of the stair-stepping. Moreover, at every sixth cell along that side there is a local reentrant corner, having $\phi_L = 50^\circ$ and $\phi_B = 40^\circ$. Each of these discrete steps disturbs the flow field.

A better solution to the problem of forming a stair-step wall would be to add the capability of including partial rigid cells in a flow field. Such a capability has been successfully implemented²² in the SAMS code²³ which belongs to the same family of hydrodynamic computer codes as do DORF and HULL. Another alternative is to turn to recently developed techniques for generating body conforming coordinate systems.

22. Coleman, M., ARRADCOM, BRL, Private communication.

23. Traci, R.M., Fan, J.L., and Liu, C.Y., "A Numerical Method for the Simulation of Muzzle Gas Flows With Fixed and Moving Boundaries", BRL Contract Report No. 161, June 1974. (AD #784144)

However, irrespective of the possible alternatives to stair-stepping a straight boundary, a purpose of the present study is to quantify the difference in the flow field in the vicinity of a stepped reflecting boundary as opposed to that near a smooth reflecting boundary.

4.4 Comparison of the Pressure Along the Smooth and Stair-Step Boundaries.

The pressure values for Shots 1 and 2 along both the smooth and stair-step walls are compared in two ways: the spatial pressure profiles are given along the walls at five specific times and then the pressure histories at four selected pairs of wall positions. The pressure values are cell-centered. The cells chosen for the comparison are adjacent to each wall, for example, cells 1,2,3,4,5,... along the smooth wall and cells 1,2',3',4',5',... along the stair-step wall as shown in Figure 14. Therefore, only one stair-step corner is initially downstream of the incident shock. The distance from the vertex of the corner to a given point along either wall is denoted by d . The initial position of the shock is along the straight line between the points (0.158m, 0.0m) and (0.09m, 0.0567m) in the computational domain.

An inconsistency in the reflected pressure values at the first reflection point arises in the DORF simulation due to the stair-step approximation. For example, consider the simulation of Shot 2. Because the actual incident angle of the incident shock along the stair-step is 50° , Mach reflection is predicted at the first reflection point (see Figure 5) rather than regular reflection as on the smooth boundary (incident angle 40°). Even when the same type of reflection is predicted, the pressure behind the reflected shock along the stair-step wall is different from the value along the smooth wall, because the angles of incidence of the shock are different. This inconsistency is inevitable given the constraints of the present DORF capabilities. The discrepancies between the stair-step and smooth boundary pressures caused by this inconsistency may be lessened somewhat, because the conditions imposed in region 2' are identical to those in region 2.

The variations of the absolute pressure values for the numerical simulations of Shots 1 and 2 along the smooth and stair-step walls are compared at the initial time ($t=0$), at a time immediately before the incident shock reaches the vertex, at the time when the maximum pressure develops at the vertex, and at early and late times after the final shock leaves the vertex. The spatial extent of the comparison is 0.18m from the vertex along each boundary. Figures 15-19 show the histories of the computed wall pressures for Shot 2; Figures 20-24 describe those for Shot 1.

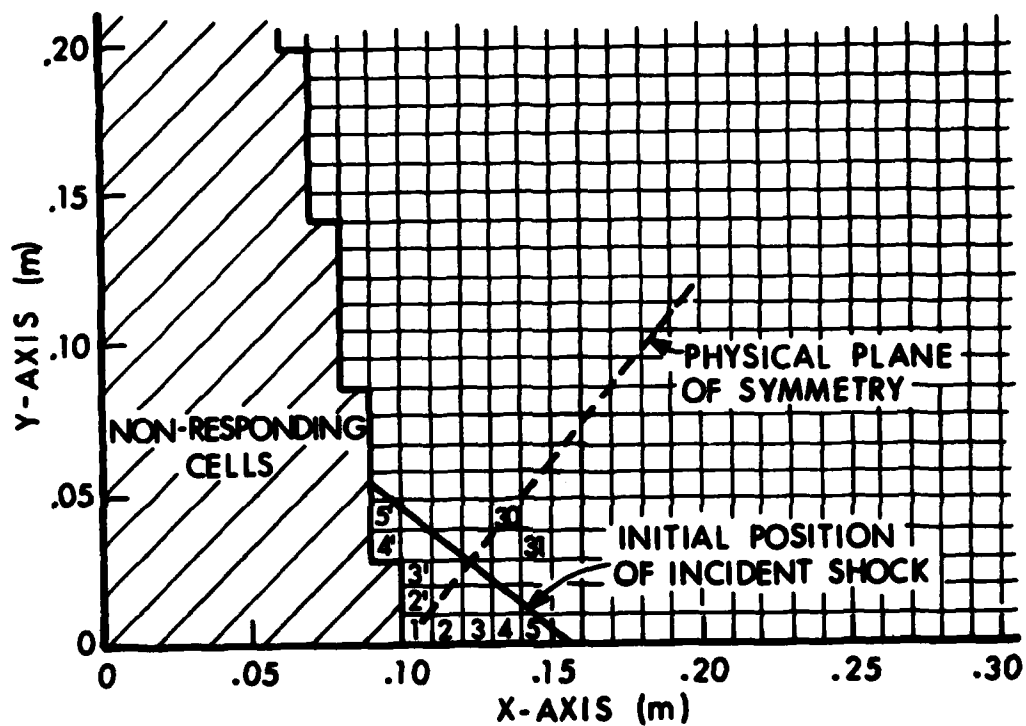


Figure 14. Detailed Portion of Computational Domain Near the Vertex.

Figure 15 compares the initial pressure values along the walls, as prescribed by the initial conditions. The transition from the ambient pressure to the pressure behind the reflected incident shock is smeared out over 3 to 4 cells. These initial curves are not identical, because the uniform mesh spacings along the x-coordinate are not equal to those along the y-coordinate.

At $t = 69.74 \mu s$ (Figure 16), the incident shock has theoretically passed the stair-step corner but has not reached the vertex. However, the calculated pressure has begun to rise due to the shock smearing in cell 1. Along the smooth boundary, the pressure beyond $d = 0.045m$ is within 4% of the theoretical value of 521.08 kPa. For $d > .10m$, the pressure is within 1%. Along the stair-step boundary, three pressure peaks corresponding to the three stair-step corners are present. The first pressure peak at $d = 0.0331m$ is substantially larger than the remaining two. For the first corner, the incident shock propagating into this small "reentrant corner" is reflected, with an accompanying increase in pressure. For the other corners, the initial gas velocities in region 2' are such that the air is partially stagnated in these corners which causes a lesser pressure rise than the shock reflection in the first corner. Although the pressures along the stair-step boundary do oscillate around the corresponding pressures on the smooth boundary, the character of the flow along the stair-step boundary is markedly different from that along the smooth boundary. The amplitude of the oscillations is between 20% and 61% of the smooth boundary values in this example. The last two pressure peaks in Figure 16 do not occur exactly at the corner position because they reached their maxima previously at the corners and are now decreasing and propagating from the corners.

At $t = 114.3 \mu s$ (Figure 17), the pressure at the vertex (in cell 1) reaches a maximum value of 1.643 MPa. The incident shock has reached the vertex and the reflected shock is ready to propagate from the vertex. The pressure curve along the smooth boundary approaches the theoretical far-field value without any oscillations and with only a slight undershoot. Along the stair-step wall the effects of the three corners are apparent. The pressure in the first corner has decreased slightly and has propagated along the neighboring smooth section of the stair-step walls. The areas of increased pressure near the second and third corners have enlarged and the pressure values have decreased from those shown in Figure 16. The pressure values in cells 2' and 3' are greater than those along the corresponding section of the smooth boundary. The percent differences between the pressure values are 49.7% and 25.1%, respectively. The reason for these differences is that regular reflection occurs along the smooth boundary and Mach reflection occurs along the stair-step boundary, due to the different angles of incidence.

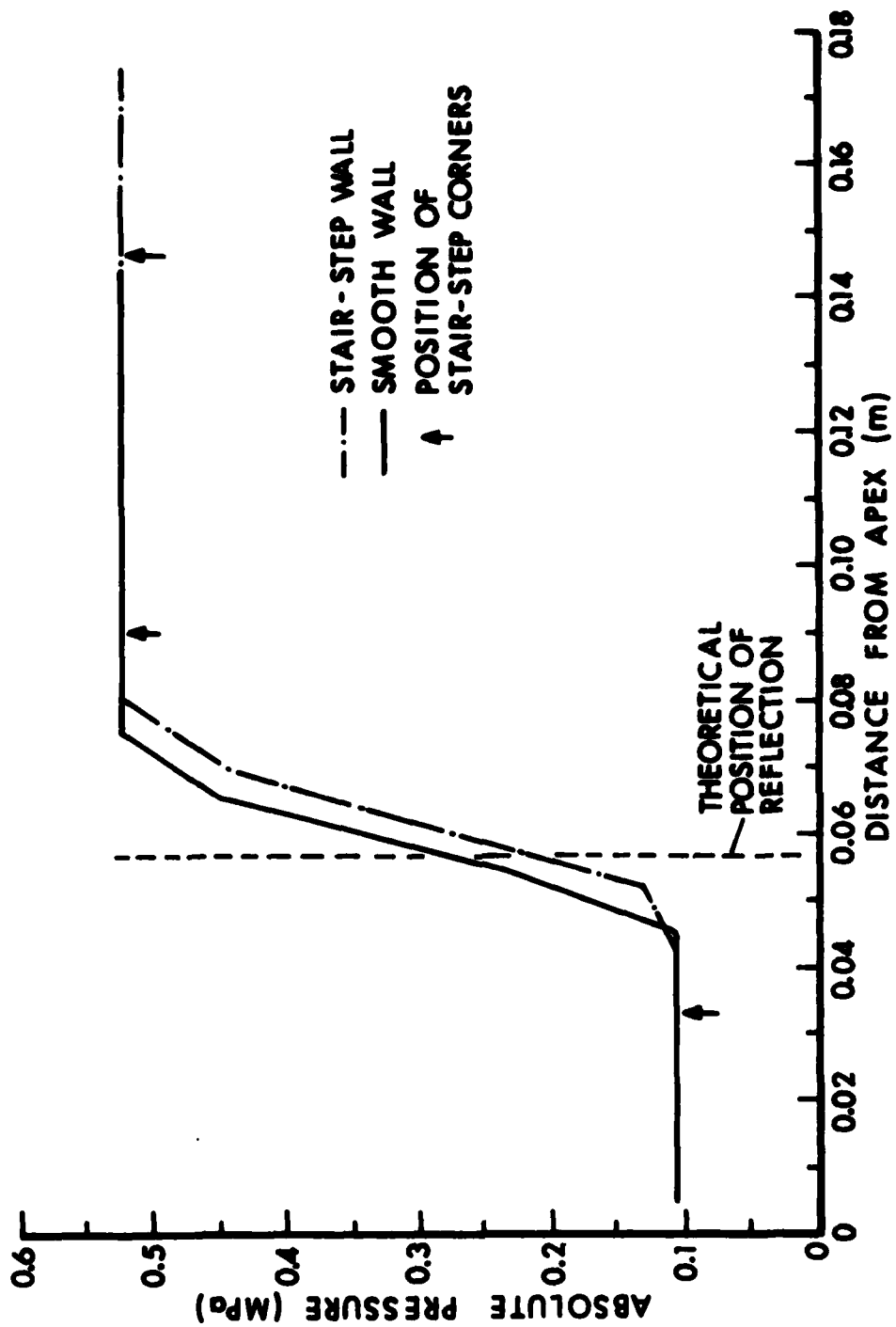


Figure 15. Comparison of Wall Pressure Values for Shot 2 at $t = 0$.

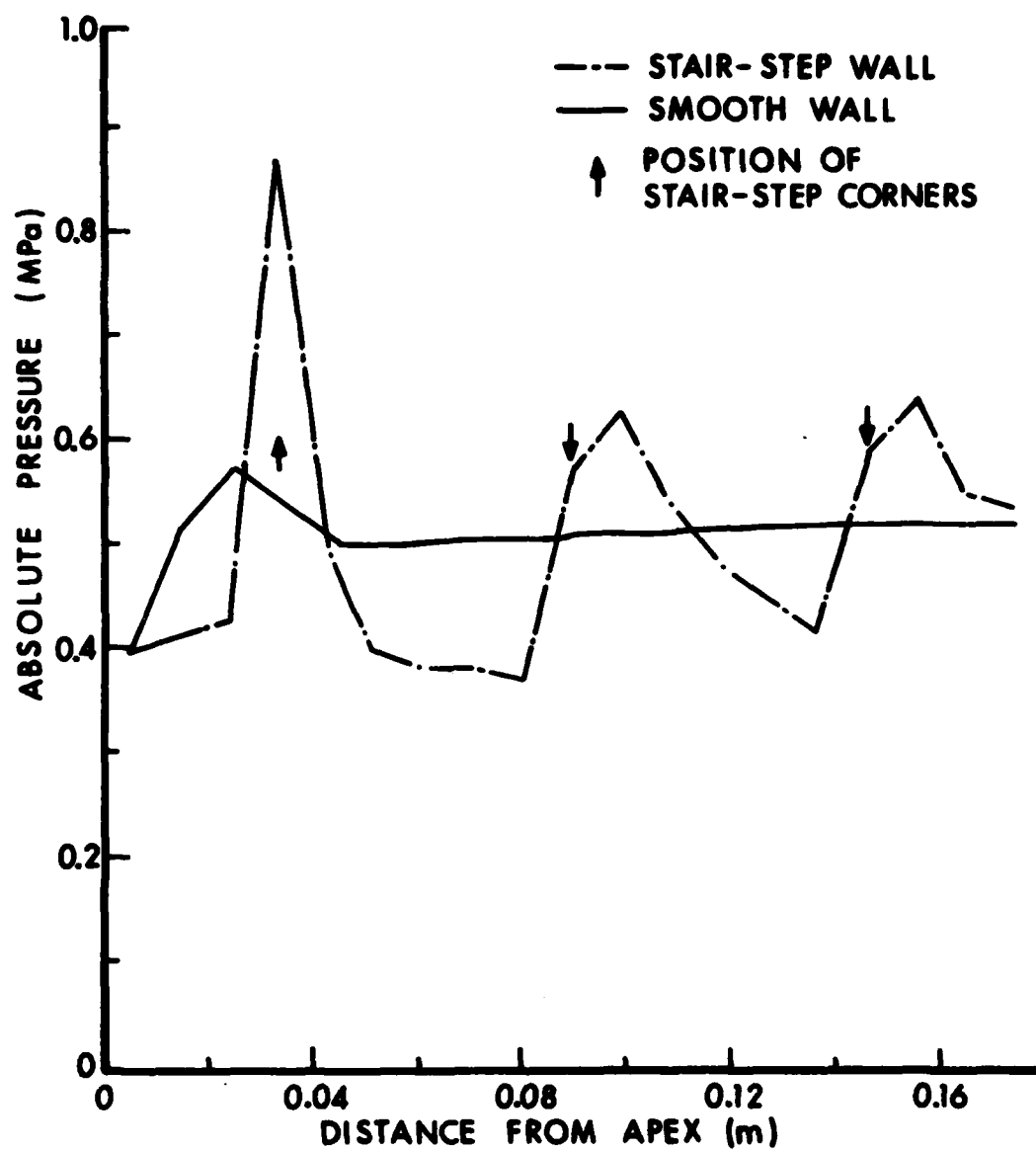


Figure 16. Comparison of Wall Pressure Values for Shot 2 at $t=69.74\mu s$.

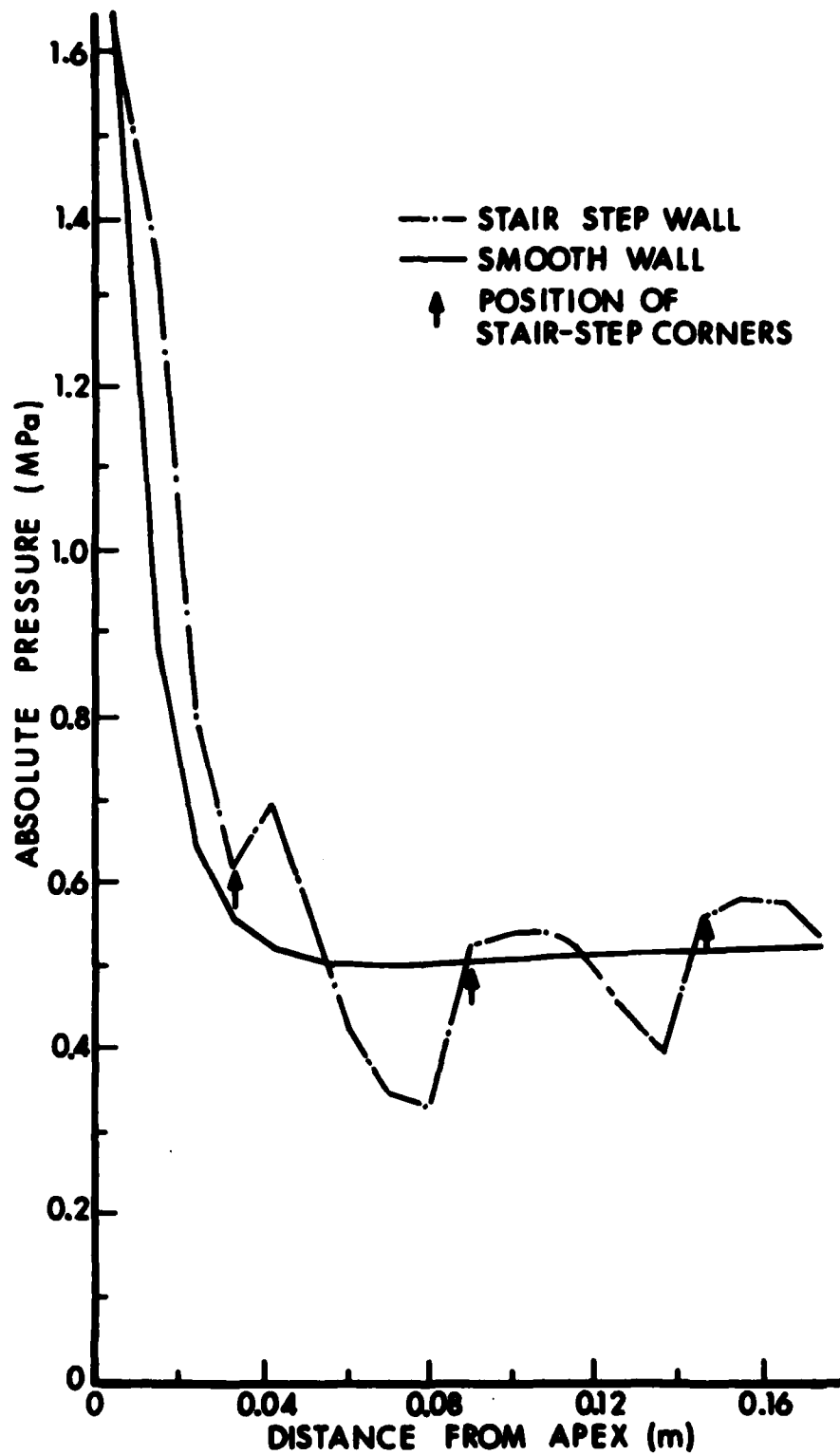


Figure 17. Comparison of Wall Pressure Values for Shot 2 at $t=114.3\mu s$.

Figure 18 gives the pressure profiles after the final reflected shock has left the vertex. At this early time, the magnitudes of the pressures differ by nearly 25% along the wall before the first stair-step corner. The first corner, which is just downstream of the pressure overshoot, changes the slope of pressure decay along the stair-step boundary. The effects of the second and third corners can still be seen. Along the smooth wall the pressure decays without oscillations from its overshoot to the far field pressure value.

Figure 19 shows the pressure profiles at a later time, $t = 321.4 \mu s$. The position of the pressure peak is $0.085m$ from the vertex along the smooth wall and $0.0995m$ along the stair-step wall. The percent difference in locations is 17%. Both pressure profiles are oscillatory behind the peaks. However, the pressure values for $d < 0.45 m$ are within 5% of one another. Near the peaks, the pressure values differ greatly. Ahead of the peaks, the previously described behavior again occurs. Hence, only for "sufficiently" large distances behind the pressure peaks are the pressure values along the smooth and stair-step walls comparable. The beginning of the equilibration of the pressure values in a small region near the vertex is the physical reason for the 5% agreement.

Figures 20-24 show the comparison between the absolute pressure values along the smooth and stair-step walls for the lower pressure Shot 1. This series of figures is analogous to Figures 15-19 for Shot 2. In Figures 20-24, the pressure scale is more refined and thus the percent pressure differences are significantly smaller than those in Figures 15-19. Figure 20 gives the comparison of the initial pressure profiles. The characteristics are identical to those in Figure 15. At $t = 91.09 \mu s$, (Figure 21) the incident shock is between the vertex and the first stair-step corner. The pressure in the vertex cell has begun to rise due to shock smearing. Behind the incident shock overshoot ($d > .055m$), the calculated pressures along the smooth boundary are within 2.4% of the theoretical value. Along the stair-step boundary, a pressure peak occurs near each of the three corners. The same phenomena which are discussed in relation to Figure 16 are present again. The corner effects are not so severe, because the initial flow field is weaker. The calculated pressure values along the stair-step boundary are different by at most 5.3% from the calculated smooth boundary values. These results are significantly better than those depicted in Figure 16. The pressure profiles at $t = 142.4 \mu s$ (Figure 22) show that the incident shock has reached the vertex. The numerically caused pressure rise along the smooth boundary at $0.065 m$ deviates by less than 2% from the theoretical value. The effects of the three corners along the stair-step wall are apparent. The pressure peak at the first corner has decreased from that in Figure 21, and those at the second and third corners have expanded along the smooth sections of the stair-step walls. The maximum deviation of the stair-step wall profile from the smooth wall profile is 9.2% and occurs at the first corner. The differences between the pressure profiles at the second and third cell centers are 1.2% and 2.3% respectively. This significant improvement over the calculation for Shot 2

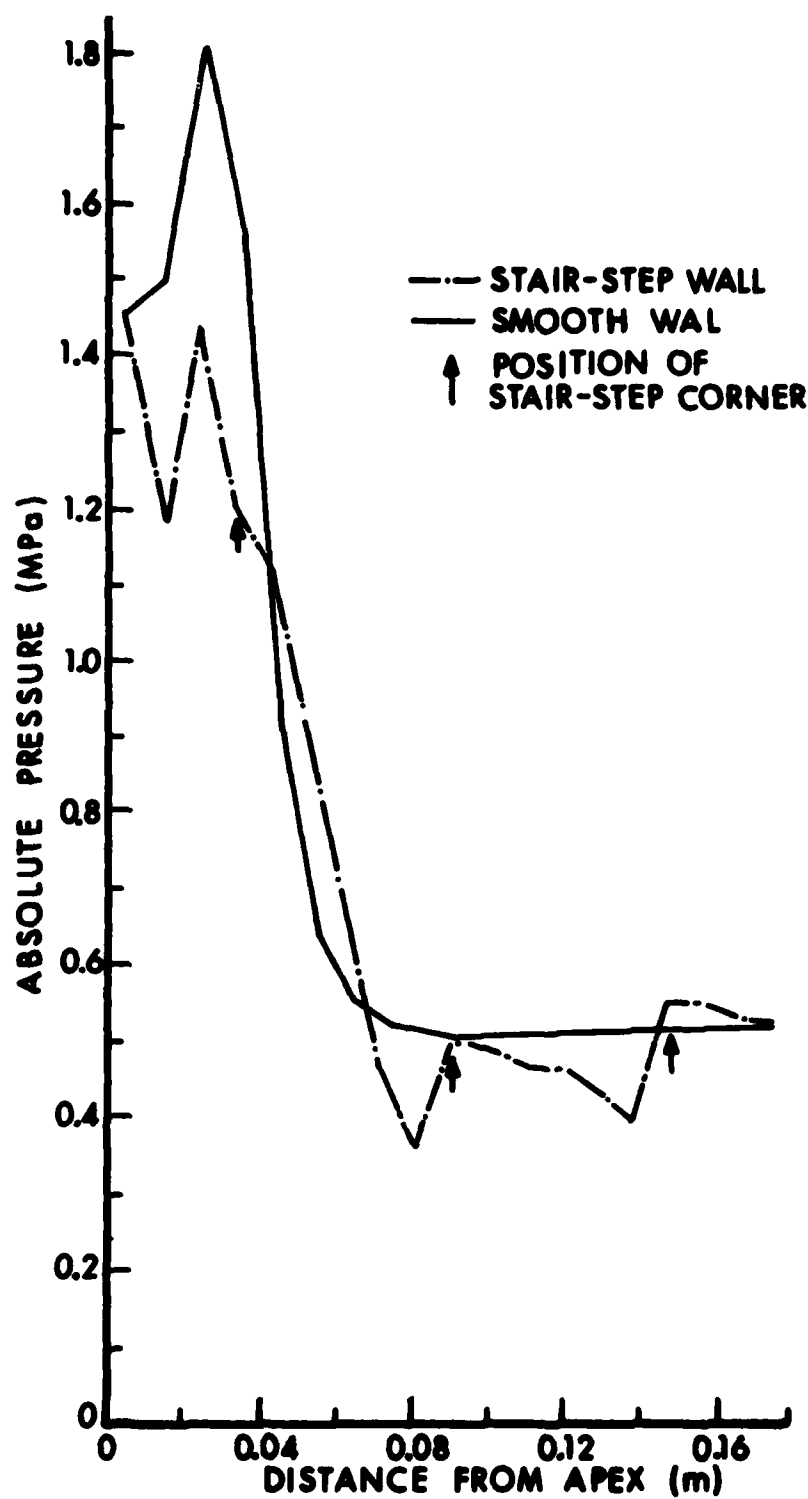


Figure 18. Comparison of Wall Pressure Values for Shot 2 at 183.6 μ s.

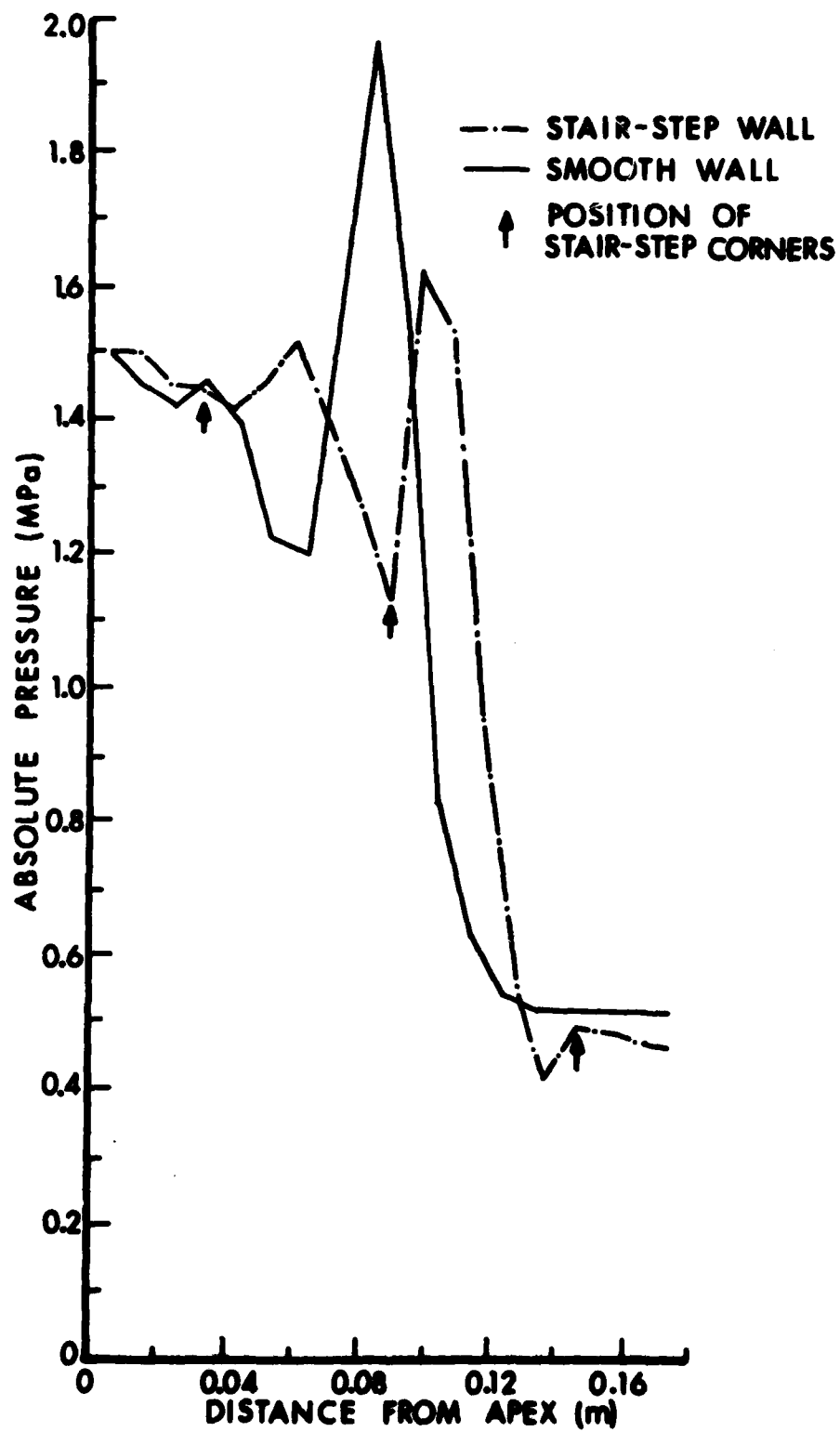


Figure 19. Comparison of Wall Pressure Values for Shot 2 at $t=321.4\mu s$.

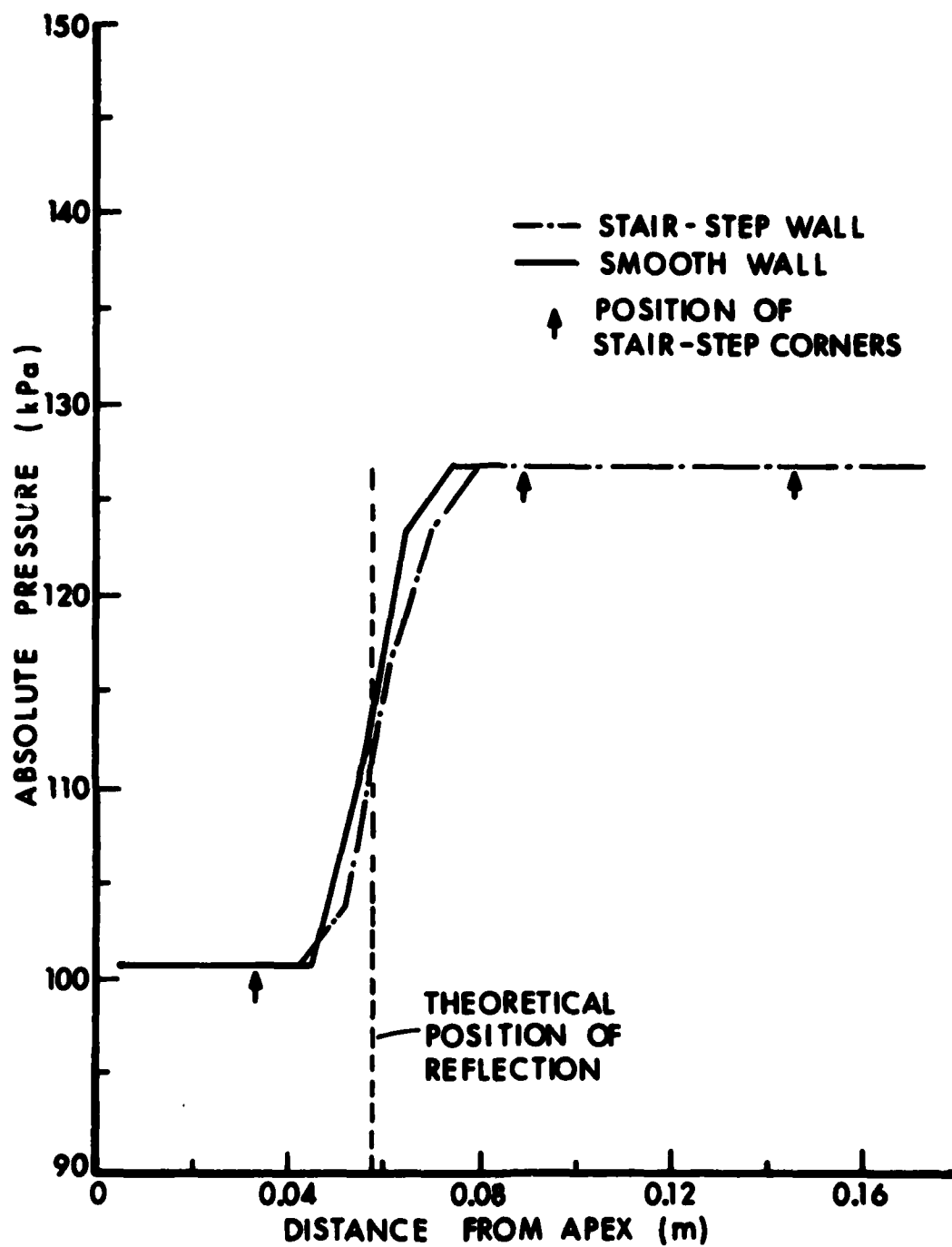


Figure 20. Comparison of Wall Pressure Values for Shot 1 at $t = 0$.

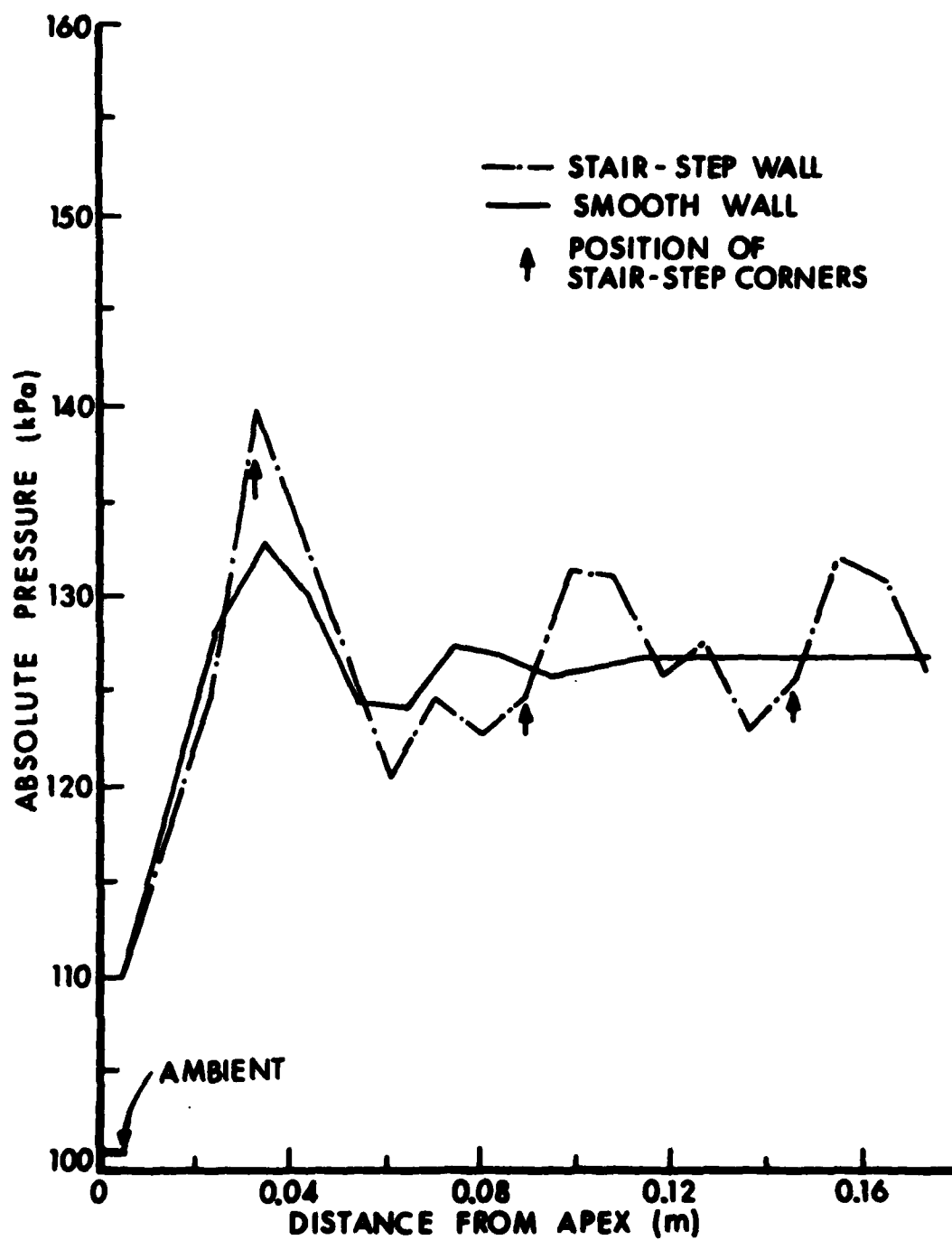


Figure 21. Comparison of Wall Pressure Values for Shot 1 at $t=91.09\mu s$.

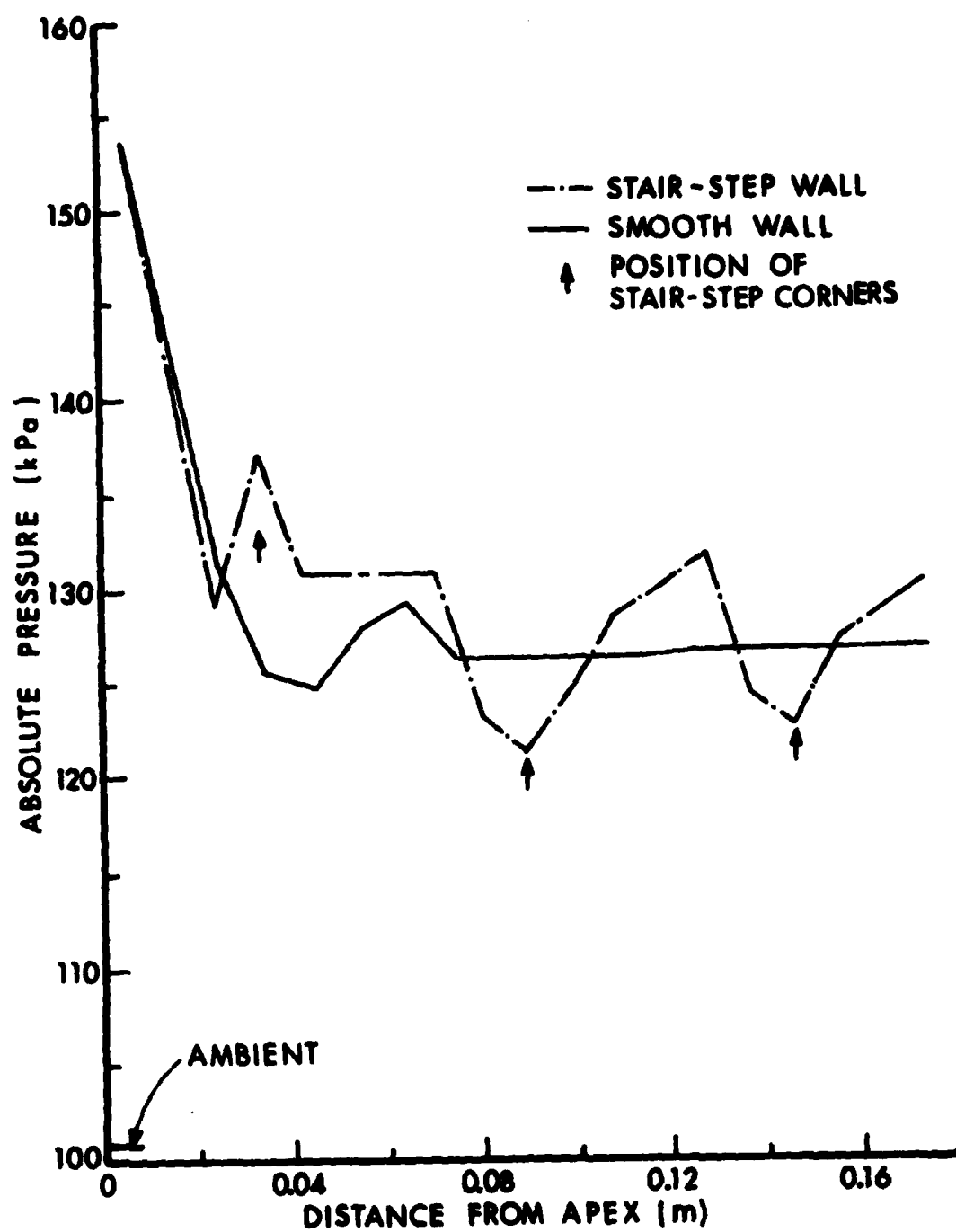


Figure 22. Comparison of Wall Pressure Values for Shot 1 at $t=142.4\mu s$.

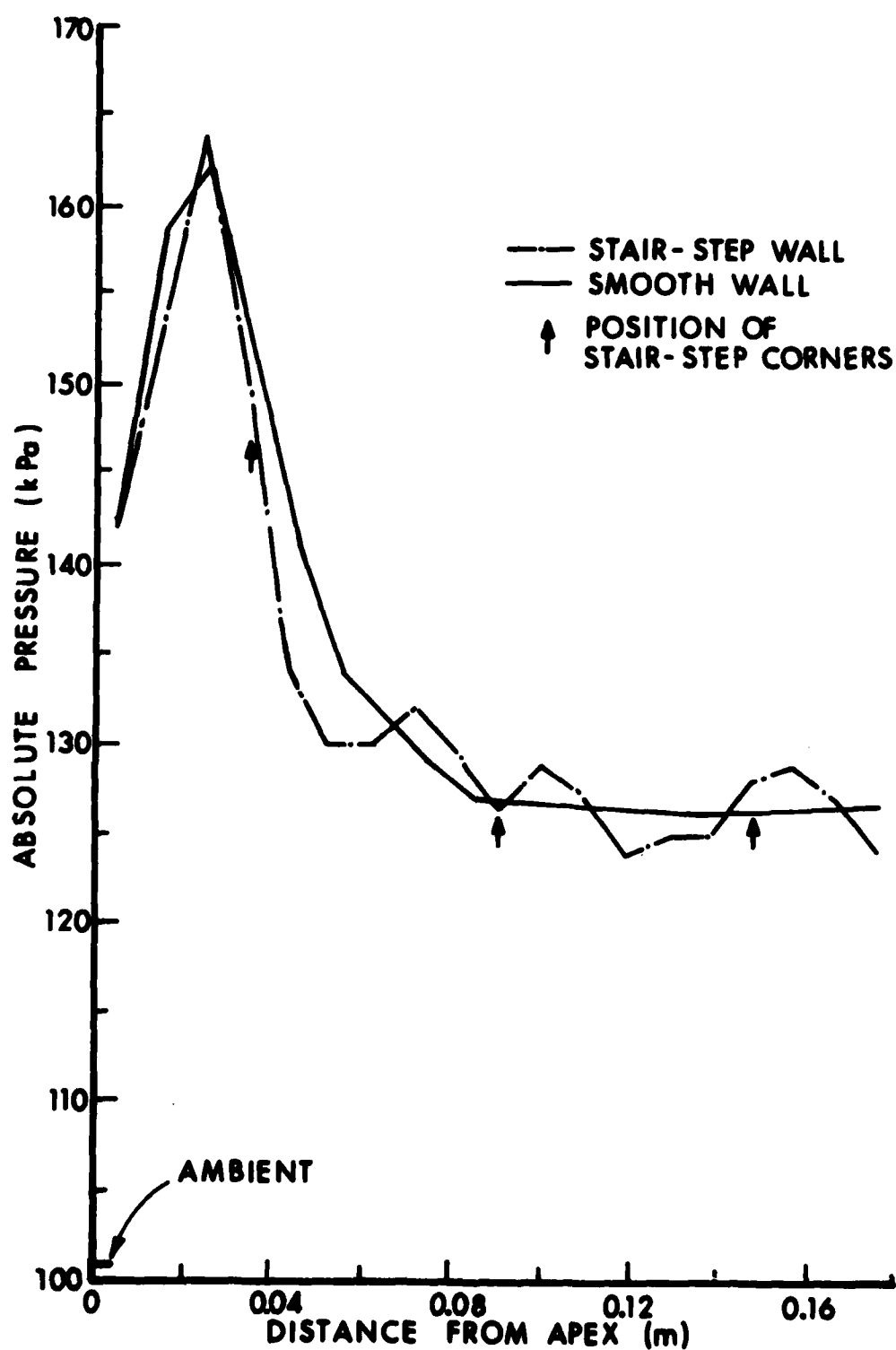


Figure 23. Comparison of Wall Pressure Values for Shot 1 at $t=240.7\mu s$.

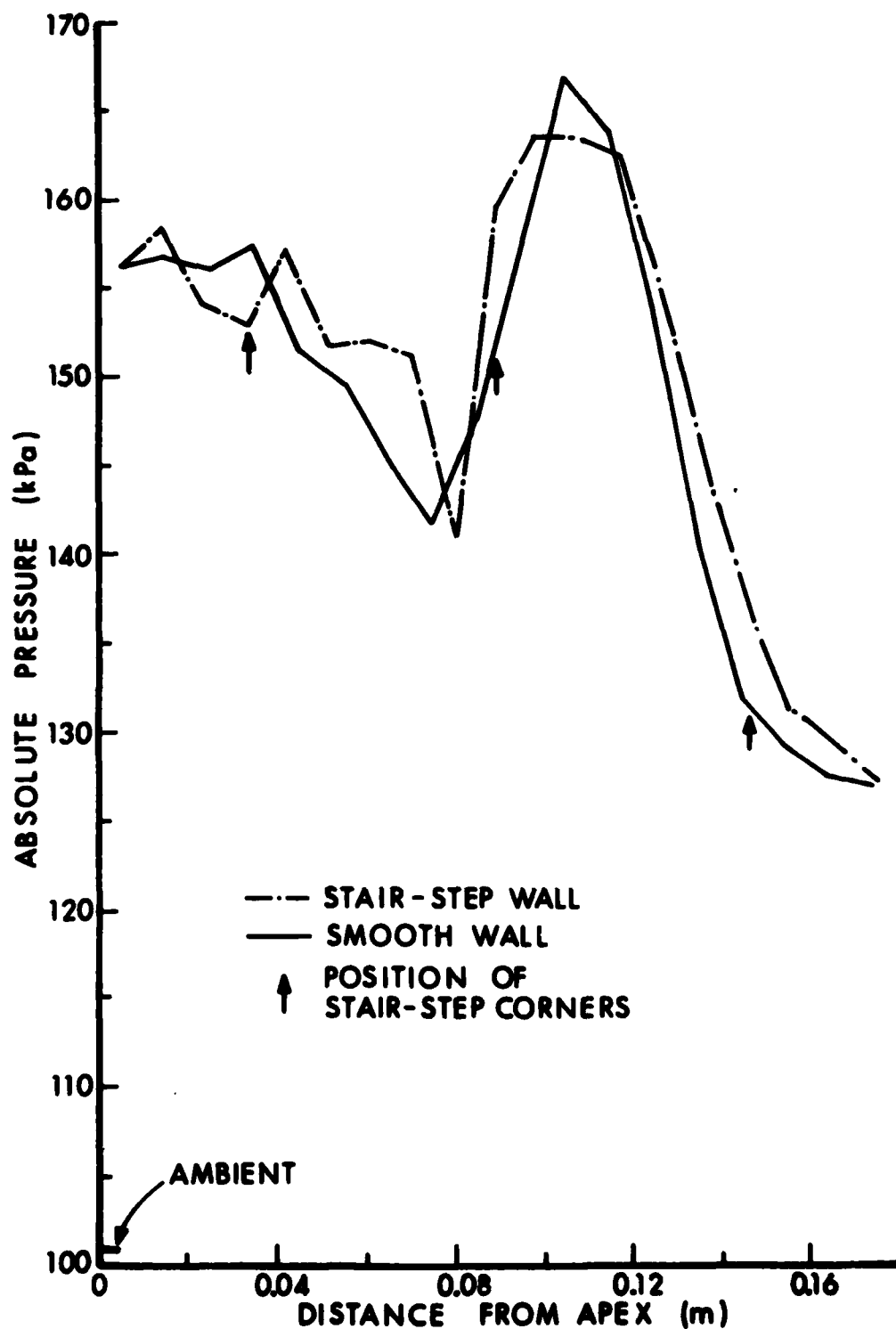


Figure 24. Comparison of Wall Pressure Values for Shot 1 at $t=465.6\mu s$.

is attributed to the fact that regular reflections occur on both walls and the incident shock is a very weak shock. Figure 23 shows that the pressure peaks have moved away from the vertex at $t = 240.7\mu s$. The positions of the largest peaks are very close and their magnitudes differ by approximately 1%. The maximum difference between the pressure profiles is less than 6%. As in Figure 18, the smooth wall profile ahead of the maximum pressure is smooth while the stair-step profile contains oscillations. In Figure 24 the pressure peaks along both walls occur approximately at 0.105m from the vertex. The profiles oscillate behind their pressure peaks and differ from each other by at most 6% from the vertex to their peak. Thus, the pressures for Shot 1 equilibrate faster behind the final reflected shock than for Shot 2.

Figures 25-32 compare the pressure histories at corresponding positions [(2,2'), (3,3'), (4,4') and (5,5')] in Figure 14. Because the mesh increment in the x-direction (10 mm) is not equal to the increment in the y-direction (9.4521mm) the cell-centers at which the pressures are recorded are not equidistant from the vertex. The distances from the vertex to the cell-centers are: 15mm for cell 2 and 14.18 mm for cell 2', 25 mm for cell 3 and 23.63 mm for cell 3', 35mm for cell 4 and 33.08 mm for cell 4', and 45 mm for cell 5 and 42.53 mm for cell 5'. Consequently, the pressure comparisons show small phase differences. In particular, the initial pressure rise along the smooth wall precedes that along the stair-step wall because the position of the station along the smooth wall is closer to the initial position of the incident shock than the corresponding cell-centered positions along the stair-step wall. Furthermore, the final reflected shock returns to the stair-step wall cell position before it reaches the corresponding smooth wall cell position. Consequently, the crossover of the solid and dashed curves during the final pressure rise in Figures 25-32 is as expected. The duration of the initial pressure plateau decreases with successive comparisons of cells 2 and 2', 3 and 3', 4 and 4', and 5 and 5' because the time for the incident shock to reach the appropriate cell-center decreases with increasing cell number.

Figures 25-28 compare the pressure-time histories for Shot 2. The "plateaus" of the solid pressure curves immediately after the first increase, which can be seen in Figures 26-28, are due to the difference in time between the arrival of the incident shock at a given position and the return of the final reflected shock to that position. As expected, the duration of the pressure plateau increases as the distance from the vertex to the cell increases. These plateaus are missing in the dashed curves, because the stair-step corner prevents analogous behavior. The deviations of the pressure values in the flow field away from a stair-step corner can be significant when compared with a corresponding position off a smooth wall. In Figure 25, the position of cells 2 and 2' are within 5.5% of each other, and yet the maximum difference in their pressure values before peak pressure occurs is 82% at $t = 0.122$ ms. The pressure history at the stair-step reentrant corner

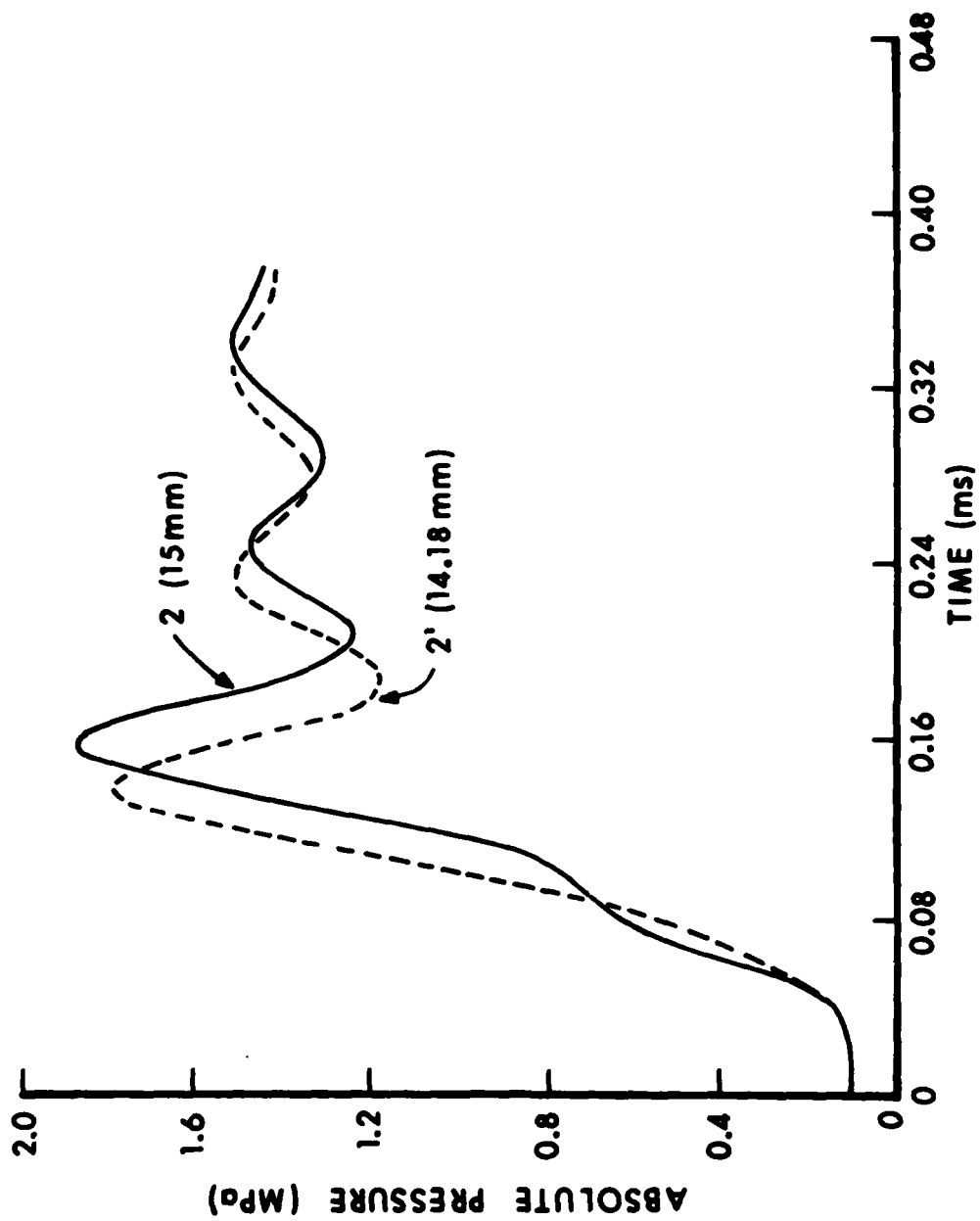


Figure 25. Comparison of Wall Pressure Histories at a One and a Half Cell Distance From the Vertex for Shot 2.

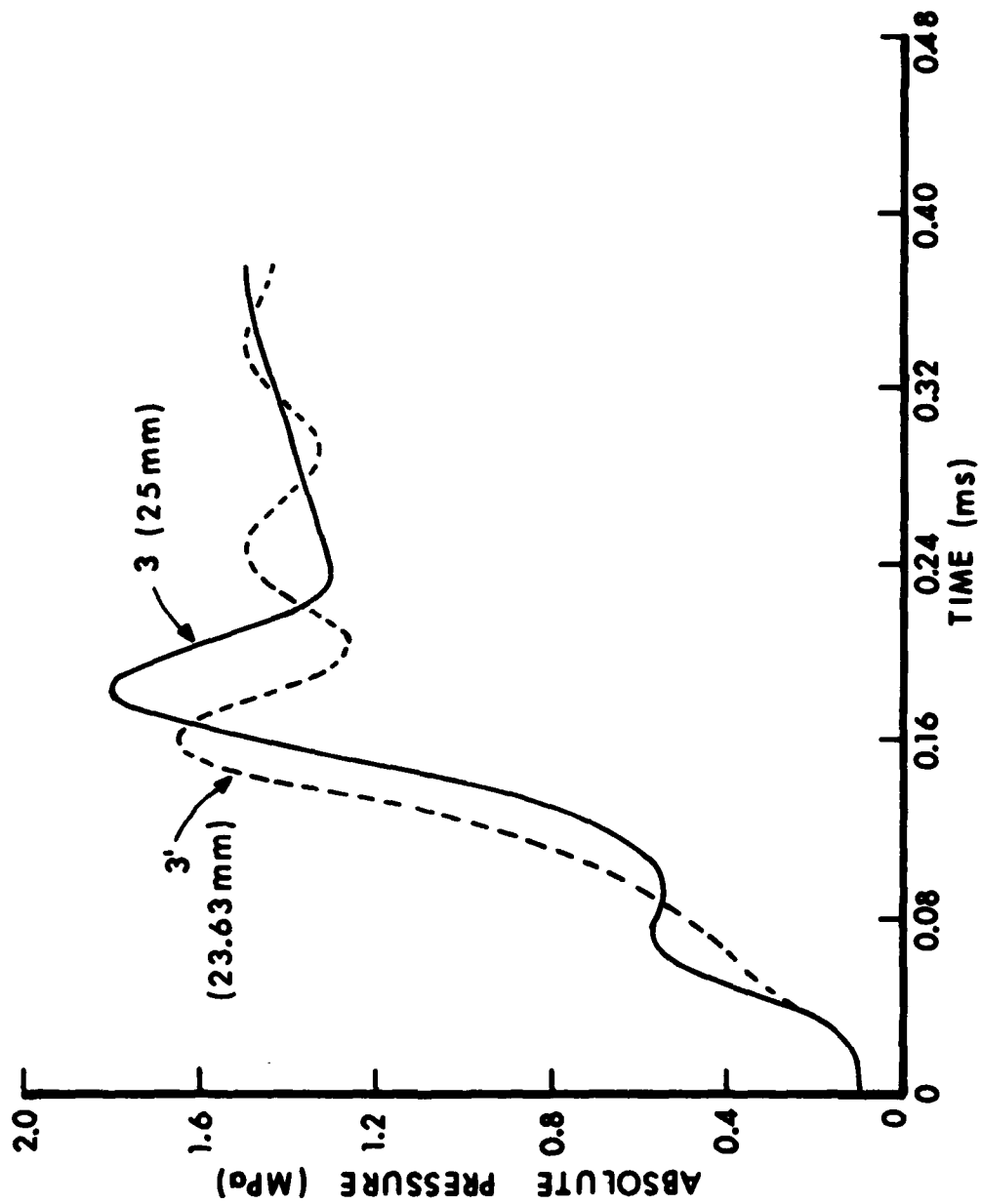


Figure 26. Comparison of Wall Pressure Histories at a Two and a Half Cell Distance From the Vertex for Shot 2.

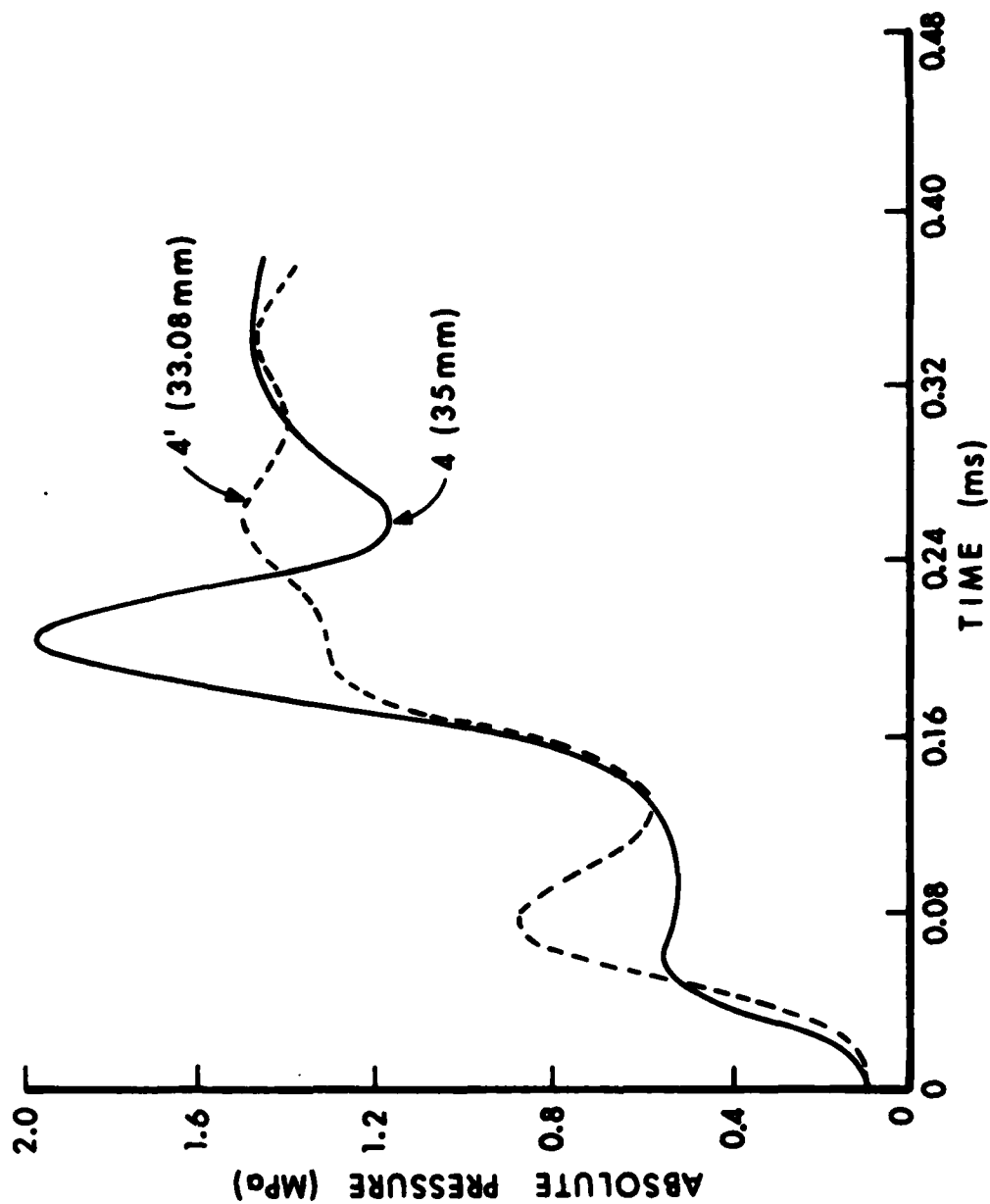


Figure 27. Comparison of Wall Pressure Histories at a Three and a Half Cell Distance From the Vertex for Shot 2.

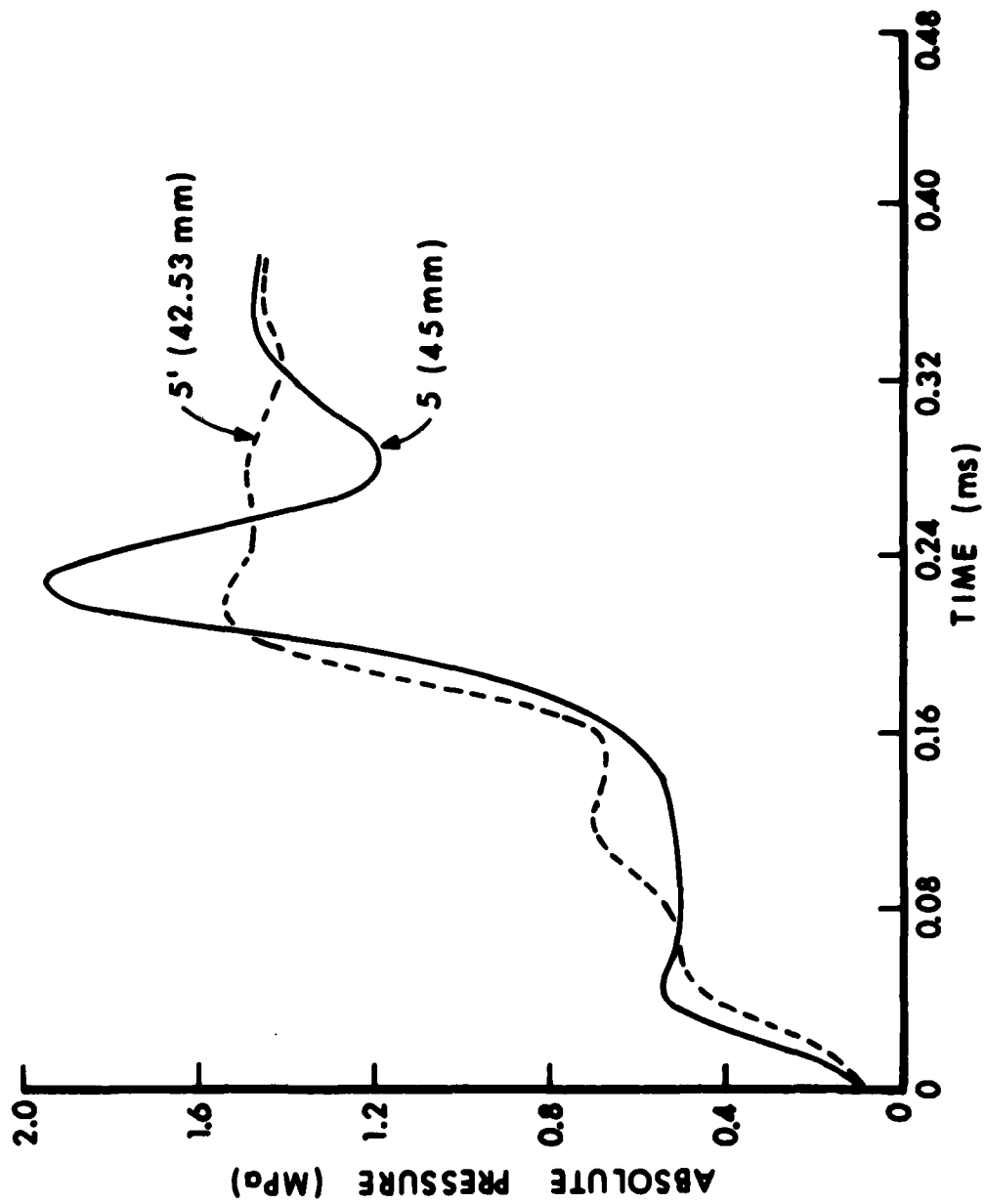


Figure 28. Comparison of Wall Pressure Histories at a Four and a Half Cell Distance From the Vertex for Shot 2.

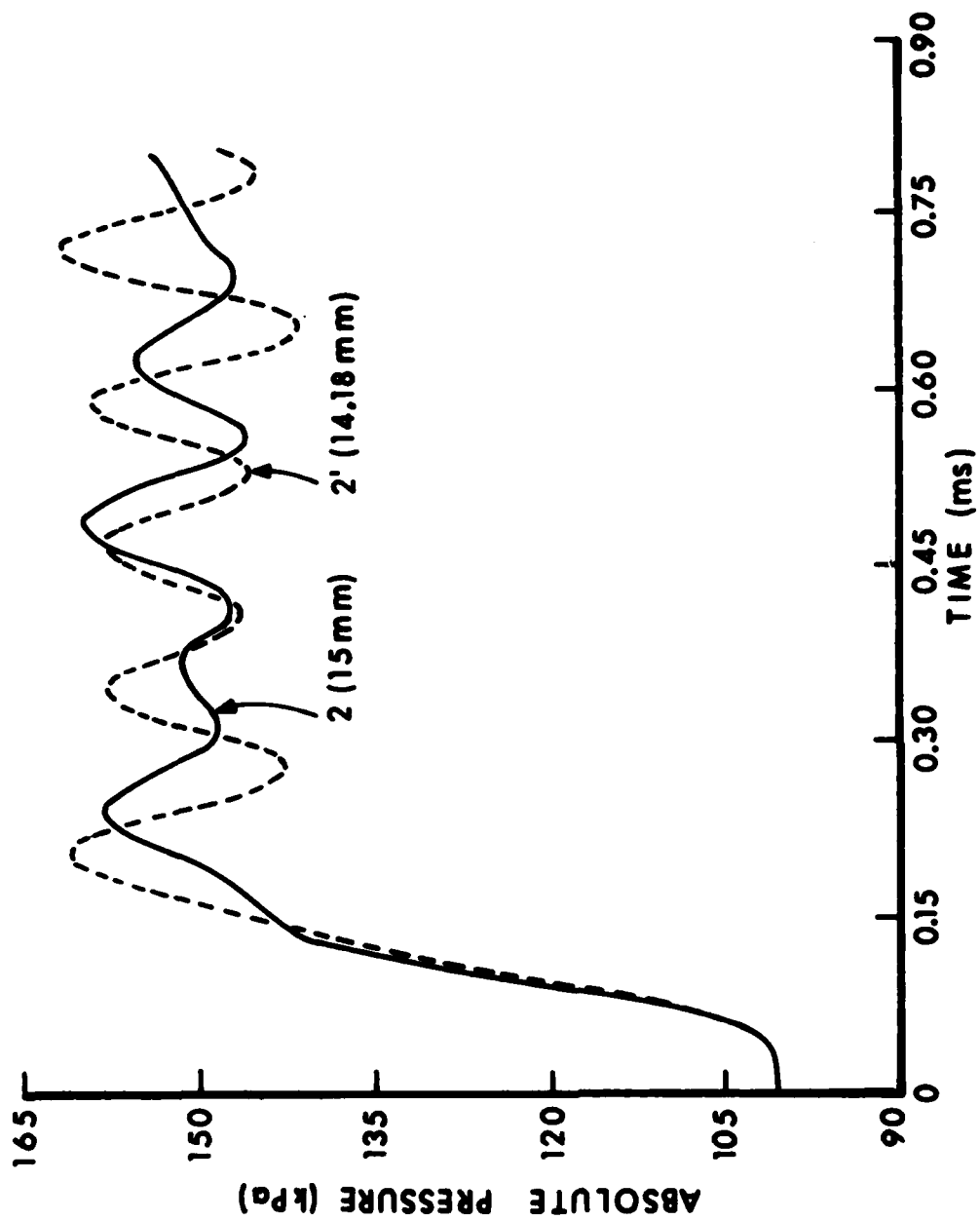


Figure 29. Comparison of Wall Pressure Histories at a One and a Half Cell Distance From the Vertex for Shot 1.

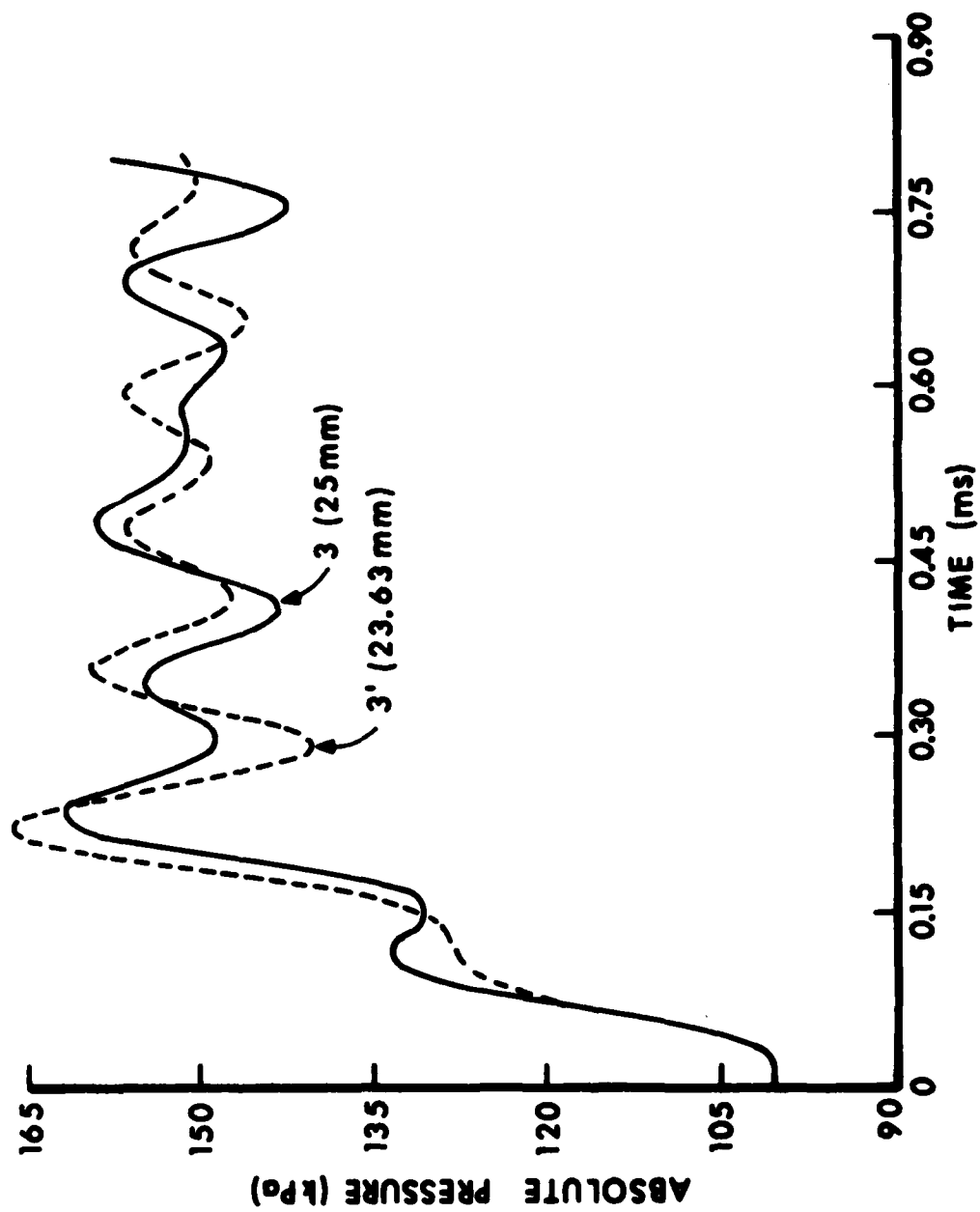


Figure 30. Comparison of Wall Pressure Histories at Two and a Half Cell Distance From the Vertex for Shot 1.

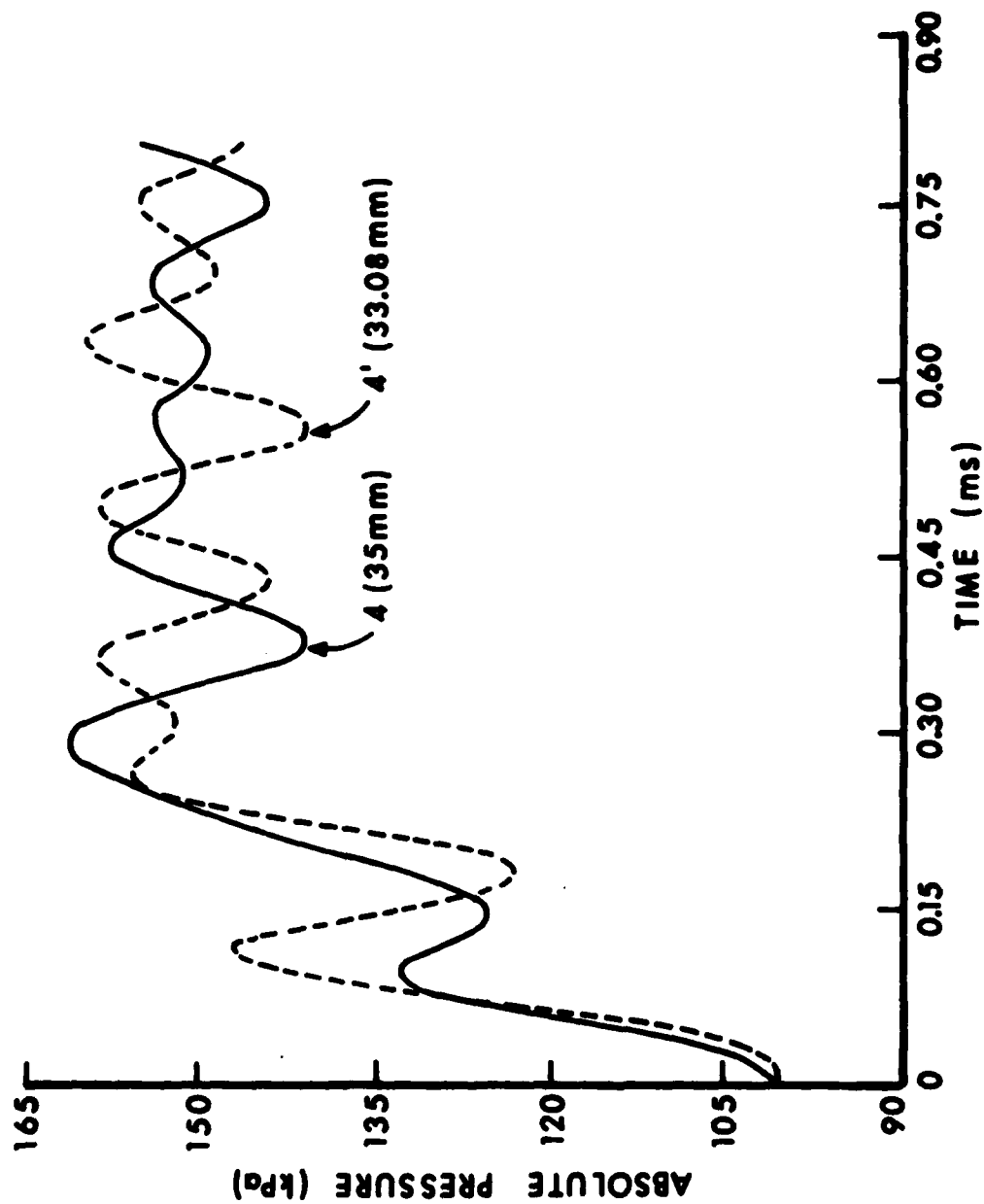


Figure 31. Comparison of Wall Pressure Histories at Three and a Half Cell Distance From the Vertex for Shot 1.

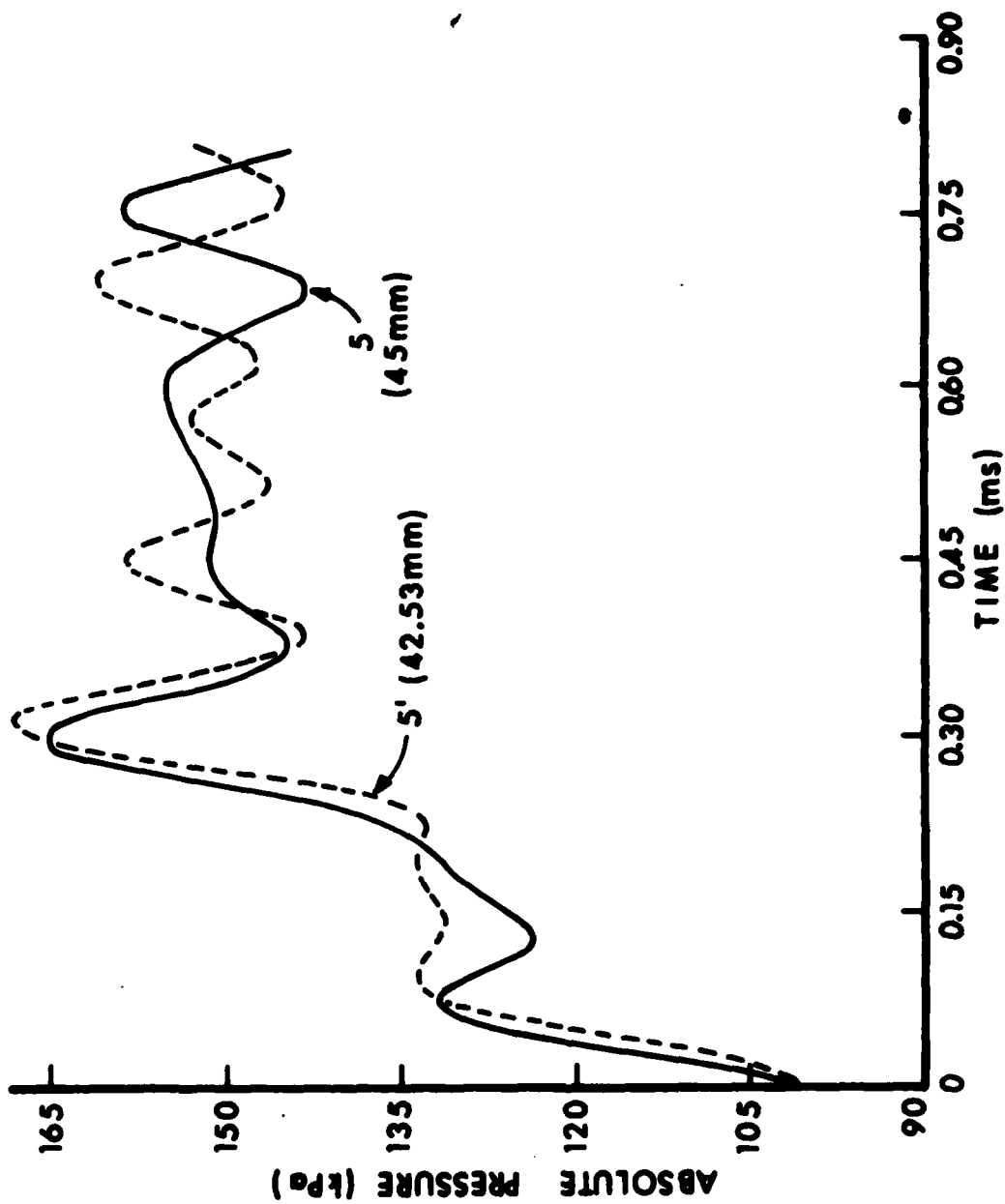


Figure 32. Comparison of Wall Pressure Histories at Four and a Half Cell Distance From the Vertex for Shot 1.

(cell 4') is given as the dashed curve in Figure 27. The interaction between the incident shock and this small reentrant corner results in the pressure rise at $t = 0.08$ ms. A 71% difference between the dashed and solid curves exists at this time. In Figure 28, the first pressure rise of the dashed curve is due to the incident shock, the second increase is due to the propagation of the high pressure seen at cell 4' (Figure 27) along the smooth section of the stair-step wall to cell 5', and the final rise is due to the arrival of the final reflected shock propagating from the vertex. In all the Figures 25-28, the smaller magnitudes of the final pressure jumps and the steadier rise along the stair-step boundaries may account for the smaller pressure overshoots in the stair-step wall pressure curves than in those along the smooth wall. The differences between the final pressure values along the smooth and stair-step walls decrease as a function of time due to the equilibration of the pressures in the vertex region. This phenomenon is quite apparent in Figure 25.

Figures 29-32 compare the pressure-time histories at corresponding positions along the smooth and stair-step walls for Shot 1. Figures 29-32 are analogous to Figures 25-28 and similar comments are applicable. The percentage differences are significantly smaller and the pressure scales are more refined for this numerical simulation than for Shot 2. In both Figures 29 and 30 the maximum deviation in the pressure values before peak pressure occurs is less than 7%. The marked increase in the pressure values of the dashed curve at approximately $t = .12$ ms in Figure 31 is due to the corner at cell 4'. The maximum pressure deviation near this time is 14%. The numerically caused undershoot of the solid curve in Figure 32 at $t = 0.13$ ms is absent in the dashed curve because a compression wave caused by the high pressure region at cell 4' has traveled along the smooth section of the stair-step wall to station 5'.

5. COMPARISON OF PRESSURE VALUES FROM EXPERIMENTS, ANALYSES, AND NUMERICAL SIMULATIONS

5.1. Experimental, Analytical and Numerical Peak Pressure Values at the Vertex.

The experimental pressure values at the vertex are compared with the analytical and numerical results in Figures 33 and 34. In the experiment, a rarefaction wave originates at the leading edge of the wedge, propagates along the wall's surface and ultimately lowers the pressure at the vertex. This expansion wave is absent in the analytic model and the DORF simulation because of their infinite wedge assumption. Consequently, the experimental peak pressure value is compared with the final pressure values from the analytical model and for corner cell 1 in the DORF simulation (see Figure 14). In the DORF results pressure oscillations are produced by the numerical simulation of the shock waves. A single comparable pressure value was obtained from the pressure history in cell 1 by a least squares fit to a constant.

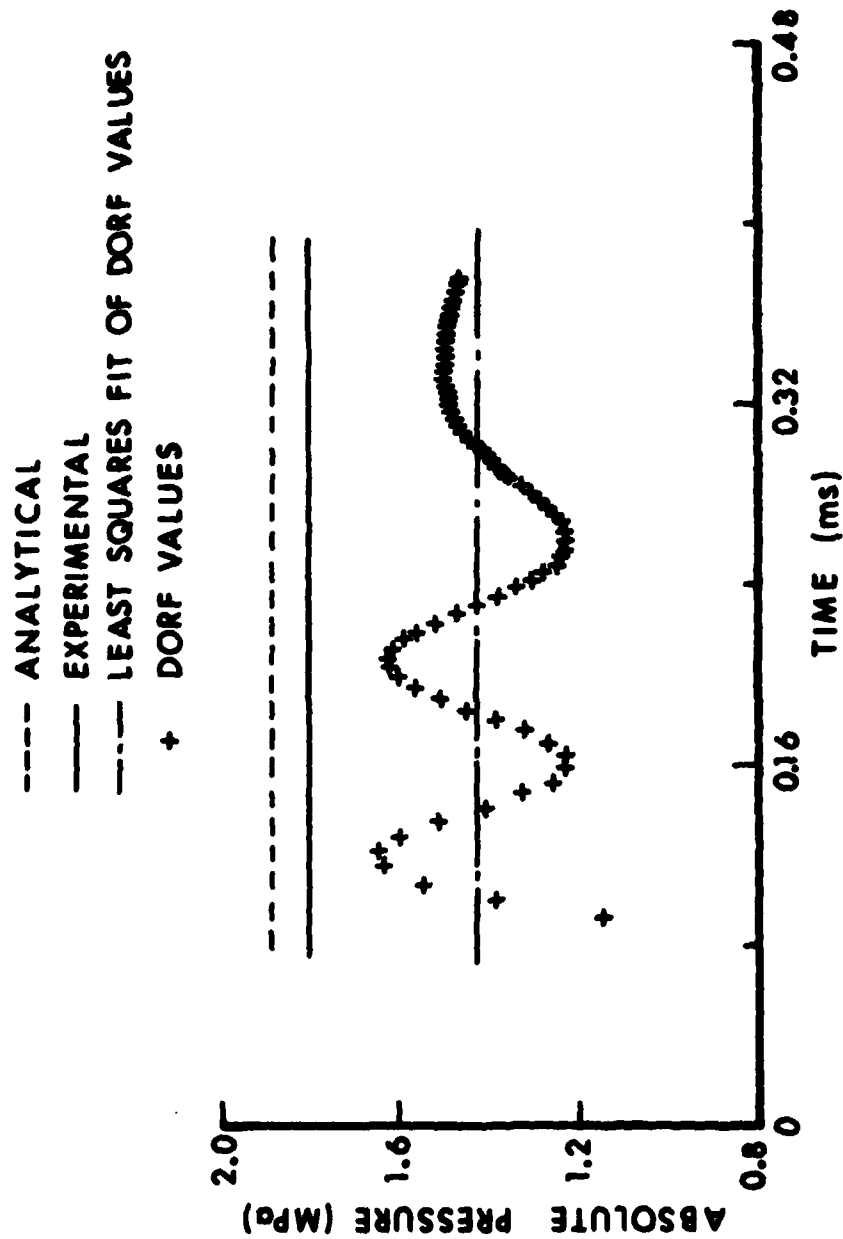


Figure 33. Comparison of Experimental, Analytical and Numerical Values of the Peak Vertex Pressure for Shot 2.

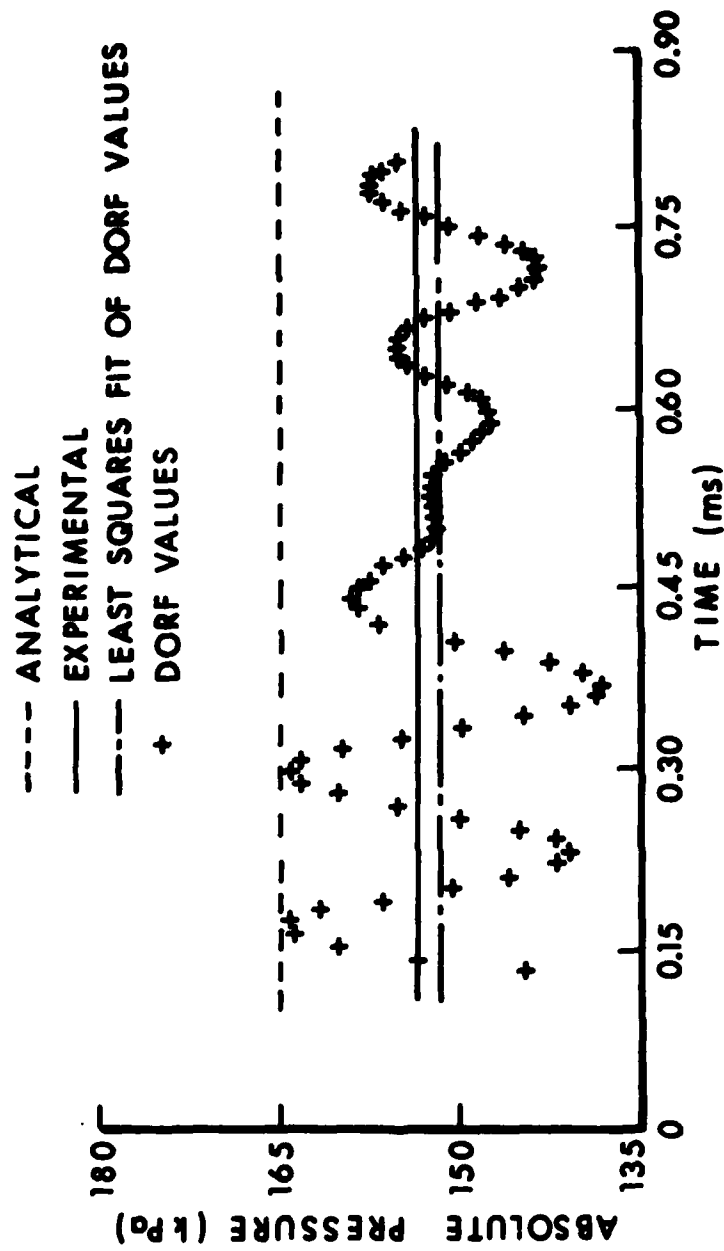


Figure 34. Comparison of Experimental, Analytical and Numerical Values of the Peak Vertex Pressure for Shot 1.

For Shot 2 (Figure 33), the peak experimental value is 1.8195 ± 0.0859 MPa, the analytic value is 1.8913 MPa, and the least squares value from the DORF results is 1.4406 MPa. The analytically computed pressure is 3.95% larger than the experimental value and is within the experimental error. The DORF value differs by -20.82% from the experimental value and by -23.83% from the analytical value. The pressure value from the analytic model should be the largest, because the assumption of an inviscid gas does not allow any viscous effects. Viscous forces which dissipate the pressure are present in the experiment. Although the DORF simulation assumed an inviscid gas, the numerical method in DORF introduces diffusion which is effectively an implicit artificial viscosity. In the determination of the type of reflection which occurs at the first reflection point for Shot 2, the quantities $\phi_0 = 40^\circ$ and $P_0/P_1 = 0.4168$ generated a point just below the curve ϕ_c in Figure 5. The close comparison of the analytic and experimental values indicates that the past history of the flow did not affect the reflection process.

The comparison of the experimental value with both the analytical and the DORF results for Shot 1 is given in Figure 34. The experimental pressure peak value at the apex is 154.58 ± 2.69 kPa. The analytical pressure value is 165.44 kPa. The least squares straight line fit of the DORF pressure values is 151.97 kPa. Consequently, the analytic pressure value is 7.03% larger than the experimental value, and the DORF value is 1.69% smaller. The DORF value is 8.14% smaller than the analytic value. The relative position of the three values is the same as in Figure 33. However, contrary to the results for Shot 2, the DORF results for Shot 1 provide better approximations to the experimental values than do the analytical values.

5.2. Experimental and Analytical Peak Pressure Duration Values.

A comparison of the experimental measurements with the analytic approximations to the peak pressure duration for a finite length re-entrant corner can be made when we combine the peak pressure duration results from Sections 2 and 3.3 into Table 6.

Table 6. Peak Pressure Duration Data From Experiments and Analytic Model.

Designation	Experimental Value	Analytical Value
Shot 1	131 ± 7 μ s	135.78 μ s
Shot 2	22 ± 5 μ s	17.06 μ s

The analytical values are within the measurement errors for the experimental peak pressure duration values. The experimental value of 22 μ s is an estimate of the duration, because the experimental pressure pulse on the oscilloscope was extremely short.

5.3 Analytical and Numerical Pressure Results Within an Infinite Corner.

The characteristics of the pressure history will vary at different positions throughout the flow field according to the analytic model developed in Section 3. For example, at a position along a wall forming a 100° corner, the ambient pressure is initially increased to the pressure behind the first reflected shock (see Figures 6 and 8) and then by the returning final reflected shock (see Figure 7 or 9). For a position along the plane of symmetry, the situation is different. The ambient pressure is initially increased by the incident shock (see Figure 6 or 8), then by the first reflected shock's reflection and lastly by the final curved shock (see Figure 7 or 9). Because both the DORF calculation and the analytic model simulate the gas flow within an infinite reentrant corner, their results are comparable. The comparisons are made between the analytic results and the DORF data at cells 1, 4, 30, and 31 shown in Figure 14.

Figures 35-38 compare the DORF results (solid curve) with the analytic calculations (broken curve) for Shot 2. The short duration of the analytically determined pressure plateau behind the first reflected shock in Figure 35 is the result of the 5 mm distance from the cell-center of cell 1 to the vertex. This highly transient plateau is lost in the numerical simulation probably because each shock is smeared over several cells. The final DORF least squares fitted pressure values are over 23% lower than the analytic values, and this trend persists, as is shown in Figures 36, 37 and 38. Figure 36 shows that at cell 4 the DORF values indicate the pressure plateau behind the first regular reflected shock wave. However, the duration of this constant pressure value is considerably shorter than the analytically determined plateau. Away from the edges of the pressure plateau, the DORF pressure values are within 9% of the analytic value. Because this same plateau exists for a longer period in cell 4 than in cell 1, a comparison of Figures 35 and 36 indicates that highly transient results are less likely to be accurately calculated by DORF, at least using the present computational flow field grid, than those of a pseudo-steady or steady nature. The pressure histories along the plane of symmetry (cell 30) and just off the plane of symmetry (cell 31) are depicted in Figures 37 and 38, respectively. Because the speed of the final curved reflected shock along the plane of symmetry is not known from the analytic model, the arrival time of that shock at any given position can not be determined.

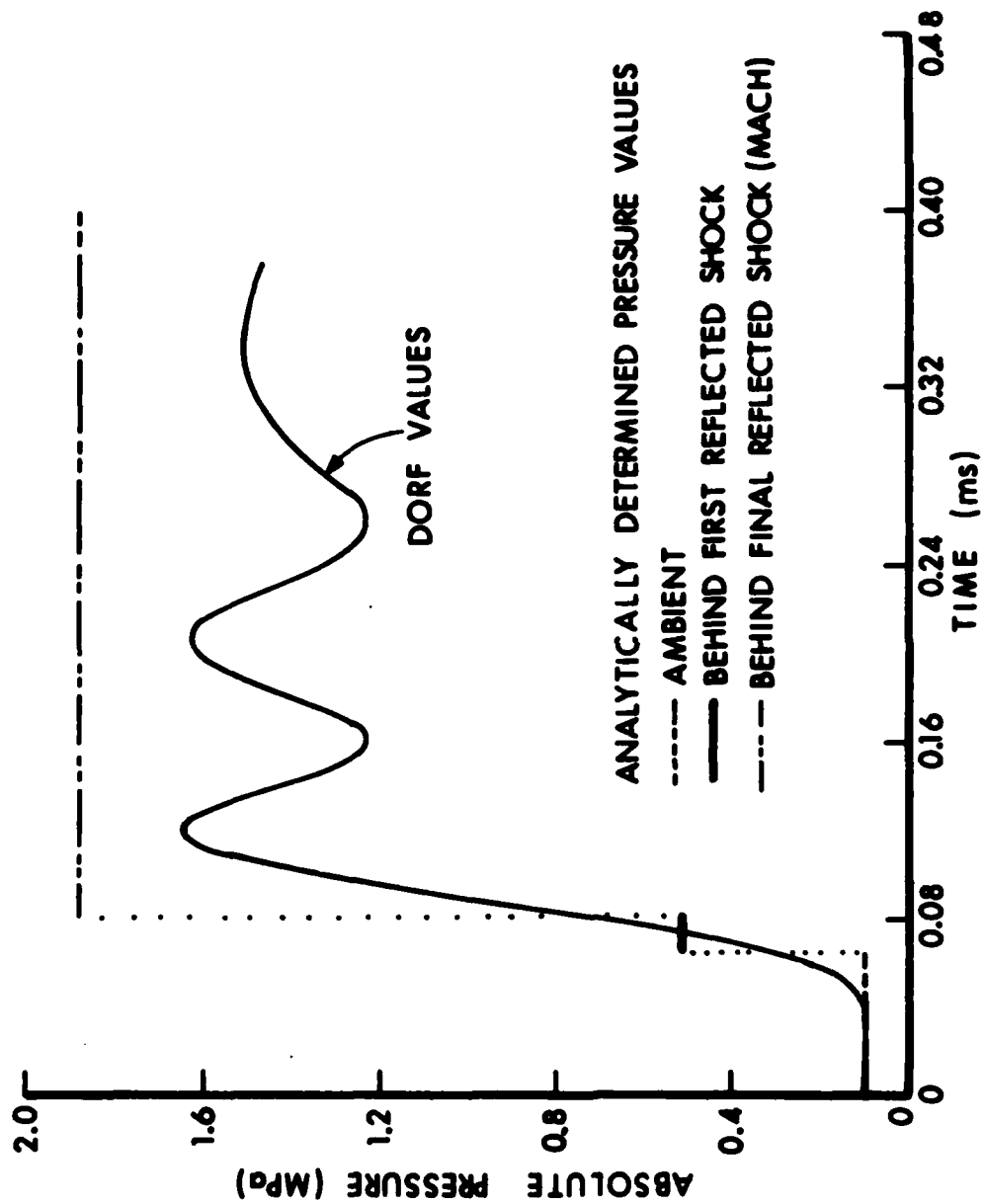


Figure 35. Comparison of the Analytic and DORF Pressure Histories at Cell 1 (5mm along the smooth boundary) for Shot 2.

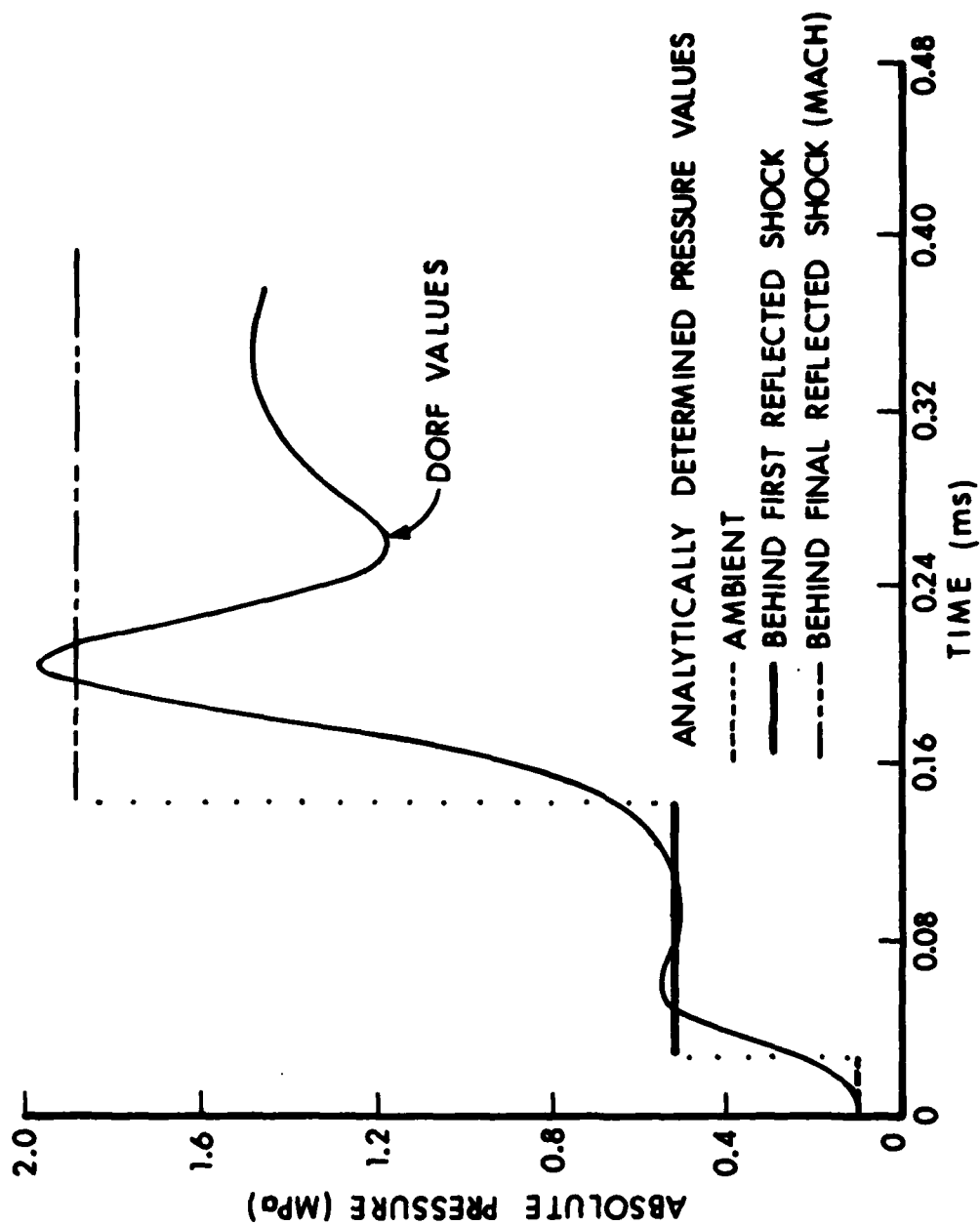


Figure 36. Comparison of the Analytic and DORF Pressure Histories at Cell 4 (35mm along the smooth boundary) for Shot 2.

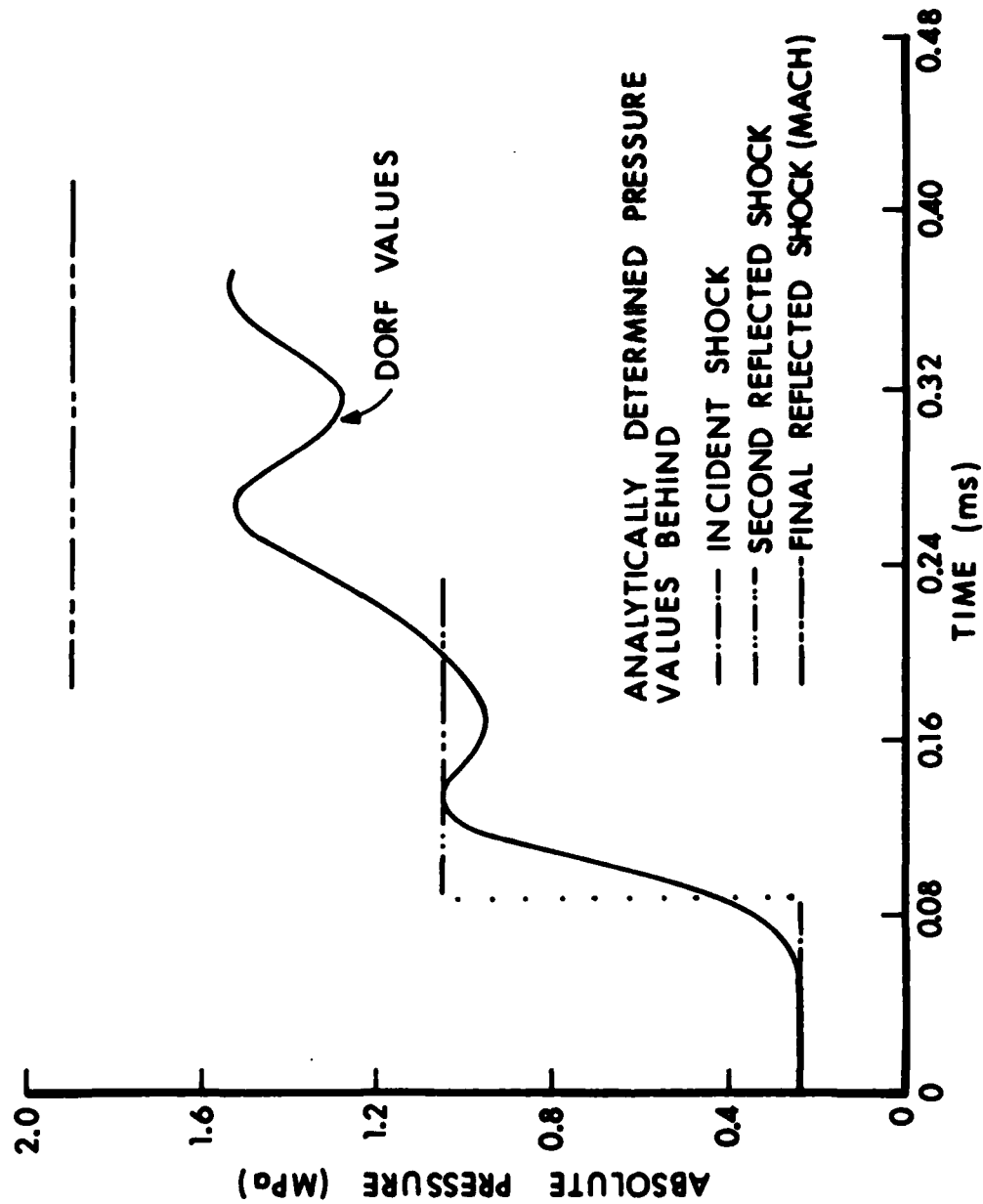


Figure 37. Comparison of the Analytic and DORF Pressure Histories at Cell 30 (55.1mm along the axis of symmetry) for Shot 2.

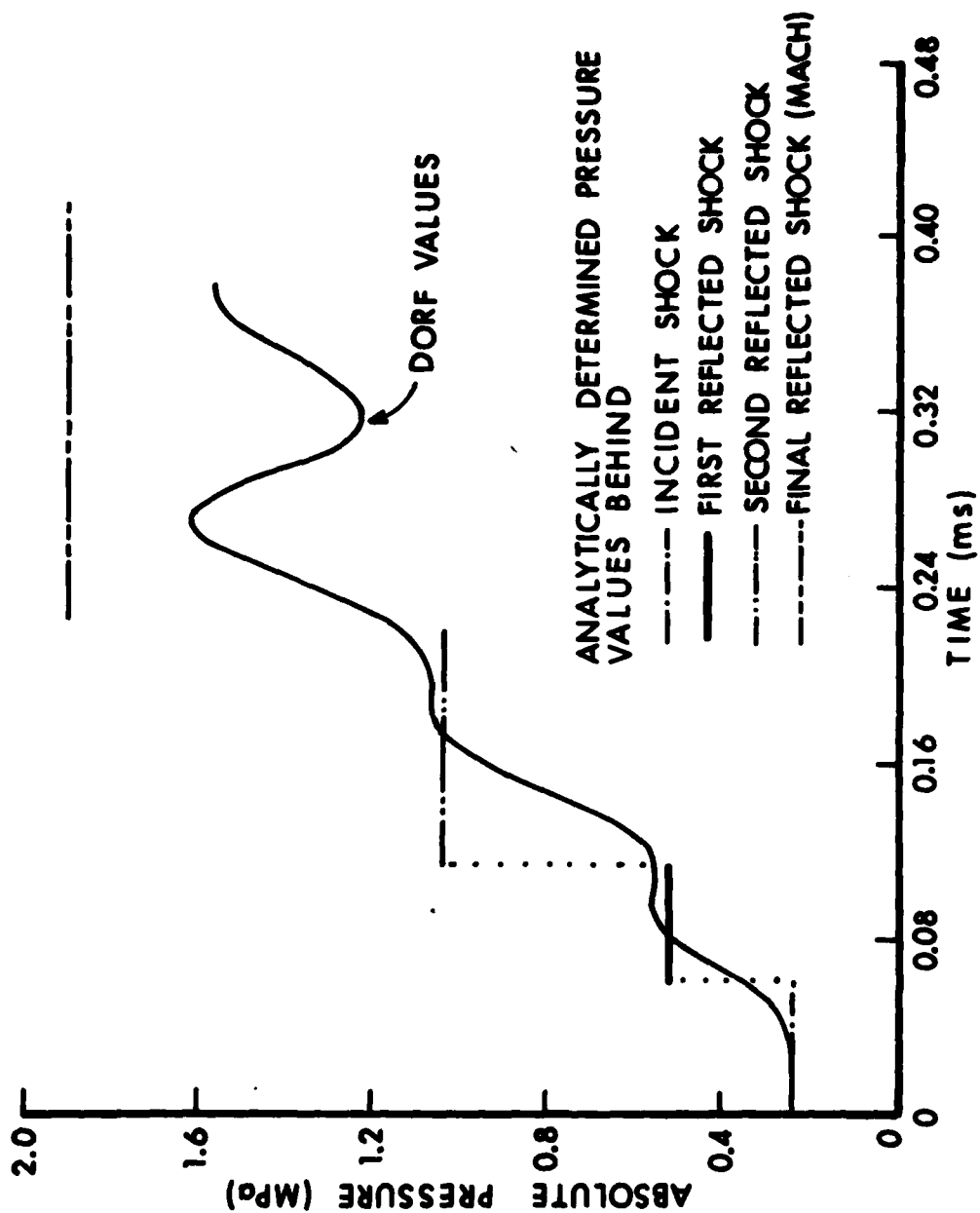


Figure 38. Comparison of the Analytic and DORF Pressure Histories at Cell 31 (off the axis of symmetry, 55.9mm from Vertex) for Shot 2.

Hence, the initiation of the final pressure plateaus in Figures 37 and 38 can not be identified. The constant pressure value behind the second reflected shock in Figure 37 is only slightly suggested by the DORF results. The discrepancy between the results is most likely due to the close proximity of cell 30 to the stair-step corner combined with the different incident angle along the stair-step wall. At cell 31 the effect of each reflection which is predicted by the analytic study can be seen in the DORF results. Although the arrival time of a given shock and the duration of the associated pressure plateau are not accurate, the distinct constant pressure values associated with regular reflection are near the analytic values. As before, the pressure values behind the Mach reflection do not compare as well as do those behind regular reflection. Because the DORF code solves a finite difference approximation to the inviscid compressible flow equations rather than the simple equation of the analytic model, Figure 38 verifies the analytic model at least qualitatively.

The pressure histories for Shot 1 calculated by the DORF code and the analytic model are compared in Figures 39-42. These figures are analogous to Figures 35-38 and many of the previously stated features are the same. The scaling used in Figures 39-42 is considerably different from that used in Figures 35-38 and care must be taken in comparing these sets. In Figure 36, the pressures from the DORF calculation and the analytic model behind the first reflected shock seem to compare more favorably than in Figure 40, at first glance. However, the opposite is true. For Shot 1, the difference is 4.7% and for Shot 2 the difference is 5.6%. Figure 39 shows the steady increase of the DORF pressure values at cell 1 from the ambient to the final peak value. The highly transient pressure plateau predicted by the analytic model is again not simulated in the DORF calculation. As discussed in Section 5.1, the analytic value is 8% higher than the least squares fit of the DORF values. This difference is approximately the same in Figures 40-42. Figures 40-42 show the pressure histories farther down the smooth boundary, on the plane of symmetry, and off the plane of symmetry, respectively. The durations of constant pressure other than those initially prescribed are not discernable in these figures. The DORF values in the intermediate pressure plateaus of Figures 40 and 41 have maximum variations of 4.7% and 7%, respectively, from the analytic values. In Figures 36 and 37 (Shot 2), the corresponding percentages are 5.6% and 8.7%, respectively. Figure 42 shows a monotonic rise in the pressure and no correspondence with the pressure plateaus.

6. CONCLUSIONS

Shock tube experiments which simulate symmetrically placed shock waves propagating into a 100° reentrant corner were performed and the pressure histories at the corner's vertex are presented. These experiments are simulated by an analytic model and by the DORF hydrodynamic

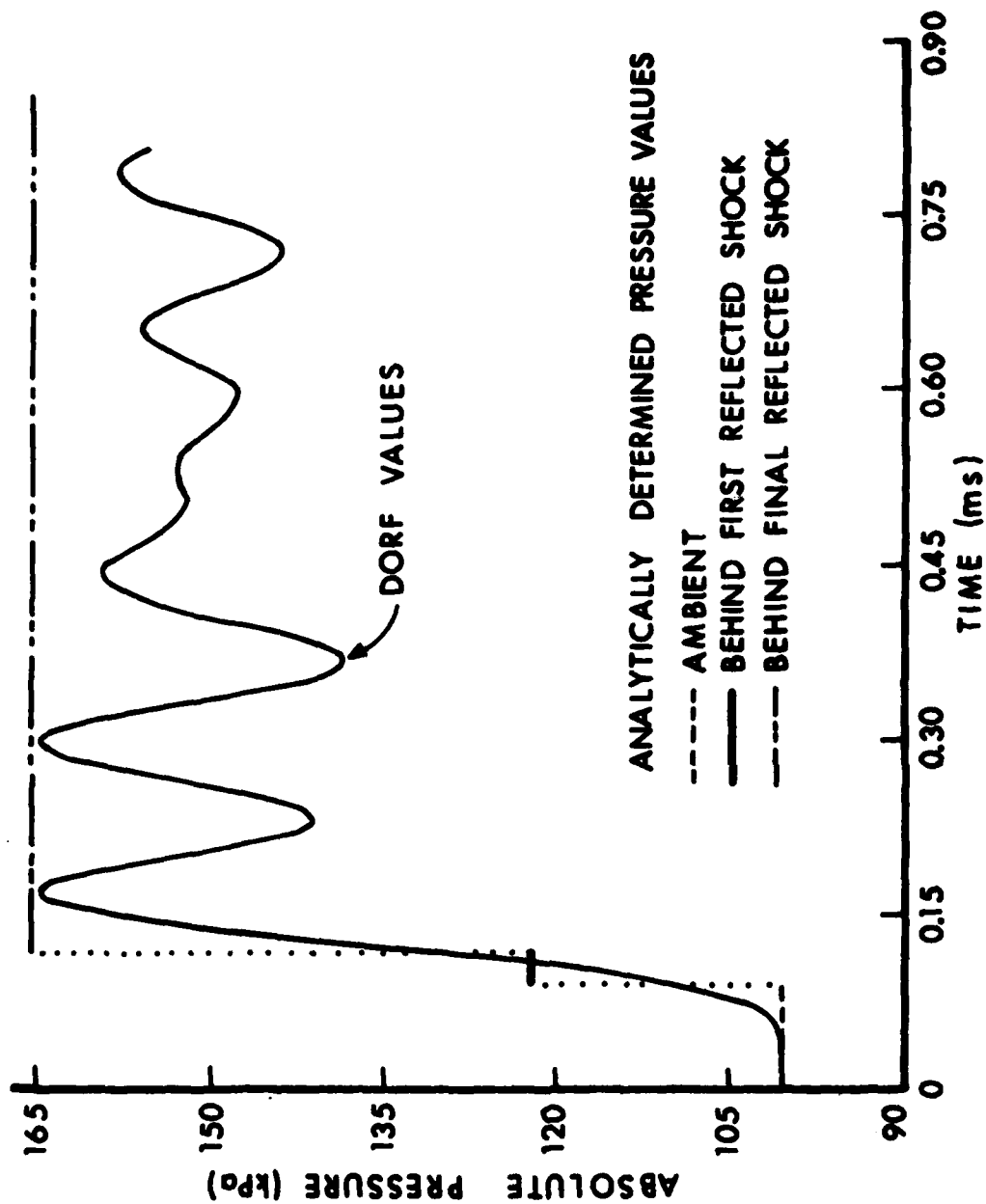


Figure 39. Comparison of the Analytic and DORF Pressure Histories at Cell 1(5 mm along the smooth boundary) for Shot 1.

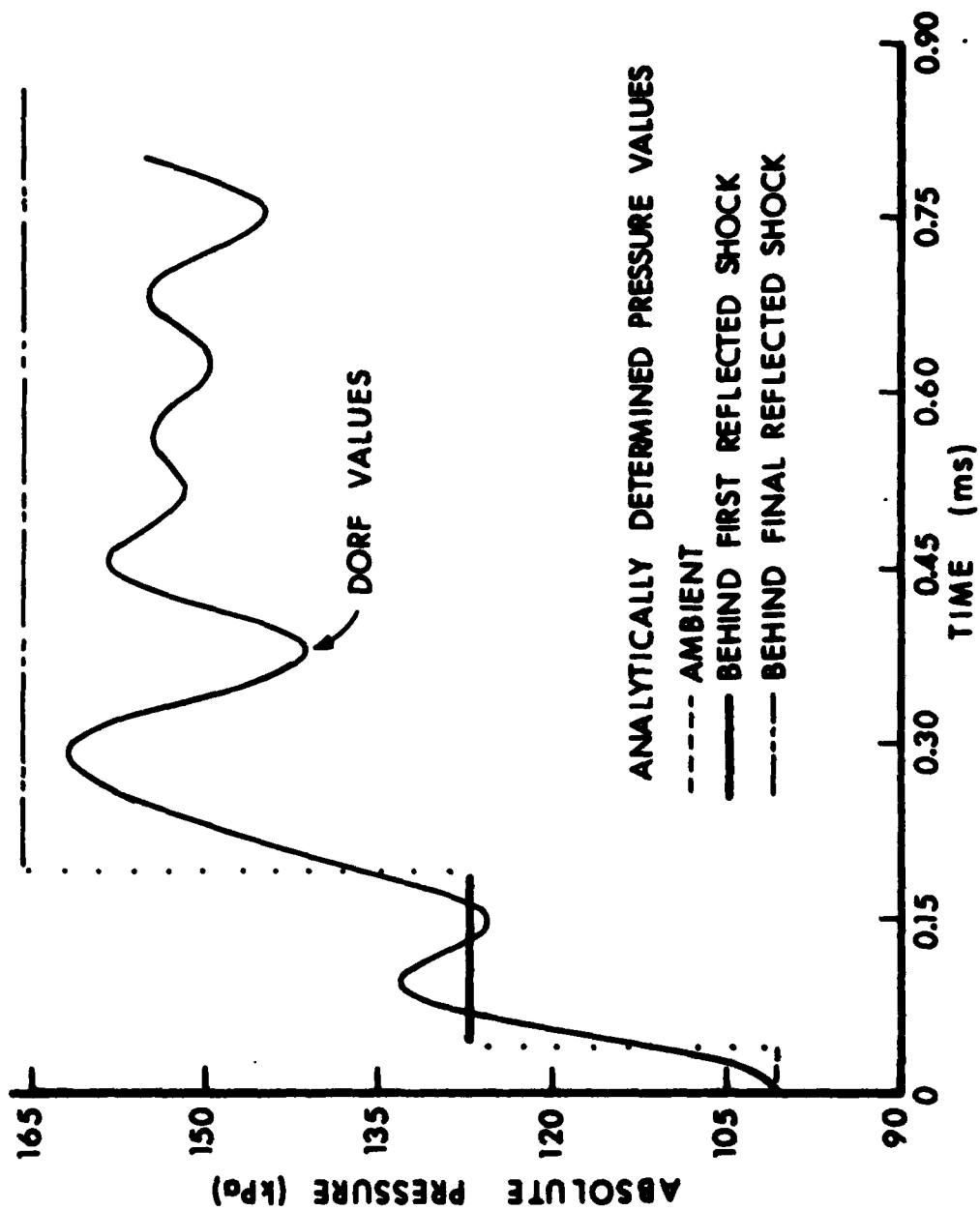


Figure 40. Comparison of the Analytic and DORF Pressure Histories at Cell 4 (35 mm along the smooth boundary) for Shot 1.

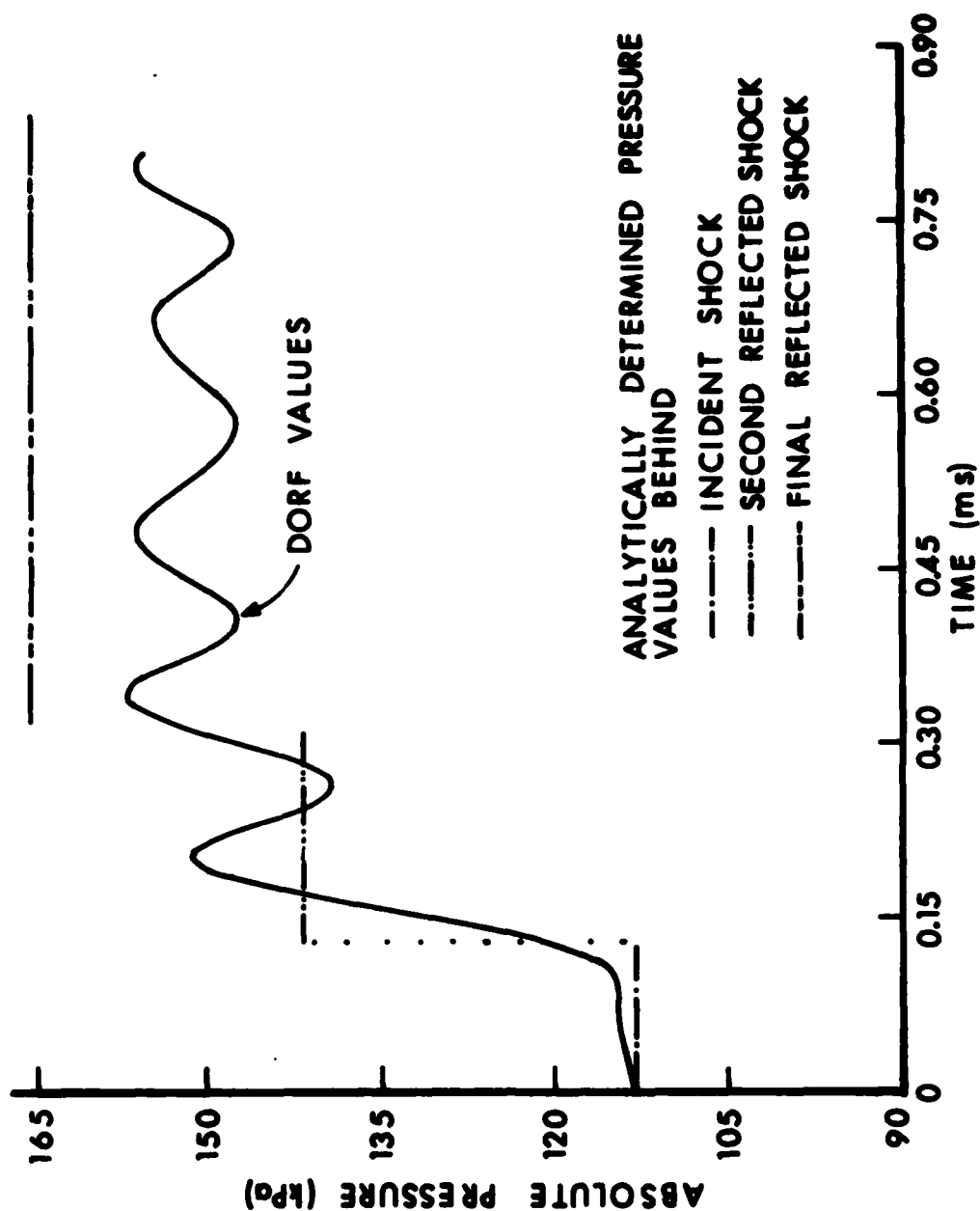


Figure 41. Comparison of the Analytic and DORF Pressure Histories at Cell 30 (55.1 mm) along the axis of symmetry) for Shot 1.

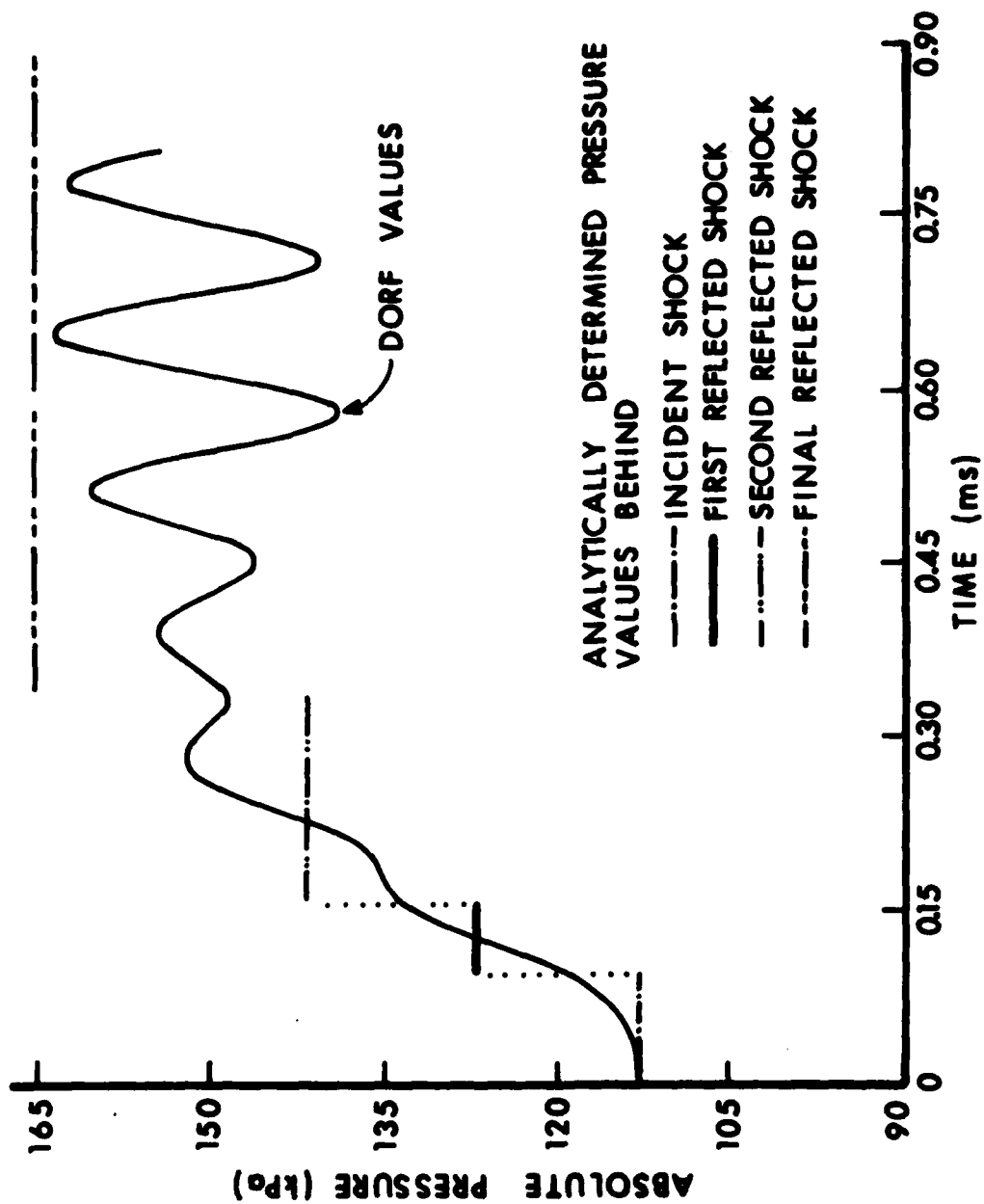


Figure 42. Comparison of the Analytic and DORF Pressure Histories at Cell 31 (off the axis of symmetry 55.9 mm from vertex) for Shot 1.

computer code. Two experiments having incident shock strengths of $P_1/P_0 = 2.3699$ (Shot 2) and $P_1/P_0 = 1.1231$ (Shot 1) are simulated by both the analytic model and numerical calculations.

A detailed description of the analytic model, which excludes real gas effects, is given. The sole restriction of the analytic study on this corner's vertex angle and incident shock strength is that complex or double Mach reflections do not occur within the corner. Thus, the model is widely applicable. Because a criterion for the type of reflection (regular and simple Mach) at each reflection point is given, the procedure indicates when the model is applicable. The mathematical techniques used in the model are simple: Galilean transformations and a method to solve a nonlinear system of algebraic equations. When the final reflected shock is not diffracted, the model calculates the exact solution of the entire flow field within an infinite corner, or the exact solution of the flow field near the vertex in a finite corner until the rarefaction wave approaches the vertex. When the final reflected shock is diffracted, the model provides an estimate of the peak vertex pressure value which is shown to be within 7% of the experimental shock tube data. For a finite corner, a formula is derived to estimate the duration of the peak pressure value at the vertex. The delineation of the corner into distinct regions by the model is verifiable by the DORF computer code simulations. Because of its predictive capabilities, the model could be used as an aid to experimental design and as a benchmark problem for hydrodynamic computer codes.

The numerical results are for a single computational mesh size. The effects of a different mesh size on the DORF results are not addressed in this report. The quantitative results for Shot 1 are significantly better than for Shot 2. For example, the peak vertex pressure value computed by DORF was less than 2% smaller than the experimental value for Shot 1 but close to 21% smaller for Shot 2. The primary feature of the DORF simulation is the use of the rigid stair-step boundary to form one of the infinite straight walls forming the 100° reentrant corner and a reflecting smooth boundary to form the other wall. The initial placement of the incident shock in the numerical simulation was such that the shock traverses a stair-step corner before reaching the vertex. This stair-step corner acts like a small reentrant corner. Therefore, the flows adjacent to the smooth and stair-step walls were significantly different from one another. The DORF code results quantitatively demonstrate the differences. The pressure profiles adjacent to the stair-step wall and smooth wall for several times and the pressure histories at corresponding positions along the walls were compared. It was found that the calculated pressures for Shot 2 at comparable smooth versus stair-step wall positions differ from one another by at least 20% and at particular positions and times up to 82%. However, these percent differences were significantly lower for Shot 1, being at most 9.2%. The comparisons showed that only after the final reflected shock passes a given cell do the pressures in corresponding cells on the two walls begin to equilibrate. The time needed for the convergence to the

same pressure value depends on the strength of the involved shocks. Consequently, the accuracy of any type of transient pressure calculations is strongly dependent on shock strength and position, and also the way in which the walls are formulated in the computational grid. Even for cells away from the stair-step corner, the pressure results may deviate by 80%. Hence, care must be taken in the interpretation and use of pressure results from a calculation involving stair-stepping to simulate a smooth plane inclined at an angle to an oncoming shock. Alternatives to stair-stepping (e.g. the utilization of partial rigid cells to model inclined surfaces or techniques for generating body conforming coordinate system) are highly recommended.

The pressure histories from the analytic model and DORF simulations are compared along the smooth boundary, and on and off the plane of symmetry. Qualitatively, the agreement between the DORF and analytic results for Shot 2 is much better than that for Shot 1. Some of the pressure plateaus predicted by the analytic model are also indicated by the numerical results. In particular, each of the cascading constant pressure regions predicted by the analytic model can be seen in the numerical calculation near the plane of symmetry (see Figure 38). However, the smearing of the shocks by the DORF code results in the distortion of some shock arrival times and in elimination of some pressure plateaus. The small amplitude oscillations in the computation for Shot 1 combined with the numerical diffusion in the computational grid make it difficult to conclusively identify a pressure plateau in the numerical results. Quantitatively the agreement between the DORF and analytic results for Shot 1 is better than that for Shot 2. For example, the numerical pressure value behind the Mach reflection in Shot 2 differs from the analytic value by 24%, while the percent difference between the numerical and analytical results for Shot 1 is at most 8%. In general, the results show that DORF models regular reflection significantly better than Mach reflection for the flow situations modeled and computational grid used.

ACKNOWLEDGMENT

The shock tube experiment was designed by Mr. William Taylor and the experimentalists were Mr. Robert Peterson and Mr. Rodney Abrahams. The first author is indebted to Dr. Raymond Sedney for his advice during the course of this work and to Mr. William Buchheister for his programming assistance. Dr. Joseph Santiago's assistance in the formulation of the computational flow field grid design is gratefully acknowledged.

REFERENCES

1. Johnson, W.E., "Code Correlation Study", AFWL-TR-70-144, U.S. Air Force Weapons Laboratory, Kirtland Air Force Base, NM (April 1971).
2. Lighthill, M.J., "The Diffraction of Blast II", Proc. Roy. Soc., Series A, Vol. 198, pp 554-65, 1950.
3. Keller, J.B., and Blank, A., "Diffraction and Reflection of Pulses by Wedges and Corners", *Communs. Pure and Appl. Math.*, Vol. IV, No. 1, pp. 75-94, 1951.
4. Keller, J.B., "Multiple Shock Reflection in Corners", *Journal of Applied Physics*, Vol. 25, No. 5, pp. 558-590, 1954.
5. Schniffman, T., Heyman, R.J., Sherman, A., and Weimer, D., "Pressure Multiplication in Re-Entrant Corners", in *Proceedings of the First Shock Tube Symposium*, Air Force Weapons Center Report No. SWR-TM-57-2 (AD467-201), 1957.
6. Goodman, H.J., "Calculations of Pressure Over the Surface of a 1/30th Scale Model Munition Magazine", ARBRL-TR-02153, US Army Ballistic Research Laboratory, Aberdeen Proving Ground, MD (April 1979). (AD #B037702L)
7. Fry, M.A., Durrett, R.E., Ganong, G.P., Matuska, D.A., Stucker, M.D., Chambers, B.S., Needham, C.E., and Westmoreland, C.D., "The HULL Hydrodynamics Computer Code", AFWL-TR-76-183, US Air Force Weapons Laboratory, Kirtland Air Force Base, NM (September 1976).
8. Fry, M.A., Needham, C.E., Stucker, M., Chambers, B.S., III, and Ganong, G.P., "AFWL HULL Calculations of Air Blast Over a Dam Slope", AFWL-TR-76-154, US Air Force Weapons Laboratory, Kirtland Air Force Base, NM (October 1976).
9. Happ, H.J., III, Needham, C.E., and Lunn, P.W., "AFWL HULL Calculations of Square-Wave Shocks on a Ramp", AFWL-TR-77-82, US Air Force Weapons Laboratory, Kirtland Air Force Base, NM (July 1977).
10. Taylor, W.J., ARRADCOM, BRL, Private Communication.
11. Thompson, P.A., Compressible Fluid Dynamics, McGraw-Hill Book Co., New York, 1972.
12. Courant, R., and Friedrichs, K.O., Supersonic Flow and Shock Waves, Vol. 1, Interscience Publishers, Inc., New York, 1948.
13. Bleakney, W., and Taub, A.H., "Interaction of Shock Waves", *Review of Modern Physics*, 21, pp. 584-605, 1949.

14. Polachek, H., and Seeger, R., "Shock Wave Interactions" in Fundamentals of Gas Dynamics, H.W. Emmons, Ed., Princeton University Press, pp. 494-504, 1958.
15. International Mathematical and Statistical Libraries, Inc., IMSL Library 3, Edition 6, IMSL, Houston, Texas, 1977.
16. Brown, K.M., "A Quadratically Convergent Newton-Like Method Based Upon Gaussian Elimination", SIAM Journal on Numerical Analysis, Vol. 6, No. 4, pp. 560-569, 1969.
17. Law, C.K., "Diffraction of Strong Shock Waves by a Sharp Compressive Corner", University of Toronto Institute for Aerospace Studies Technical Note No. 150, 1970.
18. Ben Dor, G., "Regions and Transitions of Nonstationary Oblique Shock Wave Diffractions in Perfect and Imperfect Gases", University of Toronto Institute for Aerospace Studies Technical Report No. 232, 1978.
19. Smith, L.G., "Photographic Investigation of the Reflection of Plane Shocks in Air", NDRC Report No. A-350, OSRD Report No. 6271, 1945.
20. Glasstone, S., and Dolan, P.J., "The Effects of Nuclear Weapons", Department of the Army Pamphlet No. 50-3, Headquarters, Department of the Army (March 1977).
21. Bertrand, B.P., "Measurement of Pressure in Mach Reflection of Strong Shock Waves in a Shock Tube", BRL-MR-2196, US Army Ballistic Research Laboratory, Aberdeen Proving Ground, MD (June 1972). (AD #746613)
22. Coleman, M., ARRADCOM, BRL, Private Communication.
23. Traci, R.M., Fan, J.L., and Liu, C.Y., "A Numerical Method for the Simulation of Muzzle Gas Flows With Fixed and Moving Boundaries", BRL Contract Report No. 161, June 1974. (AD #784144)

APPENDIX A

DERIVATION OF THE OBLIQUE SHOCK RELATIONS

Consider a planar discontinuity (a shock front S propagating in an inviscid fluid with velocity \vec{w} . See Figure 1A.

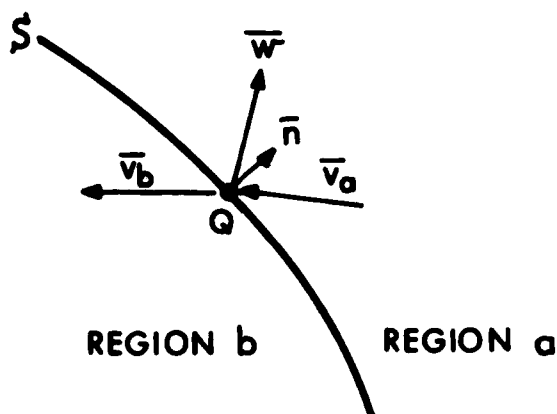


Figure 1A. A Propagating Planar Discontinuity.

The outward unit normal vector and unit tangential vector at any point Q on S are \vec{n} and \vec{t} , respectively. The fluid properties immediately ahead of the shock wave are denoted by the subscript a and those immediately behind by the subscript b . The velocity in the laboratory coordinate system, density, pressure and specific internal energy of the gas are \vec{v} , ρ , P , and I , respectively. By applying a standard control volume argument around an arbitrary position of the discontinuity and by using the principles of conservation of mass, momentum, and total energy of the discontinuity, we obtain (see Thompson¹¹ Section 7.2 or Courant and Friedrichs¹² Section 5.4)

$$\rho_b (\vec{v}_b - \vec{w}) \cdot \vec{n} - \rho_a (\vec{v}_a - \vec{w}) \cdot \vec{n} = 0, \quad (A1)$$

$$\rho_b \vec{v}_b (\vec{v}_b - \vec{w}) \cdot \vec{n} - \rho_a \vec{v}_a (\vec{v}_a - \vec{w}) \cdot \vec{n} = (P_a - P_b) \vec{n}, \quad (A2)$$

$$\begin{aligned} \rho_b \left(I_b + \frac{v_b^2}{2} \right) (\vec{v}_b - \vec{w}) \cdot \vec{n} - \rho_a \left(I_a + \frac{v_a^2}{2} \right) (\vec{v}_a - \vec{w}) \cdot \vec{n} \\ = \vec{v}_a \cdot (P_a \vec{n}) - \vec{v}_b \cdot (P_b \vec{n}), \end{aligned} \quad (A3)$$

respectively. To derive the normal momentum and tangential velocity equations of the oblique shock relations, we add to equation (A2) the quantity $(-\vec{w})$ times equation (A1) and obtain

$$\rho_b (\vec{v}_b - \vec{w}) (\vec{v}_b - \vec{w}) \cdot \vec{n} - \rho_a (\vec{v}_a - \vec{w}) (\vec{v}_a - \vec{w}) \cdot \vec{n} = (P_a - P_b) \vec{n}. \quad (A4)$$

The scalar product of equation (A4) with \vec{n} yields the conservation of normal momentum:

$$\rho_b [(\vec{v}_b - \vec{w}) \cdot \vec{n}]^2 - \rho_a [(\vec{v}_a - \vec{w}) \cdot \vec{n}]^2 = (P_a - P_b). \quad (A5)$$

The scalar product of equation (A4) with the unit tangent vector at Q combined with equation (A1) yields the continuity of tangential velocity:

$$\vec{v}_b \cdot \vec{t} = \vec{v}_a \cdot \vec{t}. \quad (A6)$$

The usual form of the conservation of energy equation for the oblique shock relations is obtained by adding $+P_b (\vec{v}_b - \vec{w}) \cdot \vec{n} - P_a (\vec{v}_a - \vec{w}) \cdot \vec{n}$ to both sides of equation (A3) and using equations (A1) and (A4) with the definition of specific enthalpy $h = I + (P/\rho)$. The result is written as

$$\left(h_b + \frac{v_b^2}{2} \right) - \left(h_a + \frac{v_a^2}{2} \right) = \vec{w} \cdot (\vec{v}_b - \vec{v}_a). \quad (A7)$$

Using equation (A6), we rewrite equation (A7) as

$$\left[h_b + \left(\frac{\vec{v}_b \cdot \vec{n}}{2} \right)^2 \right] - \left[h_a + \left(\frac{\vec{v}_a \cdot \vec{n}}{2} \right)^2 \right] = \vec{w} \cdot (\vec{v}_b - \vec{v}_a). \quad (A8)$$

Equations (A1), (A5), (A6) and (A8) are commonly known as the oblique shock relations and are valid at any point Q on the discontinuity S.

AD-AD97 471

ARMY ARMAMENT RESEARCH AND DEVELOPMENT COMMAND ABERD--ETC F/G 20/1
ANALYTIC MODEL AND NUMERICAL SIMULATION OF SHOCK WAVE PROPAGATI--ETC
JAN 81 J A SCHMITT, R E LOTTERO, H J GOODMAN

UNCLASSIFIED

ARBRL-TR-02286

SBIE-AD-E430 582

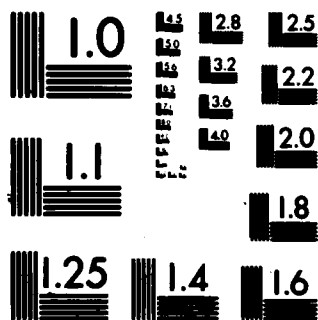
NL

END

DATE

FORMED

DTIC



MICROCOPY RESOLUTION TEST CHART
NATIONAL BUREAU OF STANDARDS-1963-A

For reference, we can rewrite equation (A7) as

$$h_b + \frac{1}{2} \left(\vec{v}_b \cdot \vec{v}_b - 2\vec{v}_b \cdot \vec{w} \right) - h_a - \frac{1}{2} \left(\vec{v}_a \cdot \vec{v}_a - 2\vec{v}_a \cdot \vec{w} \right) = 0,$$

or

$$h_b + \frac{1}{2} (v_b - w)^2 - h_a - \frac{1}{2} (v_a - w)^2 = 0. \quad (A9)$$

Using equation (A6), equation (A9) reduces to

$$h_b + \frac{1}{2} \left[(\vec{v}_b - \vec{w}) \cdot \vec{n} \right]^2 - h_a - \frac{1}{2} \left[(\vec{v}_a - \vec{w}) \cdot \vec{n} \right]^2 = 0. \quad (A10)$$

APPENDIX B

EXPLICIT FORMULAS FOR OBLIQUE SHOCK CALCULATIONS

We derive the explicit formulas from the equation system (3.1.5) through (3.1.8) as follows. We multiply equation (3.1.6) by the quantity

$\frac{1}{2} \left[\frac{1}{\rho_1} + \frac{1}{\rho_0} \right]$, use equation (3.1.5) and obtain

$$\frac{1}{2}(P_1 - P_0) \left[\frac{1}{\rho_1} + \frac{1}{\rho_0} \right] = 0.5 \left[u_0^2 \sin^2 \phi_0 - u_1^2 \sin^2(\phi_0 - \theta_1) \right]. \quad (B1)$$

Rewriting equation (3.1.8) in terms of pressure and density instead of enthalpy, we have

$$\frac{\gamma}{\gamma-1} \left[\frac{P_1}{\rho_1} - \frac{P_0}{\rho_0} \right] = 0.5 \left[u_0^2 \sin^2 \phi_0 - u_1^2 \sin^2(\phi_0 - \theta_1) \right]. \quad (B2)$$

We equate the left hand sides of equation (B1) and (B2). Multiplying the resulting equation by the ratio ρ_1/P_0 , we obtain the density in region 1 in terms of γ , P_1/P_0 and ρ_0 :

$$\rho_1 = \rho_0 \left\{ \left[\frac{\gamma+1}{\gamma-1} \frac{P_1}{P_0} + 1 \right] \left[\frac{P_1}{P_0} + \frac{\gamma+1}{\gamma-1} \right] \right\}. \quad (B3)$$

The ratio of equations (3.1.5) and (3.1.7) is

$$\rho_1 \tan(\phi_0 - \theta_1) = \rho_0 \tan \phi_0. \quad (B4)$$

From equation (B4), the deflection angle θ_1 can be expressed as

$$\theta_1 = \phi_0 - \tan^{-1} \left[(\rho_0 \tan \phi_0) / \rho_1 \right]. \quad (B5)$$

The velocity magnitude in region 0 can be expressed in terms of the quantities u_1 , ϕ_0 and θ_1 from equation (3.1.7)

$$u_0 = u_1 \cos(\phi_0 - \theta_1) / (\cos \phi_0). \quad (B6)$$

Using equation (B6), we can rewrite equation (3.1.6) as

$$(P_1 - P_0)/\cos^2(\phi_0 - \theta_1) = u_1^2 \left[-\rho_1 \tan^2(\phi_0 - \theta_1) + \rho_0 \tan^2 \phi_0 \right]. \quad (B7)$$

Using equation (B5), we rewrite equation (B7) as

$$u_1 = \pm \left[\frac{P_1 - P_0}{\rho_1 - \rho_0} \frac{\rho_0}{\rho_1} \right]^{1/2} \sin(\phi_0 - \theta_1). \quad (B8)$$

By solving equations (B3), (B5), (B8), and (B6) in order and by applying the perfect gas relations $h_1 = \gamma P_1 / [(\gamma - 1)\rho_1]$, $T_1 = P_1 / (R^* \rho_1)$, and $a_1 = (\gamma P_1 / \rho_1)^{1/2}$, we obtain all the values of the flow variables in the intersection of region 1 and a neighborhood of the reflection point Q.

LIST OF SYMBOLS

a	= sound speed (m/s)
c_p	= specific heat at constant pressure (J/(kg·K))
c_v	= specific heat at constant volume (J/kg·K))
d	= distance from the corner's apex (mm)
d_{\min}	= minimum dimension of a cell (mm)
d_p	= distance defined by equation (3.3.1) (m)
d_r	= distance rarefaction wave travels in t_w (m)
d_w	= length of wall forming a finite corner (m)
E	= specific total energy (J/kg)
\vec{g}	= gravitational acceleration (m/s ²)
h	= specific enthalpy (J/kg)
I	= specific internal energy (J/kg)
\vec{n}	= unit outer normal vector
P	= absolute pressure (Pa)
Q	= point at which shock reflection occurs
R^*	= gas constant (J/(kg·K))
S	= surface of discontinuity
T	= temperature (K)
\vec{t}	= unit tangential vector
t^+, t^*	= defined by equations (3.3.2) and (3.3.3), respectively (s)
t_w	= time taken for incident shock to traverse d_w (s)
\vec{u}	= velocity vector in the shock-fixed coordinate system $u_x \hat{i} + u_y \hat{j}$ (m/s)
\vec{v}	= velocity vector in laboratory coordinate system $v_x \hat{i} + v_y \hat{j}$ (m/s)
\vec{w}	= shock wave velocity vector (m/s)
Z	= triple point in the Mach reflection configuration
ΔS_x	= step size in the x direction (mm)
ΔS_y	= step size in the y direction (mm)

Δt = time step selected by DORF code (s)
 Δx = computational cell size in the x direction (mm)
 Δy = computational cell size in the y direction (mm)
 γ = ratio of specific heats = c_p/c_v
 δ = reentrant corner angle variation from 90° ($^\circ$)
 η = Courant-Friedrichs-Lewy stability factor
 θ_i = deflection angle of the incoming velocity as it passes through a shock into region i ($^\circ$)
 θ_w = angle a wall makes with the horizontal ($^\circ$)
 ν, λ = kinematic and bulk viscosity coefficient, respectively, (Pa-s)
 ρ = density (kg/m^3)
 τ = heat transfer coefficient ($\text{W/(m}^2\cdot\text{K)}$)
 ϕ_B = incident angle of initial shock along the smooth wall ($^\circ$)
 ϕ_i = the incident angle of the velocity in region i at the shock front ($^\circ$)
 ϕ_L = incident angle of initial shock along the stair-step wall ($^\circ$)
 χ = trajectory angle of the triple point in Mach Reflections ($^\circ$)

Subscripts

a denotes gas flow variables ahead of the shock
 b denotes gas flow variables behind the shock
 F denotes the gas flow variables in the last region
 i denotes region i, $i=1,2,3,4,5$
 0 denotes initial region or region 0

Operators

$\nabla \times$ = curl operator
 $\nabla \cdot$ = divergence operator
 ∇ = gradient operator

DISTRIBUTION LIST

<u>No. of Copies</u>	<u>Organization</u>	<u>No. of Copies</u>	<u>Organization</u>
12	Commander Defense Technical Info Center ATTN: DDC-DDA Cameron Station Alexandria, VA 22314	1	Director Institute for Defense Analyses ATTN: IDA Librarian 400 Army-Navy Drive Arlington, VA 22202
4	Under Secretary of Defense for Research & Engineering ATTN: DD/TWP DD/S&SS(OS) DD/I&SS AD/SW Washington, DC 20301	1	Director Weapons Systems Evaluation Group ATTN: Document Control Washington, DC 20305
2	Asst. to the Secretary of Defense (Atomic Energy) ATTN: Document Control D.R. Cotter Washington, DC 20301	1	Director National Security Agency ATTN: E.F. Butala, R15 Ft. George G. Meade, MD 20755
3	Director Defense Advanced Research Projects Agency ATTN: Tech Lib NMRO PMO 1400 Wilson Boulevard Arlington, VA 22209	1	Director Joint Strategic Target Planning Staff JCS ATTN: Sci & Tech Info Lib Omaha, NB 68113
2	Director Federal Emergency Management Agency ATTN: Hazard Eval & Vul Red Div, G. Sisson Tech Lib Washington, DC 20301	4	Director Defense Communications Agency ATTN: Code 930 Washington, DC 20305
5	Director Defense Intelligence Agency ATTN: DT-1B DB-4C/E.O. Farrell DT-2/Wpns & Sys Div RDS-3A4 DB-4M Washington, DC 20301	6	Director Defense Nuclear Agency ATTN: DDST/Dr. Conrad DDST/Dr. Oswald STTL/Tech Lib (2 cys) SPSS (2 cys) Washington, DC 20305

DISTRIBUTION LIST

<u>No. of Copies</u>	<u>Organization</u>	<u>No. of Copies</u>	<u>Organization</u>
2	Commander Field Command, DNA ATTN: FCPR FCTMOR Kirkland AFB, NM 87115	2	Deputy Chief of Staff for Operations and Plans ATTN: Technical Library Dir of Chemical & Nuclear Operations Department of the Army Washington, DC 20310
1	Commander Field Command, DNA Livermore Division ATTN: FCPRL P.O. Box 308, L-317 Livermore, CA 94550	2	HQDA (DAMA-AR; NCL Div) Washington, DC 20310
1	Director Interservice Nuclear Wpns School ATTN: TTV Kirkland AFB, NM 87115	2	Office, Chief of Engineers Department of the Army ATTN: DAEN-MCE-D DAEN-RDM 890 S. Pickett Street Alexandria, VA 22304
1	Commandant NATO School (SHAPE) ATTN: U.S. Documents Ofcr APO New Yor, NY 09172	1	Commander US Army Engineer Center ATTN: DT-LRC Fort Belvoir, VA 22060
1	Program Manager US Army BMD Program Office ATTN: J. Shea 5001 Eisenhower Avenue Alexandria, VA 22333	6	Commander US Army Engineer Waterways Experiment Station ATTN: Technical Library W. Flathau J.N. Strange G. Jackson L. Ingram J. Drake P.O. Box 631 Vicksburg, MS 39180
2	Director US Army BMD Advanced Technology Center ATTN: ATC-T 1CRDABH-X Huntsville, AL 35807	1	Commander US Army Engineering Center ATTN: ATSEN-SY-L Fort Belvoir, VA 22060
1	Commander US Army BMD System Command ATTN: BDMSC-TFN/N.J. Hurst P.O. Box 1500 Huntsville, AL 35807	1	Division Engineer US Army Engineering Division ATTN: HNDHD-SR Huntsville Box 1600, W. Station Huntsville, AL 35807

DISTRIBUTION LIST

<u>No. of Copies</u>	<u>Organization</u>	<u>No. of Copies</u>	<u>Organization</u>
1	Division Engineer US Army Engineering Division Ohio River ATTN: DRDAS-L (Tech Lib) P.O. Box 1159 Cincinnati, OH 45201	1	Commander US Army Aviation Research and Development Command ATTN: DRSAB-E P.O. Box 209 St. Louis, MO 63166
1	Commander US Army Material Development and Readiness Command ATTN: DRCDMD-ST 5001 Eisenhower Avenue Alexandria, VA 22333	1	Director US Army Air Mobility Research and Development Laboratory Ames Research Center Moffett Field, CA 94035
1	Commander US Army Material Development and Readiness Command ATTN: DRXAM-T1 5001 Eisenhower Avenue Alexandria, VA 22333	1	Commander US Army Communications Research and Development Command ATTN: DRDCO-PPA-SA Fort Monmouth, NJ 07703
5	Commander US Army Armament Research and Development Command ATTN: DRDAR-LCN, P. Angelotti (2 cys) DRDAR-LCN-F, W. Reiner DRDAR-TSS (2 cys) Dover, NJ 07801	6	Commander US Army Electronics Research and Development Command ATTN: DELSD-L DELEW-R, W.S. McAfee R. Frieberg DELSA-EI, J. Roma DELSA-EM, A. Sigismondi C. Goldy Fort Monmouth, NJ 07703
1	Commander US Army Armament Material Readiness Command ATTN: DRSAR-LEP-I, Tech Lib Rock Island, IL 61299	5	Commander US Army Harry Diamond Labs ATTN: J. Gaul L. Belliveau J. Gwaltney F.W. Wizenitz B. Vault 2800 Powder Mill Road Adelphi, MD 20783
2	Director US Army Armament Research and Development Command Benet Weapons Laboratory ATTN: DRDAR-LCB-TL, Tech Lib Watervliet, NY 12189		

DISTRIBUTION LIST

<u>No. of Copies</u>	<u>Organization</u>	<u>No. of Copies</u>	<u>Organization</u>
6	Commander US Army Harry Diamond Labs ATTN: DRXDO-TI DRXDO-TI/012 DRXDO-NP DRXDO-RBH, P. Caldwell DRXDO-RBA, J. Rosado DELHD-1-TL, Tech Lib 2800 Powder Mill Road Adelphi, MD 20783	1	Commander US Army Materials and Mechanics Research Center ATTN: Technical Library Watertown, MA 02172
1	Commander US Army Missile Command ATTN: DRSMI-R Redstone Arsenal, AL 35809	1	Commander US Army Research Office P.O. Box 12211 Research Triangle Park NC 27709
2	Commander US Army Missile Command ATTN: DRSMI-YDL DRSIC Redstone Arsenal, AL 35809	2	Commander US Army Nuclear Agency ATTN: ACTA-NAW Technical Library 7500 Backlick Road, Bldg 2073 Springfield, VA 22150
2	Commander US Army Natick Research and Development Command ATTN: DRXRE, D. Sieling DRXNM-UE Natick, MA 01762	1	Commander US Army Training & Doctrine Cmd ATTN: ATCD-SA, O. Wells Fort Monroe, VA 23651
1	Commander US Army Tank Automotive Resch and Development Command ATTN: DRDTA-UL Warren, MI 48090	1	Commander Combined Arms Combat Dev Act ATTN: ATCA-CO, L.C. Plegar Fort Leavenworth, KS 66027
1	Commander US Army Foreign Science & Technology Center ATTN: Resch & Concepts Branch 220 7th Street, NE Charlottesville, VA 22901	2	Director US Army TRADOC Systems Analysis Activity ATTN: LTC J. Hesse ATAA-SL, Tech Lib White Sands Missile Range NM 88002
1	Commander US Army Logistical Center ATTN: ATCL-SCA, R. Cameron Fort Lee, VA 23801	2	Office of Naval Research ATTN: Code 715, Tech Lib Code 474, N. Perrone Arlington, VA 22217
		2	Chief of Naval Operations ATTN: OP-03EG OP-985F Department of the Navy Washington, DC 20350

DISTRIBUTION LIST

<u>No. of Copies</u>	<u>Organization</u>	<u>No. of Copies</u>	<u>Organization</u>
1	Headquarters Naval Materiel Command ATTN: MAT 08T-22 Washington, DC 20360	4	Officer-in-Charge Civil Engineering Laboratory Naval Constr Btn Ctr ATTN: S. Takahaski R.J. Odello J. Crawford Tech Lib Port Hueneme, CA 93041
1	Chief of Naval Material ATTN: MAT 0323 Department of the Navy Arlington, VA 22217	2	Commander Naval Ship Engineering Center ATTN: Tech Lib NSEC 6105G Hyattsville, MD 20782
1	Director Strategic Systems Projects Office ATTN: NSP-43, Tech Lib Department of the Navy Washington, DC 20360	1	Commander Naval Surface Weapons Center ATTN: DX-21, Library Branch Dahlgren, VA 22448
1	Commander Naval Electronic Systems Cmd ATTN: PME 117-21 Washington, DC 20360	2	Commander Naval Surface Weapons Center ATTN: Code F31 Code WX21, Tech Lib Silver Spring, MD 20910
3	Commander Naval Facilities Engineering Command ATTN: Code 03T Code 04B Washington, DC 20360	1	Commander Newport Laboratory Naval Underwater Sys Center ATTN: Code EM, J. Kalinowski Newport, RI 02840
2	Commander Naval Sea Systems Command ATTN: ORD-91313 Library Code 03511 Department of the Navy Washington, DC 20362	2	Commander Naval Weapons Center ATTN: Code 533, Tech Lib Code 40701, M. Keith China Lake, CA 93555
1	Commander David W. Taylor Naval Ship Research & Devel. Center ATTN: Lib Div, Code 522 Bethesda, MD 20084	2	Commander Naval Ship Research & Dev Center Facility Underwater Explosions Resch Div ATTN: Code 17, W.W. Murray Tech Lib Portsmouth, VA 23709

DISTRIBUTION LIST

<u>No. of Copies</u>	<u>Organization</u>	<u>No. of Copies</u>	<u>Organization</u>
1	Commander Naval Weapons Evaluation Facility ATTN: Code 10, Tech Lib Kirtland AFB Albuquerque, NM 87117	1	AFATL (DLYV, J. Flint) Eglin AFB, FL 32542
		1	AFATL (DLYV, P. Nash) Eglin AFB, FL 32542
2	Director Naval Research Laboratory ATTN: Code 2027, Tech Lib Code 8440, F. Rosenthal Washington, DC 20375	1	ADTC (Tech Lib) Eglin AFB, FL 32542
		1	Commander RADC (TSLD) Griffis AFB, NY 13341
1	Superintendent Naval Postgraduate School ATTN: Code 0142, Tech Rpts Monterey, CA 93940	1	Air Force Geophysics Lab ATTN: LWV, K. Thompson Hanscom AFB, MA 01731
1	President Naval War College ATTN: E-11, Tech Service Newport, RI 02840	6	AFWL, AFSC ATTN: DES, J. Thomas R. Julley J. Shinn DE, M. Plamoncon SUL NTES-B, R. Guice Kirtland AFB Albuquerque, NM 87117
1	HQ USAF (INT) Washington, DC 20330		
1	HQ USAF (PRE) Washington, DC 20330	1	Ballistic Missile Office/MN Air Force Systems Command ATTN: MNN Norton AFB, CA 92409
1	Deputy Chief of Staff Logistics & Engineering Department of the Air Force ATTN: LEEE Washington, DC 20330	2	Commander-in-Chief Strategic Air Command ATTN: NRI-STINFO Lib XPFS Offut AFB, NE 68113
1	Deputy Chief of Staff Rsch, Dev, & Acq Department of the Air Force ATTN: AFRDQSM Washington, DC 20330	1	FID (NIIS, Library) Wright-Patterson AFB, OH 45433
2	AFSC (DLW; Tech Lib) Andrews AFB Washington, DC 20334	1	AFIT (Lib, Bldg 640, Area B) Wright-Patterson AFB, OH 45433

DISTRIBUTION LIST

<u>No. of Copies</u>	<u>Organization</u>	<u>No. of Copies</u>	<u>Organization</u>
1	Director US Bureau of Mines ATTN: Tech Lib Denver Federal Center Denver, CO 80225	2	Oak Ridge National Lab Nuclear Division ATTN: Doc Ctl for Tech Lib Civ Defse Rsch Proj P.O. Box X Oak Ridge, TN 37830
1	Director US Bureau of Mines Twin Cities Research Ctr ATTN: Tech Lib P.O. Box 1660 Minneapolis, MN 55111	5	Sandia Laboratories ATTN: Doc Ctl for 3141 Sandia Rpt Collection A.M. Chabai M.L. Merritt L.J. Vortman L. Hill P.O. Box 5800 Albuquerque, NM 87115
1	Department of Energy Albuquerque Operations Ofc ATTN: Doc Ctl for Tech Lib P.O. Box 5400 Albuquerque, NM 87115	1	Sandia Laboratories Livermore Laboratory ATTN: Doc Ctl for Tech Lib P.O. Box 969 Livermore, CA 94550
7	Director Lawrence Livermore Labs ATTN: L-90, R.G. Dong L-96, L.W. Woodruff L-7, J. Kahn L-3, Tech Info L-200, T. Butkovich L-437, R. Schock L-205, J.R. Hearst P.O. Box 808 Livermore, CA 94550	1	Director National Aeronautics & Space Administration Scientific and Technical Information Facility P.O. Box 8757 BWI Airport, MD 21240
3	Director Los Alamos Scientific Lab ATTN: Doc Ctl for Rpts Lib R.A. Gentry R. Bridwell P.O. Box 1663 Los Alamos, NM 87544	1	Director ATTN: Mr. J.C. Nall P.O. Box 1925 Washington, DC 20505
1	Department of Energy Nevada Operations Ofc ATTN: Doc Ctl for Tech Lib P.O. Box 14100 Las Vegas, NV 89114	2	Aerospace Corporation ATTN: Tech Info Services P.N. Mathur P.O. Box 92957 Los Angeles, CA 90009

DISTRIBUTION LIST

<u>No. of Copies</u>	<u>Organization</u>	<u>No. of Copies</u>	<u>Organization</u>
1	Agbabian Associates ATTN: M. Agbabian 250 North Nash Street El Segundo, CA 90245	1	Calspan Corporation ATTN: Technical Library P.O. Box 400 Buffalo, NY 14225
1	Applied Theory, Inc. ATTN: J.G. Trulio 1010 Westwood Blvd. Los Angeles, CA 90024	1	Civil Systems, Inc. ATTN: J. Bratton 2201 San Pedro, N.E. Albuquerque, NM 87110
1	AVCO ATTN: Res Lib A830, Rm 7201 201 Lowell Street Wilmington, MA 01887	1	EG&G, Incorporated Albuquerque Division ATTN: Technical Library P.O. Box 10218 Albuquerque, NM 87114
2	BDM Corporation ATTN: Library T. Neighbors 7915 Jones Branch Drive McLean, VA 22102	1	General American Trans. Corp. General American Research Div. ATTN: G.L. Neidhardt 7449 N. Natchez Avenue Niles, IL 60648
1	The BDM Corporation ATTN: R. Hensley P.O. Box 9274 Albuquerque International Albuquerque, NM 87119	1	General Electric Company-TEMPO ATTN: DASIAC P.O. Drawer QQ Santa Barbara, CA 93102
1	The Boeing Company ATTN: Aerospace Library P.O. Box 3707 Seattle, WA 98124	1	General Electric-TEMPO ATTN: E. Bryant 220 S. Main Street, Rm 206 Bel Air, MD 21014
3	California Research and Technology, Inc. ATTN: K. Kreyenhagen S. Shuster Tech Lib 6269 Variel Avenue Woodland Hills, CA 91364	1	J.H. Wiggins Co., Inc. ATTN: J. Collins 1650 South Pacific Coast Hiway Redondo Beach, CA 90277
1	California Research and Technology, Inc. ATTN: D. Orphal 4049 First Street Livermore, CA 94550	4	Kaman Avidyne ATTN: N.P. Hobbs (2 cys) S. Criscione Library 83 Second Avenue Northwest Industrial Park Burlington, MA 01830

DISTRIBUTION LIST

<u>No. of Copies</u>	<u>Organization</u>	<u>No. of Copies</u>	<u>Organization</u>
2	Kaman Sciences Corporation ATTN: Library F.H. Shelton P.O. Box 7463 Colorado Springs, CO 80933	3	Physics International Corp. ATTN: E.T. Moore C. Vincent F.M. Sauer 2700 Merced Street San Leandro, CA 94577
2	Lockheed Missiles and Space College ATTN: Technical Library T. Geers 3251 Hanover Street Palo Alto, CA 94304	3	Physics International Corp. ATTN: J. Thomsen L.A. Behrmann Technical Library 2700 Merced Street San Leandro, CA 94577
2	Martin Marietta Aerospace Orlando Division ATTN: G. Fotieo Mail Point 505, C. Luongo P.O. Box 5837 Orlando, FL 32805	7	R&D Associates ATTN: J. Carpenter B. Port C. MacDonald A. Latter W. Wright J.G. Lewis Technical Library P.O. Box 9695 Marina del Rey, CA 90291
2	McDonnell Douglas Astronautics Corporation ATTN: R.W. Halprin C. Gardiner 5301 Bolsa Avenue Huntington Beach, CA 92647	1	R&D Associates ATTN: H. Cooper Suite 500 1401 Wilson Boulevard Arlington, VA 22209
2	Merritt Cases, Inc. ATTN: J.L. Merritt Technical Library P.O. Box 1206 Redlands, CA 92373	1	The Rand Corporation ATTN: C.C. Mow 1700 Main Street Santa Monica, CA 90406
1	Pacific Sierra Research Corp. ATTN: H. Brode 1456 Cloverfield Boulevard Santa Monica, CA 90404	3	Science Applications, Inc. ATTN: J. Cockayne W. Layson J. McGahan 8400 Westpark Drive McLean, VA 22102
1	Pacifica Technology ATTN: R. Bjork P.O. Box 148 Del Mar, CA 92014		

DISTRIBUTION LIST

<u>No. of Copies</u>	<u>Organization</u>	<u>No. of Copies</u>	<u>Organization</u>
2	Science Applications, Inc. ATTN: B. Bernstein D. Maxwell 2450 Washington Street Suite 120 San Leandro, CA 94577	1	TRW Systems Group ATTN: E. Wong San Bernardino Operations P.O. Box 1310 San Bernardino, CA 92402
1	Science Applications, Inc. ATTN: Technical Library P.O. Box 2351 La Jolla, CA 92038	1	Universal Analytics, Inc. ATTN: E.I. Field 7740 W. Manchester Blvd. Playa del Rey, CA 90291
4	Systems, Science and Software, Inc. ATTN: D.R. Grine T. Cherry T.D. Riney Tech Library P.O. Box 1620 La Jolla, CA 92038	1	Vela Seismological Center ATTN: G. Ullrich 312 Montgomery Street Alexandria, VA 22314
1	Systems, Science and Software, Inc. ATTN: J. Murphy 11800 Sunrise Valley Drive Reston, VA 22091	1	Weidlinger Assoc. Consulting Engineers ATTN: J. Isenberg 3000 Sand Hill Road Menlo Park, CA 94025
3	Terra Tek, Inc. ATTN: S. Green A. Abou-Sayed Tech Library 420 Wakara Way Salt Lake City, UT 84108	1	Weidlinger Assoc. Consulting Engineers ATTN: M.L. Baron 110 East 59th Street New York, NY 10022
2	Terra Tek, Inc. ATTN: Li-San Hwang Technical Library 630 North Rosemead Blvd. Pasadena, CA 91107	1	Westinghouse Electric Company Marine Division ATTN: W.A. Volz Hendy Avenue Sunnyvale, CA 94008
4	TRW Systems Group ATTN: P. Dai B. Sussoltz P. Bhutta Tech Info Ctr/S-1930 One Space Park Redondo Beach, CA 92078	1	Battelle Memorial Institute ATTN: Technical Library 505 King Avenue Columbus, OH 43201
		1	California Institute of Tech. ATTN: T.J. Ahrens 1201 E. California Blvd. Pasadena, CA 91109

DISTRIBUTION LIST

<u>No. of Copies</u>	<u>Organization</u>	<u>No. of Copies</u>	<u>Organization</u>
2	Denver Research Institute University of Denver ATTN: J. Wisotaki Technical Library P.O. Box 10127 Denver, CO 80210	1	University of Illinois Consulting Engineering Services ATTN: N.M. Newark 1211 Civil Engineering Bldg. Urbana, IL 61801
3	IIT Research Institute ATTN: M.R. Johnson R.E. Welch Technical Library 10 West 35th Street Chicago, IL 60616	1	The University of New Mexico The Eric H. Wang Civil Engineering Research Facility ATTN: N. Baum University Station Box 25 Albuquerque, NM 87131
2	Lovelace Biomedical and Environmental Research Institute, Inc. ATTN: R.K. Jones Technical Library P.O. Box 5890 Albuquerque, NM 87115	2	Washington State University Administration Office ATTN: A.M. Hohorf G. Duval Pullman, WA 99163
			<u>Aberdeen Proving Ground</u>
1	Massachusetts Institute of Technology Aeroelastic and Structures Research Laboratory ATTN: E.A. Witmer Cambridge, MA 02139		Dir, USAMSAA ATTN: DRXSY-D DRXSY-MP, H. Cohen Cdr, USATECOM ATTN: DRSTE-TO-F Dir, USACSL, Bldg. E3516 ATTN: DRDAR-CLB-PA
2	Southwest Research Institute ATTN: W.E. Baker A.B. Wenzel P.O. Drawer 28510 San Antonio, TX 78284		
4	SRI International ATTN: G.R. Abrahamson Y. Gupta D. Keough B. Gasten 333 Ravenswood Avenue Menlo Park, CA 94025		

USER EVALUATION OF REPORT

Please take a few minutes to answer the questions below; tear out this sheet. fold as indicated, staple or tape closed, and place in the mail. Your comments will provide us with information for improving future reports.

1. BRL Report Number _____

2. Does this report satisfy a need? (Comment on purpose, related project, or other area of interest for which report will be used.)

3. How, specifically, is the report being used? (Information source, design data or procedure, management procedure, source of ideas, etc.) _____

4. Has the information in this report led to any quantitative savings as far as man-hours/contract dollars saved, operating costs avoided, efficiencies achieved, etc.? If so, please elaborate.

5. General Comments (Indicate what you think should be changed to make this report and future reports of this type more responsive to your needs, more usable, improve readability, etc.) _____

6. If you would like to be contacted by the personnel who prepared this report to raise specific questions or discuss the topic, please fill in the following information.

Name: _____

Telephone Number: _____

Organization Address: _____

----- FOLD HERE -----

Director
US Army Ballistic Research Laboratory
Aberdeen Proving Ground, MD 21005



NO POSTAGE
NECESSARY
IF MAILED
IN THE
UNITED STATES

OFFICIAL BUSINESS
PENALTY FOR PRIVATE USE, \$300

BUSINESS REPLY MAIL
FIRST CLASS PERMIT NO 12062 WASHINGTON, DC
POSTAGE WILL BE PAID BY DEPARTMENT OF THE ARMY

Director
US Army Ballistic Research Laboratory
ATTN: DRDAR-TSB
Aberdeen Proving Ground, MD 21005



----- FOLD HERE -----

